JPL Publication 15-11

Jovian Plasma Modeling for Mission Design

Henry B. Garrett
Wousik Kim
Brent Belland
Jet Propulsion Laboratory, California Institute of Technology
Pasadena, California

Robin Evans
Mori Associates, Inc.
Rockville, Maryland

National Aeronautics and
Space Administration
Jet Propulsion Laboratory
California Institute of Technology
Pasadena, California

December2015

This research was carried out at the Jet Propulsion Laboratory, California Institute of Technology, under a contract with the National Aeronautics and Space Administration.

Reference herein to any specific commercial product, process, or service by trade name, trademark, manufacturer, or otherwise, does not constitute or imply its endorsement by the United States Government or the Jet Propulsion Laboratory, California Institute of Technology.

© 2015 California Institute of Technology. Government sponsorship acknowledged.

ACKNOWLEDGMENTS

The research described in this paper was carried out at the Jet Propulsion Laboratory, California Institute of Technology, under a contract with the National Aeronautics and Space Administration. The efforts described herein have been assisted by many colleagues at the Jet Propulsion Laboratory (I. Jun, J. M. Ratliff, J. Drouilhet, and G. A. Clough) and other institutions over 30 years. The primary source and inspiration for this work, however, was our friend and mentor, Dr. T. Neil Divine, who developed the initial programs and processes on which this toolkit is based. We also thank J. E. P. Connerney and K. K. Khurana for allowing us to use their magnetic field models which are an integral part of the toolkit. We owe special thanks to the Planetary Data System (S. Joy and others) who assisted in securing much of the data we used here. In addition, we acknowledge the always helpful inputs and advice of Roger V. Carlson, the Jet Propulsion Laboratory editor.

Table of Contents

ACKNOWLEDGMENTS ..... **II**

ABSTRACT ..... **VIII**

1 INTRODUCTION **1**

2. INTRODUCTION TO DIVINE/GARRETT PLASMA MODELS **2**

2.1 DESCRIPTIONS OF THE DG1/DG2 PROGRAM ELEMENTS 4

2.1.1 Package "Distr-GIRE2KI_V3.f *4*

2.1.2 JUPRAD_GIRE2KI_V.f and GIRE2KI_subs_2-200.f *10*

2.2 SAMPLE OUTPUT FROM THE DG1/DG2 MODELS 10

3 UPDATING THE LOW ENERGY PLASMA MODELS **11**

3.1 THE VOYAGER PLS ELECTRON AND ION DATA 11

3.1.1 Additional Voyager Data—Sittler and Strobel *13*

3.1.2 Galileo Data—Frank, Paterson, Bagenal, and Delamere *15*

3.2 UPDATING THE DG1 MODEL 19

3.2.1 Updating the Model: General Comments *22*

3.2.2 Updating the Model: Inner Plasmasphere *25*

3.2.3 Updating the Model: Temperatures for R > 3.8 Rj *25*

3.2.4 Updating the Model: Number Density Variations for R > 3.8 Rj *27*

3.2.5 Updating the Model: Summary *30*

3.3 COMPARISONS OF THE DG2 PLASMA MODEL WITH DATA 30

3.4 DG2 MODEL PREDICTIONS: CONTOUR PLOTS 36

4 THE AURORAL ELECTRON FLUX **44**

5 NASCAP-2K SPACECRAFT CHARGE MODEL UPDATES **46**

5.1 OVERVIEW 46

5.2 INCORPORATION OF KAPPA DISTRIBUTIONS INTO NASCAP-2K 47

5.3 NASCAP-2K EUROPA CLIPPER CHARGING COMPUTATIONS 49

6 CONCLUSIONS **56**

7 REFERENCES **57**

APPENDIX A. CONTOUR PLOTS **60**

APPENDIX B. JOVIAN IONOSPHERE MODEL **64**

APPENDIX C. ACRONYMS AND ABBREVIATIONS **66**

Figures

Figure 1. Jovian magnetic field based on the VIP4 magnetic field model (Connerney et al., 1998). 2

Figure 2. HST UV images of the Jovian aurora. (a) Polar projections of the main auroral ovals, left is for the North Pole, right is for the South Pole (several images have been projected and superimposed). (b) Image of the northern aurora, showing the main

features: Main oval and Polar emissions as well as footprints from three of the Galilean moons (see Grodent et al., 2003, and references therein, for additional information). ... 3
Figure 3. Example of a field line/flux tube trace from a body in space down to the jovian surface. In this case, the trace is from Io down to the auroral "spots" that it creates in the jovian atmosphere (from HST UV images and the VIP4 magnetic field model. 4
Figure 4. Comparisons for Voyager 1 Plasma Science (PLS) instrument spectra at a) 1016 UT, Day 64, at 5.3 Rj and b) 1537 UT, Day 63, at 20 Rj (Divine and Garrett, 1983). 8
Figure 5. Background plasma differential fluxes at the base of the auroral zone at 15 Rj, 110° W, and 0° latitude (Garrett et al., 2008). Flux components are: a) cold (E Cold), warm (DFE2), high energy (DFE3), Kappa (DFE4) electrons, and Energetic Particle Detector (EPD); b) cold protons (H Cold), warm protons (H Hot), and singly ionized sulfur (DFS+)—latter assumed representative of the other cold ion species. 9
Figure 6. Voyager 1 electron and ion density observations versus time during the flyby of Jupiter. The data ("Voy e cts/cm^3" and "Voy ion cts/cm^3") are taken directly from the PDS.. 11
Figure 7. Voyager 2 electron and ion density observations versus time during the flyby of Jupiter. The data ("Voy e cts/cm^3" and "Voy ion cts/cm^3") are taken directly from the PDS.. 12
Figure 8. Voyager 1 electron temperature observations versus time during the flyby of Jupiter. The data are from the PDS. 12
Figure 9. Voyager 2 electron temperature observations versus time during the flyby of Jupiter. The data are from the PDS. 13
Figure 10. Voyager 1 Jupiter flyby temperatures from Sittler and Strobel (1987). Interpolated 10-minute averages of: Tc*: Estimated "cold" electron temperatures; Th*: Estimated "hot" or "warm" electron temperatures; and Tion*: Estimated cold ion temperatures. Note: according to Sittler and Strobel (1987), Tc*=Tion* near perijove. 14
Figure 11. Voyager 1 Jupiter flyby densities from Sittler and Strobel (1987). Interpolated 10--minute averages of Nh, the estimated "hot" electron density; the estimated electron density (Ne(cold) = "Voy e cts/cm^3"); and "Voy ion cts/cm^3", the estimated cold ion density. 14
Figure 12. Voyager and Galileo ion cts densities versus distance from Jupiter in Rj. The Galileo data are PLS data (Frank et al. (1992)) in the PDS and as analyzed by Bagenal and Delamere (2011). The equatorial fits, "N0", to the ion density provided by Bagenal and Delamere (2011) and by the DG2 model are also shown. 15
Figure 13. Voyager and Galileo temperature versus distance from Jupiter. The Voyager electron and ion temperature data are the same as presented in Figures 8, 9, and 10. The Galileo PLS ion data are from PDS as analyzed by Bagenal and Delamere (2011). The temperature fits are from Bagenal and Delamere (2011), the DG1, and the DG2 models. 16
Figure 14. Plot of the PLS E4 electron spin-averaged count rates averaged over Rj intervals of 1.5 Rj versus energy. 18
Figure 15. Comparison of published PLS E4 electron spectra (Frank and Paterson, 2002) at ~24 Rj and 17:15 UT and PDS E4 spin averaged data at 17:09 UT and 17:18 UT for the same time period using Eq. (3). Also plotted is the estimate of the background fluxes at 24 Rj. 19
Figure 16. Representative electron differential spectra fits at a) 10 Rj and b) 35.7 Rj (blue curves) based on the average count rates (corrected for bias effects) in Figure 14. Also shown are three different Maxwellian-based fits to the data. 20
Figure 17. Fits to the E4 PLS averages from the PDS. Values plotted are the electron total density (cm^{-3}), low energy electron density (Ne1, cm^{-3}), and high energy electron density (Ne2, cm^{-3}). 21
Figure 18. Fits to the E4 PLS averages from the PDS. Values plotted are the "average" electron temperature (eV), "RMS" electron temperature (eV), the low energy electron temperature component (Te1, eV), and high energy electron temperature component (Te2, eV). 21

Figure 19. "Mean" composition mass (M), "mean" charge (Q), and the charge ratio (M/Q) as functions of distance along the equatorial plane for the DG1/DG2 models. Also plotted are the corresponding values (B-D) from the Bagenal-Delamere model (see Delamere et al., 2005). 23
Figure 20. Scale height versus distance from Jupiter from Bagenal and Delamere (2011) Table 1 and Eq. (6). 24
Figure 21. Comparison between the original DG1 cold plasma and electron temperature variations and the new variations for the DG2 model. 26
Figure 22. Plot of the warm electron temperatures measured on Voyager 1 (Sittler and Strobel, 1987) and by the Galileo PLS as determined by this study. The latter data have been fit to the Galileo *Tew* Galileo data between ~12–30 Rj (Eq. 9). 27
Figure 23. Plots of the ion densities versus Rj for the DG1/DG2, Bagenal, and Frank fits. The Bagenal and Frank fits are defined in Bagenal and Delamer (2011). 28
Figure 24. Cold proton, warm proton, and warm electron densities. The figure is an update of Figure 6 in Divine and Garrett (1983). The observations are from Krimigis et al. (1979a,b), McNutt (1980) and Scudder et al. (1981). The model curves are for Eq. 10. 29
Figure 25. Plot of the warm electron densities measured on Voyager 1 (Sittler and Strobel, 1987) and by the Galileo PLS (as determined in this study). Also plotted are the original warm proton curves from the Divine and Garrett (1983) DG1 (their Eq. 15) and the new DG2 fit (Eq. 10) along the centrifugal equator for comparison. 29
Figure 26. Voyager 1 and 2 cold electron (Voy e) and ion (Voy ion) densities versus time (see Sittler and Strobel (1987) as adapted from the PDS) compared to the original DG1 plasma model. "RHOE" is the cold electron density and "Total Ions" the sum of all the cold ions (including the cold protons). 32
Figure 27. Voyager 1 and 2 cold electron (Voy e) and ion (Voy ion) densities versus time (see Sittler and Strobel (1987); data adapted from the PDS) compared to the new DG2 plasma model. "*RHOE*" is the cold electron density and "*Total ions*" the sum of all the cold ions (including the cold protons). 33
Figure 28. Voyager 1 and 2 electron temperatures versus time compared with DG1 and DG2 electron and ion temperature predictions during the Voyager flybys of Jupiter. The Voyager data (Voy e) are from the PDS (Sittler and Strobel, 1987). "TEMP(DG1)" are the cold ion and electron temperatures for the DG1 model. "TEMP(DG2)" and "TEMPE" are the cold ion and electron temperatures respectively for the DG2 model. 34
Figure 29. Voyager PDS cold electron and ion data (green dots) and DG2 predictions (blue dots) versus distance from Jupiter (Rj). 35
Figure 30. Galileo ion data (Bagenal and Delamere, 2011) and DG2 predictions versus distance from Jupiter (Rj). 36
Figure 31. Log_{10} of the Cold Electron Density (cm^{-3}) versus *R*(Rj) at 110° W longitude. 37
Figure 32. Log_{10} of the Cold Ion Density (cm^{-3}) versus R(Rj) at 110° W Longitude. Top contour is for the sum of the DG2 ions (excluding the protons) while the bottom contour is for an average contour suggested by the Bagenal and Delamere (2011) parameters. Note difference in scales. 38
Figure 33. Log_{10} of the Cold Ion Temperature versus R at 110° W Longitude. The top contour is the DG1 ion temperatures while the bottom contour is for the DG2 ion temperatures.. 39
Figure 34. Meridional contour plots of the three electron Kappa plasma distribution parameters (Kappa value, density, and temperature) as modeled by the DG2 plasma model. The gray contours correspond to regions where the program could not fit a Kappa distribution—typically this was where there is no high energy electron data (e.g., outside ~60 L). 40
Figure 35. Meridional contour plots of the three proton Kappa plasma distribution parameters (Kappa value, density, and temperature) as modeled by the DG2 plasma model. The gray contours correspond to regions where the program could not fit a Kappa

distribution—typically this was where there is no high energy proton data (e.g., outside ~60 L). 42
Figure 36. Plots of auroral electron fluxes incident on Jupiter's upper atmosphere as estimated by Ajello et al. (2001). A) A Maxwellian distribution function fit (Eq. (1)); B) A 3 Kappa distribution fit (Eq. (2)). 44
Figure 37. Omni-directional energy spectrum for the diffuse aurora (based on Eq. 1 in Bhattacharya et al. (2001)) at 18.4 Rj in the equatorial plane as measured by the Galileo Energetic Particle Detector(EPD) instrument. 45
Figure 38. Fits to the electron differential fluxes for the jovian aurora as defined by Ajello et al. (2001) in Figure36b. The Kappa fits are as described earlier. Also plotted is the Nascap-2k Fontheim distribution (sum of a Maxwellian, a power law spectrum and a Gaussian distributions) fit to the Ajello et al. spectrum. 46
Figure 39. The Nascap-2k Auroral Environment parameter input screen before modification. 47
Figure 40. The modified Nascap-2k Auroral Environment parameter input screen with additional Kappa parameter input boxes as added. Up to four electron Kappa distributions and two ion Kappa distributions can be modeled in addition to the pre-existing Fontheim distribution. 48
Figure 41. Comparison between the Ajello 3 Kappa distribution and the Fontheim approximation. The spacecraft potentials versus time are plotted. 49
Figure 42. Three-dimensional Nascap-2k plot of an RPS-powered Europa spacecraft design concept showing the differential surface potentials. The surface material is covered in the default conductive black Kapton with δmax = 2.1. 51
Figure 43. Sample secondary electron emission yield curve for Aluminum, δ_{max} = 1.00 showing how the secondary yield change with incident electron energy. The secondary electron yield is the number of electrons emitted from a surface for each energetic electron impacting the surface at the indicated energy. 52
Figure 44. Three-dimensional Nascap-2k plot of a Europa RPS spacecraft design showing the differential surface potentials. The surface material is covered in the default conductive black Kapton with δ_{max} = 0.87 as measured by J. R. Dennison and associates. Note the dramatic change in surface potential. 53
Figure 45. Similar plot of a Europa design for the solar spacecraft design concept showing the differential surface potentials. The spacecraft is assumed to be covered in black Kapton (with δ_{max} = 0.87) whereas the solar panels are assumed be coated with ITO (δ_{max} = 2.47). The potential is again ~+2 V. 54
Figure 46. ITO coated solar panel potential as a function of the ITO δ_{max}. 55

Tables

Table 1. Thermal populations of charged particle distributions in Jupiter's magnetosphere (Tables 6 and 7 from Divine and Garrett, 1983). 5
Table 2. Key plasma parameters returned by the DG1 and DG2 plasma models. 6
Table 3. Background plasma parameters at 70° latitude and 110° west longitude over Jupiter's North Pole and in the jovian equatorial plasmasheet for different radial distances (see Table 2 for the explanation of variables and units). 10
Table 4. PLS E4 energy channels, geometric mean energy, and channel energy width. As the particles are electrons, it is assumed that 1 E/Q in volts is equivalent to 1 eV in energy (Frank et al., 1992). 17
Table 5. Fitted Maxwellian components to Figure 14 count rates as corrected for background and converted to flux using Eq. (3). 22
Table 6. Coefficients used to define the scale height, H. Adapted (e.g., with the correction "x = $Log_{10}(r/6)$", not "x = $Log_{10}(r)$") from Bagenal and Delamere (2011) Table 1 and Eq. 6. 24

Table 7. Fits to predicted auroral oval electron fluxes for Figure 36: (a) Maxwellian distribution, (b) Kappa distributions, and, (c), for Kappa fits to the diffuse aurora over the polar caps (Figure 37) at various distances along the equatorial plane..... 45

ABSTRACT

The purpose of this report is to address uncertainties in the plasma models at Jupiter responsible for surface charging and to update the jovian plasma models using the most recent data available. The updated plasma environment models were then used to evaluate two proposed Europa mission designs for spacecraft charging effects using the Nascap-2k code. The original Divine/Garrett jovian plasma model (or "DG1", T. N. Divine and H. B. Garrett, "Charged particle distributions in Jupiter's magnetosphere," *J. Geophys. Res.,* vol. 88, pp. 6889–6903, 1983) has not been updated in 30 years, and there are known errors in the model. As an example, the cold ion plasma temperatures between ~5 and 10 Jupiter radii (Rj) were found by the experimenters who originally published the data to have been underestimated by ~2 shortly after publication of the original DG1 model. As knowledge of the plasma environment is critical to any evaluation of the surface charging at Jupiter, the original DG1 model needed to be updated to correct for this and other changes in our interpretation of the data so that charging levels could be properly estimated using the Nascap-2k charging code. As an additional task, the Nascap-2k spacecraft charging tool has been adapted to incorporate the so-called Kappa plasma distribution function—an important component of the plasma model necessary to compute the particle fluxes between ~5 keV and 100 keV (at the outset of this study, Nascap-2k did not directly incorporate this common representation of the plasma thus limiting the accuracy of our charging estimates). The updating of the DG1 model and its integration into the Nascap-2k design tool means that charging concerns can now be more efficiently evaluated and mitigated. (We note that, given the subsequent decision by the Europa project to utilize solar arrays for its baseline design, surface charging effects have become even more of an issue for its mission design). The modifications and results of those modifications to the DG1 model to produce the new DG2 model presented here and the steps taken to integrate the DG2 predictions into Nascap-2k are described in this report.

1 INTRODUCTION

Divine and Garrett developed the original DG1 jovian plasma and auroral charging models in the early 1980s (Divine and Garrett, 1983). Garrett and his colleagues at Jet Propulsion Laboratory (JPL) have since been responsible for applying these original models to the Galileo, Juno, and Europa missions (Garrett and Hoffman, 2000; Garrett et al., 2008). Since the original Pioneer and Voyager flybys that DG1 was based on, our understanding of those environments has been constantly improving. New results from Galileo, Ulysses, Cassini, and Hubble are now available. Indeed, models of specific components of the Io plasma torus, and plasma sheet by McNutt, Sittler, Bagenal, and colleagues (McNutt, 1980; McNutt et al., 1981; Sittler and Strobel, 1987; Delamere et al., 2005; Bagenal and Delamere, 2011; Smyth et al., 2011)) and visual observations from Earth of the jovian aurora (Ajello et al., 2001) are now available. Typically, however, these studies have not specifically addressed all the plasma parameters required for computing spacecraft charging at Jupiter. It is the intent of this study to incorporate the recent studies and all new data into a revised, comprehensive environment model, DG2, and determine the effects on surface potentials for representative Europa spacecraft designs.

The second part of this study is the coupling of the DG2 model to the Nascap-2k charging analysis tool (Davis et al., 2004; Mandell et al., 2006). Given the ambient plasma and auroral environments, two potential spacecraft designs for a Europa mission were then evaluated for surface charging using Nascap-2k. This tool requires a detailed definition of the ambient plasma ($E < 100$ keV) fluxes versus energy, convection velocity, and composition. The two major components of the jovian plasma environment of interest are the cold Io torus plasma and the jovian auroral particle fluxes (which dominate charging between the ~15–30 L-shells). The Nascap-2k tool principally uses combinations of Maxwell Boltzmann distributions (e.g., a plasma representation given by a "number density" and a "temperature" that follows a Gaussian distribution; see Eq. 1) to describe the plasma. The DG1 model provides not only convected Maxwellian distributions but also a more advanced representation in the form of a Kappa plasma distribution—this provides a smooth continuous spectrum from the low energy part of the spectrum up into the million electron volt range. A method for incorporating this distribution directly into the Nascap-2k code has been developed under this task that improves our ability to accurately model the response of a spacecraft to the jovian environment and will be described in Section 5.

To summarize, this report describes the following:

1) Development of an integrated plasma model update (FORTRAN code) to the original Divine/Garrett plasma model;
2) Comparison and validation of the model with the best current observations;
3) Creation of a direct linkage for a Kappa distribution function to the Nascap-2k charging code.
4) Preliminary charging analyses of a radioisotope power system (RPS) and of a solar array version of possible Europa spacecraft designs.

2. INTRODUCTION TO DIVINE/GARRETT PLASMA MODELS

As an introduction, this first section briefly describes the software that is associated with the original Divine/Garrett plasma models (Divine and Garrett, 1983; Garrett, 2006). This includes the original Divine radiation model described in Divine and Garrett (1983) (the latter is needed to estimate the Kappa distributions), the cold plasma models, and the warm electron and ion models. In 1983, Dr. Neil Divine, with the first author's assistance, developed a set of algorithms capable of estimating the jovian plasma and radiation environments for use in studying the effects of the jovian environment on JPL missions. At Dr. Divine's direction, the first author subsequently developed computer programs based on the algorithms. The plasma models were used to provide estimates of the 10–100 keV electron and 10–100 keV proton environments for Galileo, Juno, and other jovian missions. As part of those studies, the models were extended to provide estimates of the "omnidirectional" differential and integral fluence spectra using Kappa distributions. The latter provide smooth, continuous curves for the fluences over the energy ranges from tens of kiloelectron volts up to several megaelectron volts, and these particle distributions were used for estimating charging and radiation effects on solar array cover glasses.

The magnetosphere of Jupiter covered by the DG1 model is shaped by several factors. In particular, the jovian magnetic field with its tilt of 11° relative to its spin axis, its rapid rotation, and the jovian moon Io at 5.9 Jupiter radii (Rj), which generates a vast torus of neutral gas and cold plasma, are major drivers of the jovian magnetosphere. The extremely rapid rotation of Jupiter's magnetic field forces the cold plasma associated with this torus to accelerate and expand by centrifugal force into a giant disc as illustrated in Fig. 1. The magnetic field lines become distended beyond ~15 Rj and tend toward being parallel to the spin equator at greater distances. The magnetic field tilt and rotation rate cause the plasma disc to oscillate up and down so that at a given location plasma parameters vary radically during a 10-h period (5 h if the spacecraft is near the jovian equatorial plane)—the plasma also tends to follow the centrifugal equator which is tilted ~7° to the equatorial plane.

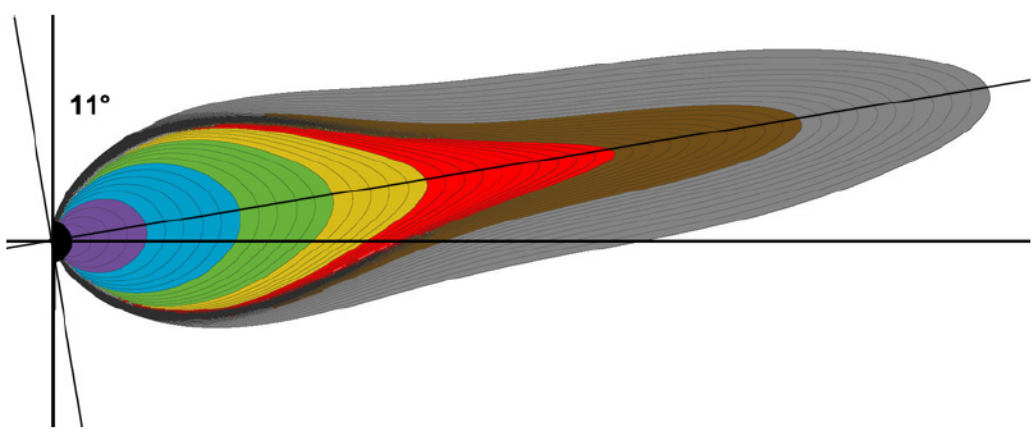

Figure 1. Jovian magnetic field based on the VIP4 magnetic field model (Connerney et al., 1998).

Jupiter's background particle environment can be roughly divided into three populations: 1) the cold plasma (1–100 eV) associated with Jupiter's ionosphere, the Io torus, and the plasma disc; 2) the intermediate plasma (0.1–100 keV); and, 3) the radiation environment covering the energy band from 0.1–100 MeV. The cold plasma is characterized by high densities (~3,000 cm^{-3}) and low energies. The plasma consists of hydrogen, oxygen (singly and doubly ionized), sulfur (singly, doubly, and triply ionized), and sodium (singly ionized) ions. Intermediate energy electrons (~5 keV) and protons (~30 keV) at Jupiter are assumed to vary exponentially from ~5 cm^{-3} inside 20 Rj to 0.001 cm^{-3} beyond 40 Rj (Divine and Garrett, 1983).

Superimposed on the background plasma is a complex auroral environment. Figure 2 (Grodent et al., 2003) is a set of UV photographs of the jovian north and south polar regions from the Hubble Space Telescope (HST)—the images clearly show several outstanding auroral features. As marked in the bottom (b) frame, the jovian auroral environment observed to-date consists of at least three components: a narrow auroral zone "ring" (labelled "Main oval" in Fig. 2) above ~60° latitude like that of the Earth's at high latitudes in the northern and southern polar regions, a broad region of somewhat diffuse aurora (labelled "Polar emission") over the polar caps, and the distinct auroral footprints associated with the **vxB** induced electric field interaction between the rapidly rotating jovian magnetosphere and its moons (labeled "Io footprint" and "Ganymede and Europa footprints" in Fig.2)—see the magnetic field line tracing for Io in Fig. 3. Each of these auroral jovian environments represents a unique current source and hence a unique charging threat to a spacecraft.

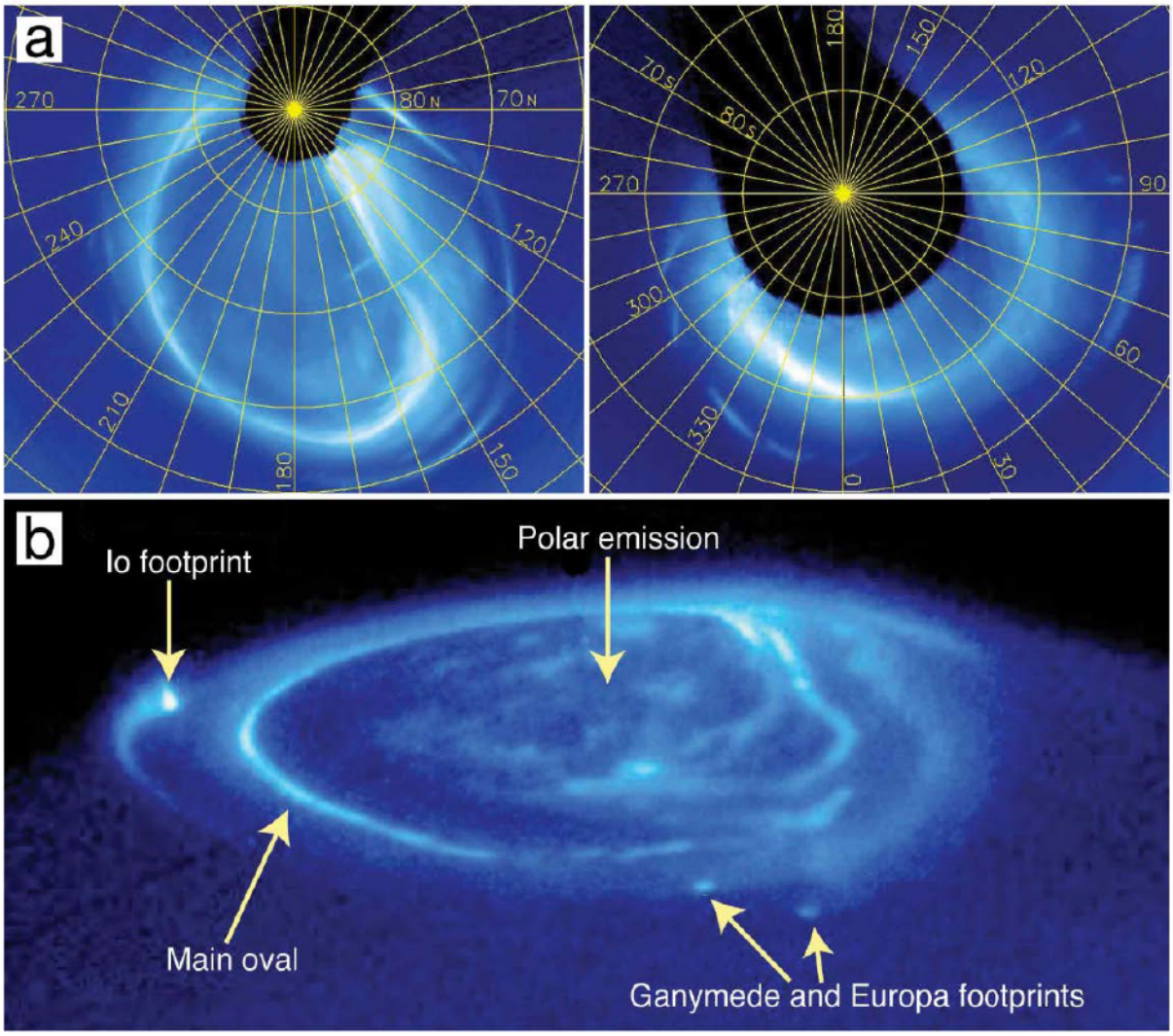

Figure 2. HST UV images of the Jovian aurora. (a) Polar projections of the main auroral ovals, left is for the North Pole, right is for the South Pole (several images have been projected and superimposed). (b) Image of the northern aurora, showing the main features: Main oval and Polar emissions as well as footprints from three of the Galilean moons (see Grodent et al., 2003, and references therein, for additional information).

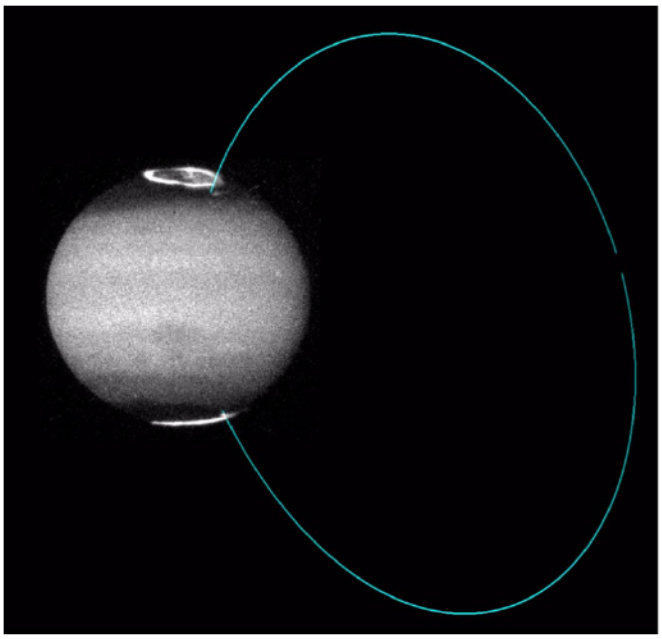

Figure 3. Example of a field line/flux tube trace from a body in space down to the jovian surface. In this case, the trace is from Io down to the auroral "spots" that it creates in the jovian atmosphere (from HST UV images and the VIP4 magnetic field model.

2.1 Descriptions of the DG1/DG2 Program Elements

This section provides an overview of the principal computer packages developed to provide estimates of the jovian environments in DG1 and DG2. Details can be found in Divine and Garrett (1983) or Garrett (2006). As the names of the base packages and their ranges have not changed, these descriptions provide a good introduction and overview of the DG2 model and the modifications to DG1. In addition to a main calling program, the principle program elements are:

Distr-GIRE2KI_V3.f

JUPRAD_GIRE2KI_V.f/GIRE2KI_subs_2-200.f

The principle I/O components are:

JDAT4a

Input.trj

Plasma.dat

Listings of the program packages and examples of input files are available upon request from the authors.

2.1.1 Package "Distr-GIRE2KI_V3.f

This package contains the fundamental algorithms for estimating the low energy plasma environments at Jupiter. The specific populations and their ranges are listed in Table 1 (copied from Divine and Garrett, 1983, Tables 6 and 7). In addition to a main driver program for the overall computer package discussed here, the "JUPRAD_GIRE2KI_V.f" and "GIRE2KI_subs_2-200.f" packages must also be included. The main inputs to the package are the trajectory data in terms of the jovian radial distance in units of "Rj" (1 Rj = 71,400 km), WLONG = west longitude-System III (Seidelmann and Divine, 1977), and ALAT=latitude, System III. Given these values, the program computes the parameters listed in Table 2. These can be output in a variety of ways or coupled with a spacecraft charging code to compute surface potentials.

Table 1. Thermal populations of charged particle distributions in Jupiter's magnetosphere (Tables 6 and 7 from Divine and Garrett, 1983).

Formulae	Parameter Values	Species
	Inner Plasmasphere: $1.0 < r < 3.8\ R_J$	
$N_k = g_k N_0 \exp\left[\frac{r_0}{r} - \left(\frac{r}{H_0} - 1\right)^2 \left(\lambda - \lambda_c\right)^2\right]$	$N_0 = 4.65\ \mathrm{cm}^{-3}$ $r_0 = 7.68\ R_J$ $H_0 = 1.0\ R_J$ $kT = 46$ eV $\omega = 12.6$ km/s R_J $\alpha = 7°$, $\tan\alpha = 0.123$ $l_0 = 21°$	$e^-\ g_0 = 1.00$ $O^+\ g_2 = 0.20$ $O^{++}\ g_2 = 0.02$ $S^+\ g_4 = 0.70$ $S^{++}\ g_5 = 0.03$ $g_1 = g_6 = g_7 = 0.00$
$\lambda_c = (\tan\alpha)\cos(l - l_0)$ $V_\phi = \omega R$		
	Cool Torus: $3.8 < r < 5.5\ R_J$	
$N_k = g_k N \exp\left[-\left(\frac{r\lambda - z_0}{H}\right)^2\right]$	N and kT from Table 7 $H_0 = 0.2\ R_J$ $E_0 = 1.0$ eV $\omega = 12.6$ km/s R_J $\alpha = 7°$, $\tan\alpha = 0.123$ $l_0 = 21°$	
$H = H_0\,(kT/E_0)^{1/2}$ $V_\phi = \omega R$ $z_0 = r(\tan\alpha)\cos(l - l_0)$		
	Warm Torus: $5.5 < r < 7.9\ R_J$	
$N_k = g_k N \exp\left[-\left(\frac{r\lambda - z_0}{H}\right)^2\right]$	N and kT from Table 7 $H_0 = 0.2\ R_J$ $E_0 = 1.0$ eV $\omega = 12.6$ km/s R_J $\alpha = 7°$, $\tan a = 0.123$ $l_0 = 21°$	$e^-\ g_0 = 1.00$ $g_1 = 0.00$ $O^+\ g_2 = 0.06$ $O^{++}\ g_3 = 0.08$ $S^+\ g_4 = 0.24$ $S^{++}\ g_5 = 0.25$ $S^{+++}\ g_6 = 0.01$ $Na^+\ g_7 = 0.01$
$H = H_0\,(kT/E_0)^{1/2}$ $V_\phi = \omega R$ $z_0 = r(\tan\alpha)\cos(l - l_0)$		
	Inner Disc: $7.9 < r < 20\ R_J$	
$N_k = g_k N \exp\left[-\left(\frac{r\lambda - z_0}{H}\right)^2\right]$ $kT = E_0 - E_1 \exp\left[-\left(\frac{r\lambda - z_0}{H}\right)^2\right]$	N from Table 7 $H = (1.82–0.041r)\ R_J$ $z_0 = \left(\frac{7r - 16}{30} R_J\right)\cos(l -$	
	$V_\phi = (8.32r + 33.6)$ km/s $E_0 = 100$ eV $E_1 = 85$ eV $l_0 = 21°$	$e^-\ g_0 = 1.00$ $g_1 = 0.00$ $O^+\ g_2 = 0.07$ $O^{++}\ g_3 = 0.06$ $S^+\ g_4 = 0.06$ $S^{++}\ g_5 = 0.26$ $S^{+++}\ g_6 = 0.06$ $Na^+\ g_7 = 0.05$
	Outer Disc: $20 < r < 170\ R_J$	
$N_k = g_k N \exp\left[-\left(\frac{r\lambda - z_0}{H}\right)^2\right]$ $kT = E_0 - E_1 \exp\left[-\left(\frac{r\lambda - z_0}{H}\right)^2\right]$ $z_0 = r_0(\tan\alpha)\cos\left[l - l_0 - \frac{w}{V_A}(r - r_0)\right]$	N from Table 7 $H = 1.0 R_J$ $E_0 = 100$ eV $E_1 = 85$ eV $\alpha = 10.77°$, $\tan\alpha = 0.19$ $V_\phi = 200$ km/s $\frac{\omega}{V_A} = 0.9\,\frac{\mathrm{deg}}{R_J}$ $r_0 = 20\ R_J$ $l_0 = 21°$ $B_0 = 53\ \gamma$ $b = 1.6$	

TABLE 7. Equatorial Parameter Values for Jupiter's Thermal Charged Particle Populations

Jovicentric Distance r, R_J	Electron density $\log N$, cm^{-3}	Temperature $\log(kT)$, eV
3.8	1.55	+1.67
4.9	2.75	−0.31
5.1	2.91	−0.18
5.3	3.27	+0.37
5.5	2.88	0.92
5.65	3.57	1.15
5.8	3.31	1.33
5.9	3.35	1.54
6.4	3.18	1.63
7.4	2.78	1.67
7.9	2.25	1.75
10.0	1.48	2.00
20.0	0.20	2.00
60.0	−2.00	2.00
100.0	−2.00	2.00
170.0	−3.00	2.00

Linear interpolation among the entries on adjacent rows is recommended.

Table 2. Key plasma parameters returned by the DG1 and DG2 plasma models.

TEMP	= Temperature of the cold ion populations (eV)
TEMPE	= Temperature of the cold electron population; added for the new DG2 version—see later; TEMPE=TEMP for DG1; (eV)
RHOT	= Base density constant used to compute constituent densities
RHOE	= Density of cold electrons (cm^{-3})
RHOH1	= Density of cold protons (cm^{-3}) (from Table 6, 0; however, see below)
RHOO1	= Density of cold O^+ (cm^{-3})
RHOO2	= Density of cold O^{++} (cm^{-3})
RHOS1	= Density of cold S^+ (cm^{-3})
RHOS2	= Density of cold S^{++} (cm^{-3})
RHOS3	= Density of cold S^{+++} (cm^{-3})
RHONA	= Density of cold Na^+ (cm^{-3})
VCNC	= Jovian plasma convection velocity (km/s)
RHOEW	= Density of warm (1–100 keV) electrons (cm^{-3})
RHOHC	= Density of cold protons to balance RHOEW and RHOHW (cm^{-3})
RHOHW	= Density of warm (1–100 keV) protons (cm^{-3})
TEW	= Temperature of warm electrons (1 keV)
THC	= Temperature of cold proton population "HC "
THW	= Temperature of warm protons (30 keV)
REK	= Kappa density of warm electrons (cm^{-3})
TEK	= Kappa temperature of warm electrons (eV)
AK	= Kappa value for warm electrons (unitless)
RHK	= Kappa density of warm protons (cm^{-3})
THK	= Kappa temperature of warm protons (eV)
AH	= Kappa value for warm protons (unitless)

These parameters provide estimates of the plasma distribution functions. The basic Boltzmann distributions assumed are of the form:

$$f_i(v) = \frac{N_i}{\pi^{3/2} v_0^3} \exp(-v^2 / v_0^2) \qquad (1)$$

where:

$v_0 = (2kT/m)^{1/2}$

v = particle velocity relative to observation point (km/s); the convection velocity V_{cnvc} can be incorporated here

N_i = number density (cm^{-3}) of species e^-, H^+, O^+, O^{++}, S^+, S^{++}, S^{+++}, Na^+ (i=0,1,2,..,7) or e^-(warm) and H^+(warm)

m = mass of species (g)

k = Boltzmann constant

T = temperature (K) of species or for the Kappa distribution:

$$f_\kappa(E) = N_\kappa (m_\kappa / 2\pi E_0)^{3/2} \kappa^{-3/2} \frac{\Gamma(\kappa+1)}{\Gamma(\kappa-1/2)} \frac{1}{(1+E/\kappa E_0)^{\kappa+1}} \tag{2}$$

where:

N_κ = Kappa number density (cm^{-3}) of species (e^- and H^+)

m_κ = Kappa distribution mass (g) of species (e^- and H^+)

κ = Kappa value

E_0 = Kappa temperature (or characteristic energy)

E = Energy of particle ($1/2\ mv^2$)

This package, coupled with output from the "JUPRAD_GIRE2KI_V.f" and "GIRE2KI_subs_2-200.f" packages, computes the cold (Boltzmann) and warm (Kappa) electron and proton distribution functions versus energy (note: for the cold protons, one can include the effects of the convection velocity, V_{cnvc}—see Eq. (1). Inputs are: position in System III [from the "traj.in" file], time step(s), spacecraft velocity (assumed 0 for this study), and energy. The program returns the distribution functions at energy E (eV):

Fe1 = distribution function for cold electrons

Fe2 = distribution function for warm electrons

Fe3 = distribution function for high energy electrons (E > 100 keV)

Fe4 = distribution function for Kappa electrons (defaults to warm electrons if no Kappa fit is possible)

FH1 = distribution function for cold protons

FH2 = distribution function for warm protons

FH3 = distribution function for high energy protons (E > 0.6 MeV)

FH4 = distribution function for Kappa protons (defaults to warm protons if no Kappa fit is possible)

Units for the distribution function are (s^3/km^6)—the tool's output has been modified to provide the data in the form of individual differential flux spectra in units of (cm^2-s-sr-keV)$^{-1}$ at each time step (see Garrett, (2006) for a detailed description and examples). Figures 4 and 5 are examples of these distribution functions.

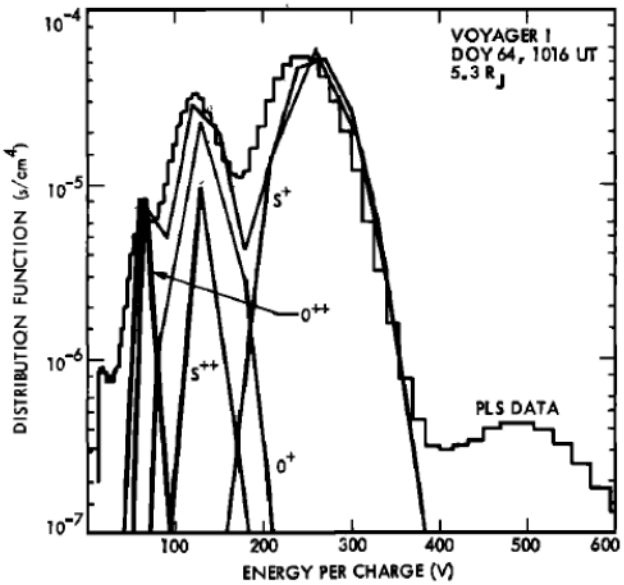

a)

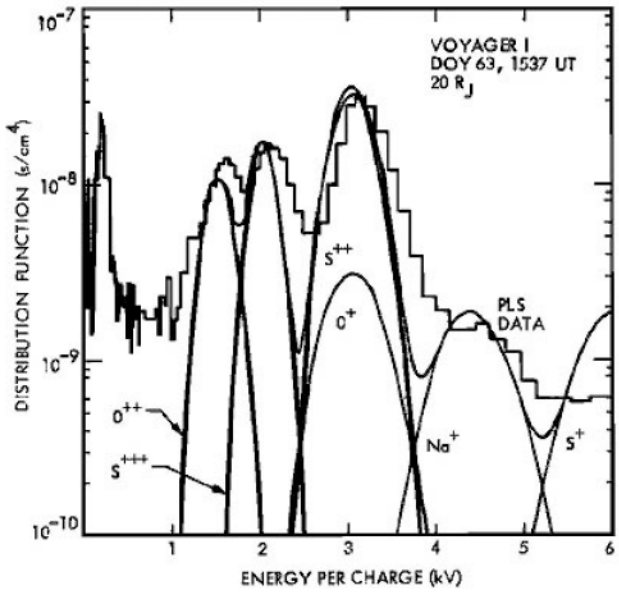

b)

Figure 4. Comparisons for Voyager 1 Plasma Science (PLS) instrument spectra at a) 1016 UT, Day 64, at 5.3 Rj and b) 1537 UT, Day 63, at 20 Rj (Divine and Garrett, 1983).

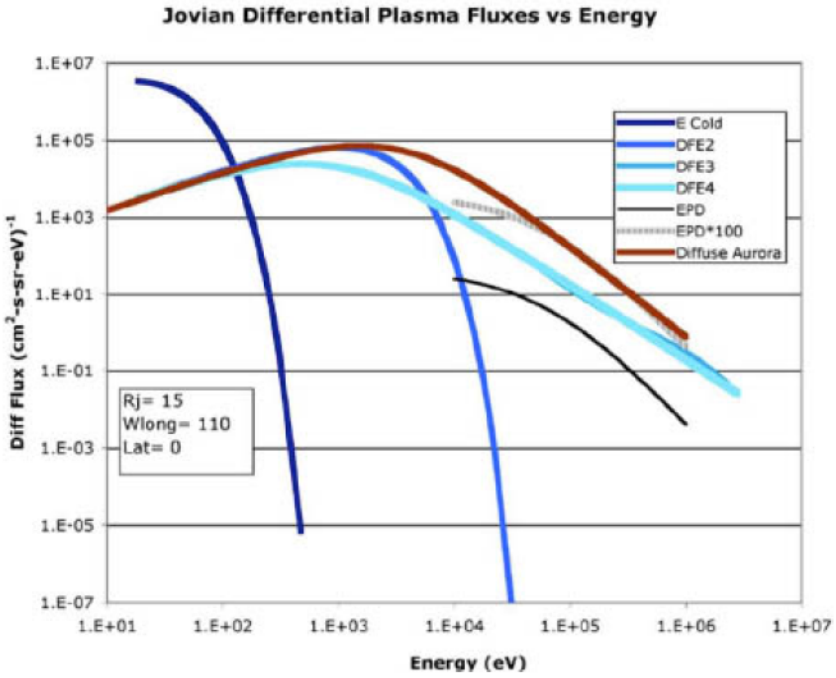

a)

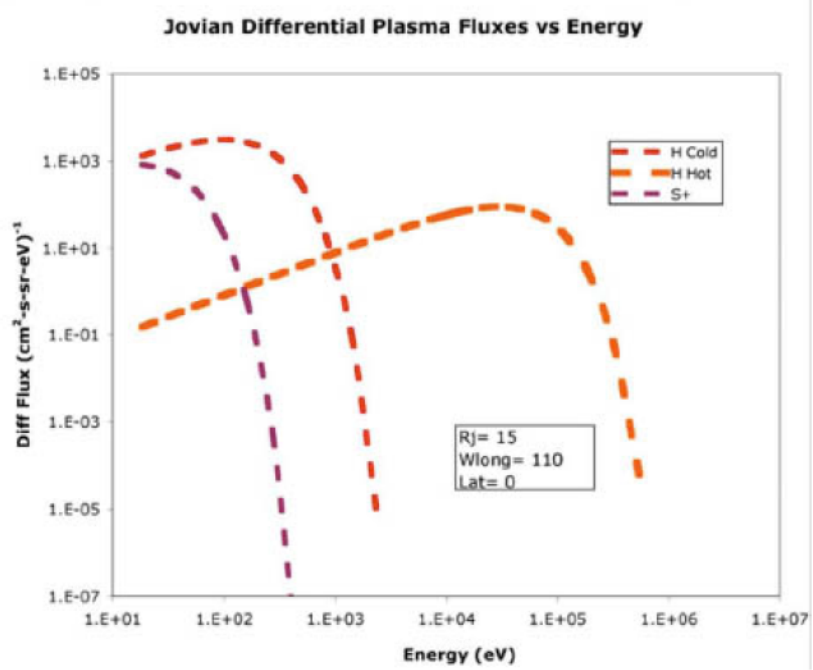

b)

Figure 5. Background plasma differential fluxes at the base of the auroral zone at 15 Rj, 110° W, and 0° latitude (Garrett et al., 2008). Flux components are: a) cold (E Cold), warm (DFE2), high energy (DFE3), Kappa (DFE4) electrons, and Energetic Particle Detector (EPD); b) cold protons (H Cold), warm protons (H Hot), and singly ionized sulfur (DFS+)—latter assumed representative of the other cold ion species.

2.1.2 JUPRAD_GIRE2KI_V.f and GIRE2KI_subs_2-200.f

To compute the high energy radiation environments necessary for the Kappa distributions, the "JUPRAD_GIRE2KI_V.f" and "GIRE2KI_subs_2-200.f" packages are required. The basic variables in the code (e.g., magnetic L shell, local field strength B, and pitch angle with respect to the field line) are determined by Jupiter's magnetic field. For reference, in the System III (Seidelmann and Divine, 1965) coordinate system, *l*, the longitude, increases westward (opposite to the azimuthal angle in a system of spherical coordinates). "JUPRAD_GIRE2KI_V.f" and "GIRE2KI_subs_2-200.f" packages are required to provide reference electron and proton fluxes at 36 keV and 316 keV for the electrons and 600 keV and 6 MeV for the protons that are used in estimating the Kappa parameters. The range of applicability of the energetic electron and proton models now extend to the jovian magnetopause—note: the proton model has been recently updated (Garrett et al., 2015). The model populations are assumed independent of time, longitude, and direction azimuth about the field line, as appropriate for stably trapped populations. The reader is referred to Divine and Garrett (1983), Garrett et al. (2012), and Garrett et al. (2015) for a complete description of the components of the jovian radiation model and its updates.

2.2 Sample Output from the DG1/DG2 Models

As an example of the output from the original DG1 model, sample values over the auroral zone and in the distant plasmasheet at the equatorial crossing point of the auroral field lines (a region where we expect surface charging to occur) are presented in Table 3—the different components were defined in Table 2. Figure 4 compares actual measurements from Voyager 1 with the DG1 model (Divine and Garrett, 1983). Corresponding differential flux plots in units of $(cm^2\text{-s-sr-eV})^{-1}$ are presented in Figure 5 at 15 Rj from Jupiter. These plots illustrate the plasma data typically needed to compute the effects of surface charging. The model predictions (from the new DG2 model) will be compared with actual data in subsequent sections.

Table 3. Background plasma parameters at 70° latitude and 110° west longitude over Jupiter's North Pole and in the jovian equatorial plasmasheet for different radial distances (see Table 2 for the explanation of variables and units).

Background

RJ	WLONG	ALAT	TEMP	RHOE	RHOHC	RHOO1	RHOO2	RHOS1	RHOS2	RHOS3	RHONA	VCNC
1.2	110	70	46	2637	3.00	527	53	1846	79	0	0	15
2	110	70	46	48.92	2.06	9.78	0.98	34	1.47	0	0	25
15	110	0	15	6.91	0.683	0.48	0.41	0.41	1.80	0.41	0.35	158

Background

RJ	WLONG	ALAT	RHOHW	THW	RHK	THK	AH
1.2	110	70	-	-	0.669	16173	3.47
2	110	70	0.021	30000	-	-	-
15	110	0	0.341	0.341	-	-	-

3 UPDATING THE LOW ENERGY PLASMA MODELS

As a first step in updating the DG1 plasma model, the original Voyager 1 and 2 plasma observations from the PLS instruments as corrected (Scudder et al., 1981; Bagenal et al., 1985; Sittler and Strobel, 1987) were reviewed and "clean" data from those papers and the Planetary Data System (PDS) prepared for testing the new DG2 model. In addition to the Voyager flyby observations, data from Galileo's 35 orbits of Jupiter are now available for analysis from the Plasma Instrumentation (PLS) (Frank et al., 1992) experiment. Bagenal and Delamere (2011, 2014) recently analyzed and fit these PLS low energy ion data from 5 Rj to 30 Rj. Electron data from the PLS as published in the PDS were analyzed by the JPL authors and used in modifying the warm electron component of the model (5 keV–50 keV). These four sets, the Voyager PLS electron and ion data and the Galileo PLS electron and ion data, form the principle data sets used to produce the DG2 model and will be separately described in Sections 3.1, 3.2, and 3.3.

3.1 The Voyager PLS Electron and Ion Data

The primary sources of Voyager plasma data are the PLS instruments (Scudder et al. 1981; Sittler and Strobel, 1987). The data are available in the Planetary Data System (PDS) for the Voyager missions for the jovian flyby segments1979-03-01 to 1979-03-05 (Voyager 1) and 1979-07-04 to 1979-07-11 (Voyager 2). The electron and ion densities ("total moment density") for both orbits are presented in Figures 6 and 7. Figures 8 and 9 are the corresponding "temperatures" for the electrons. As described in Sittler and Strobel (1987), these values have been corrected for spacecraft potential.

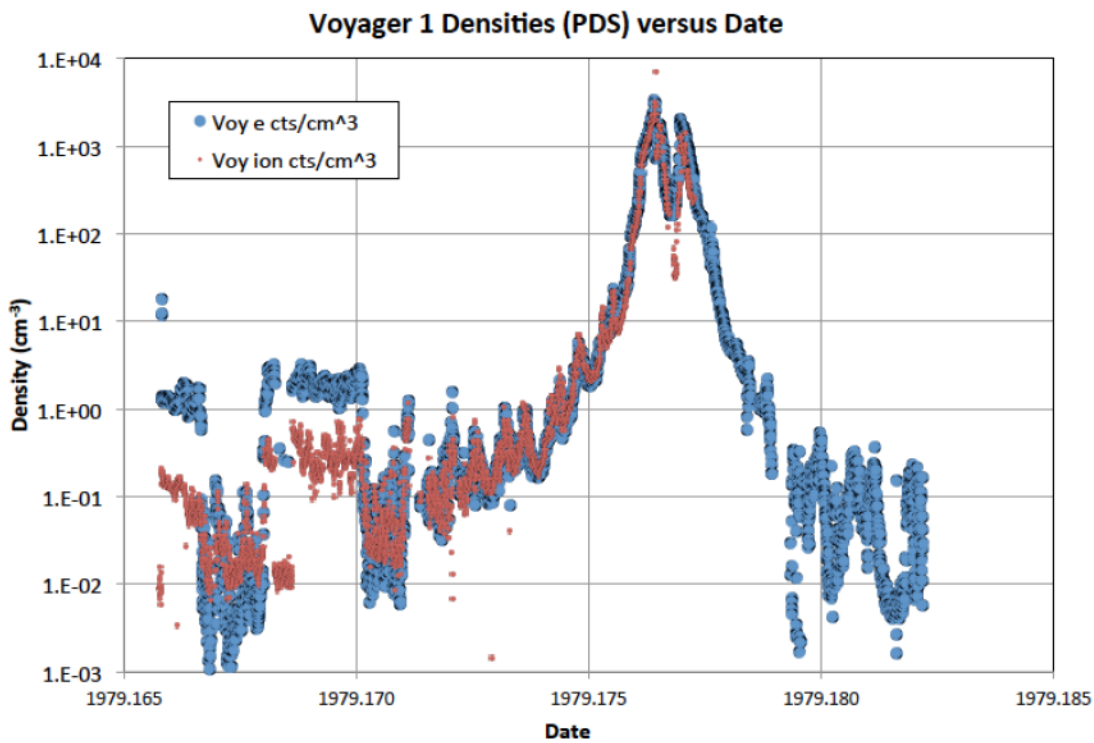

Figure 6. Voyager 1 electron and ion density observations versus time during the flyby of Jupiter. The data ("Voy e cts/cm^3" and "Voy ion cts/cm^3") are taken directly from the PDS.

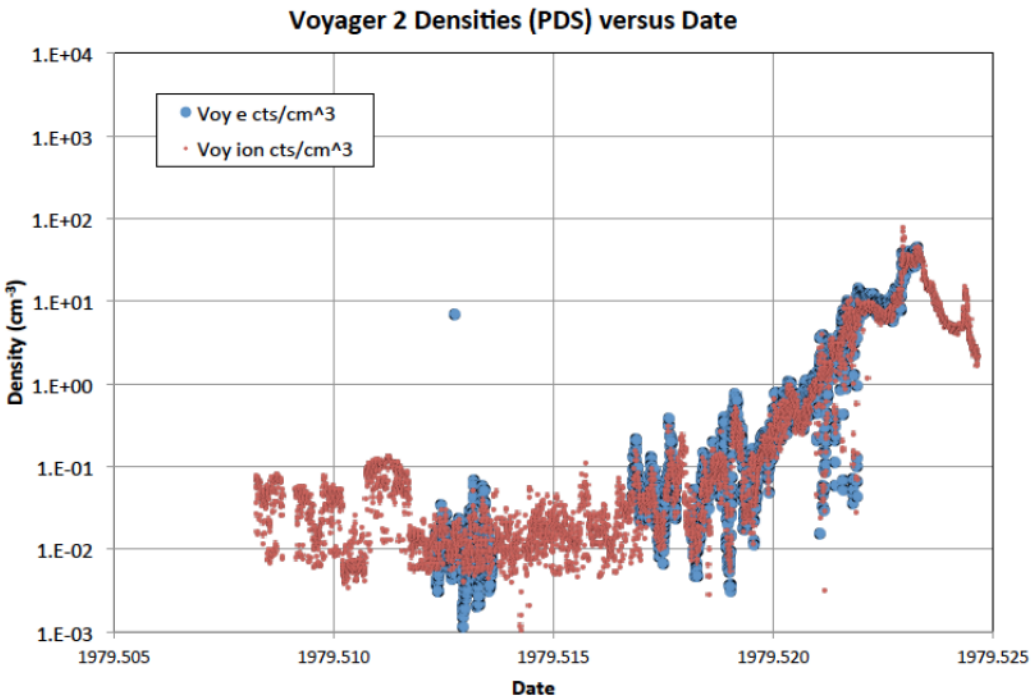

Figure 7. Voyager 2 electron and ion density observations versus time during the flyby of Jupiter. The data ("Voy e cts/cm^3" and "Voy ion cts/cm^3") are taken directly from the PDS.

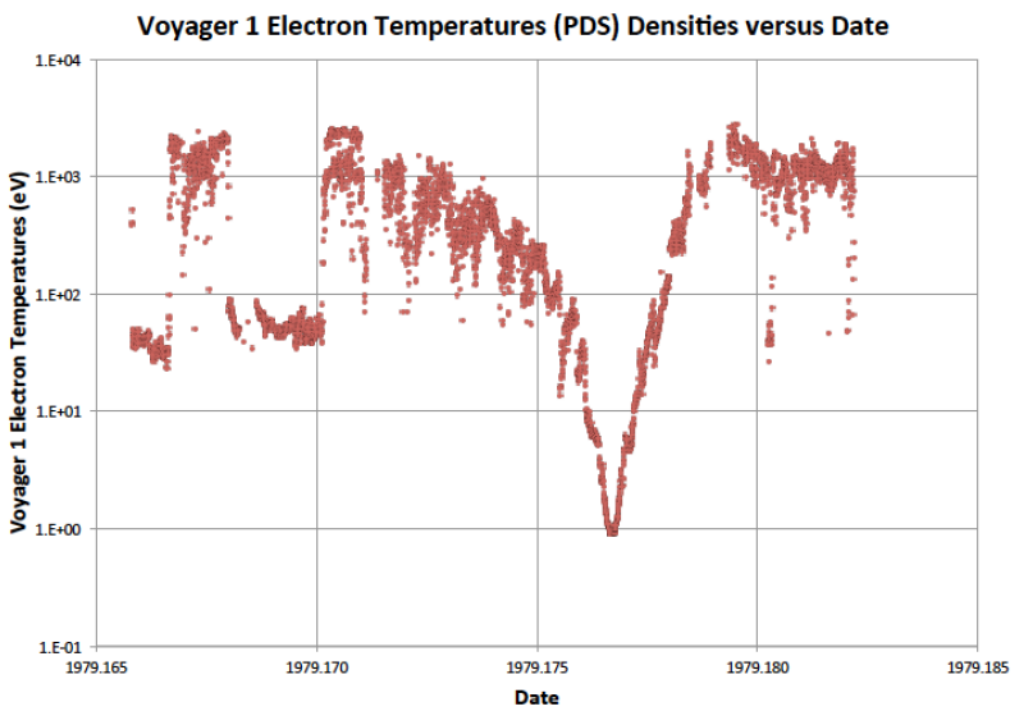

Figure 8. Voyager 1 electron temperature observations versus time during the flyby of Jupiter. The data are from the PDS.

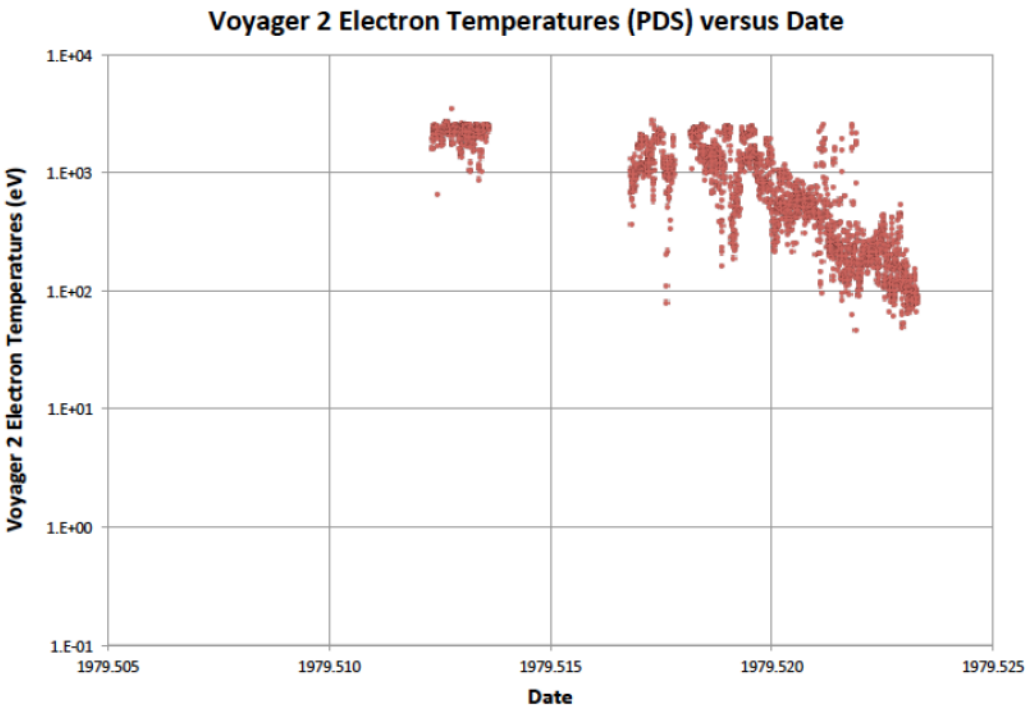

Figure 9. Voyager 2 electron temperature observations versus time during the flyby of Jupiter. The data are from the PDS.

3.1.1 Additional Voyager Data—Sittler and Strobel

In addition to the PDS electron (and ion) "total moment" density (e.g., determined by integrating over the total distribution function as opposed to the separate "cold" and "warm" components) and temperatures, Sittler and Strobel (1987) also presented estimates of what they term the "cold" and "hot" electron densities. Interpolated 10-minute averages from that paper for the temperature are plotted in Figure 10 (Tc*: Estimated "cold" electron temperatures; Th*: Estimated "hot" or "warm" electron temperatures; and Tion*: Estimated cold ion temperatures). Near perijove (11–13 UT), the cold electron and ion temperatures are assumed to be identical. The reader is referred to Sittler and Strobel (1987) for a detailed explanation of these different populations.

Figure 11 plots the PDS Voyager 1 Jupiter flyby densities (Sittler and Strobel, 1987). Shown are the interpolated 10-minute averages of the "hot" electron density scanned from Sittler and Strobel (1987). They assume that the "total moment" electron density Ne(cold) is equivalent to this density as the warm component is only a small fraction of the total and the estimated cold ion density.

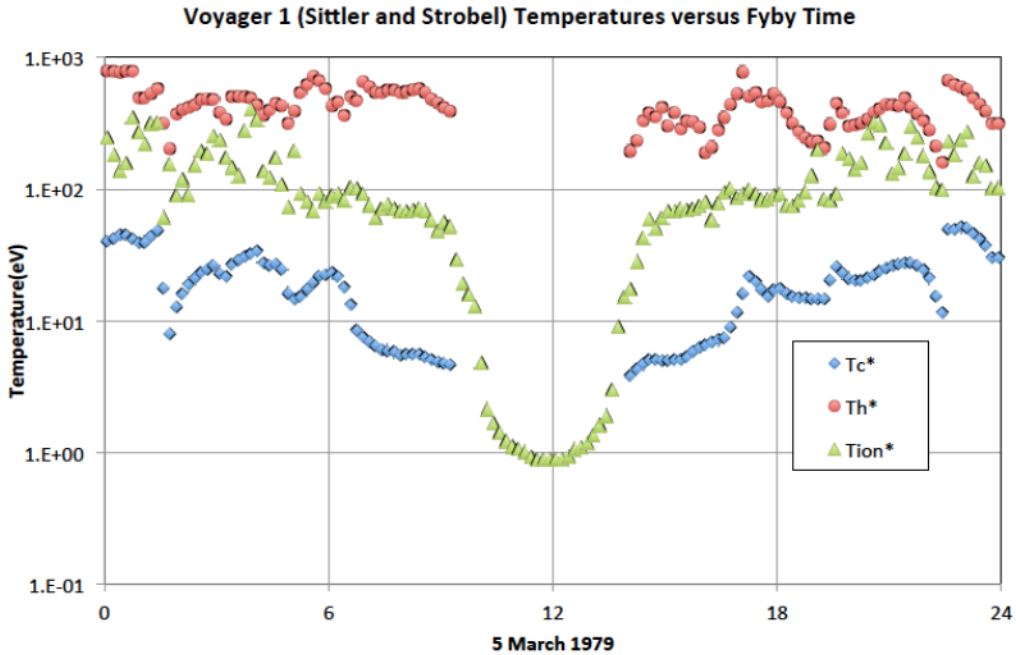

Figure 10. Voyager 1 Jupiter flyby temperatures from Sittler and Strobel (1987). Interpolated 10-minute averages of: Tc*: Estimated "cold" electron temperatures; Th*: Estimated "hot" or "warm" electron temperatures; and Tion*: Estimated cold ion temperatures. Note: according to Sittler and Strobel (1987), Tc*=Tion* near perijove.

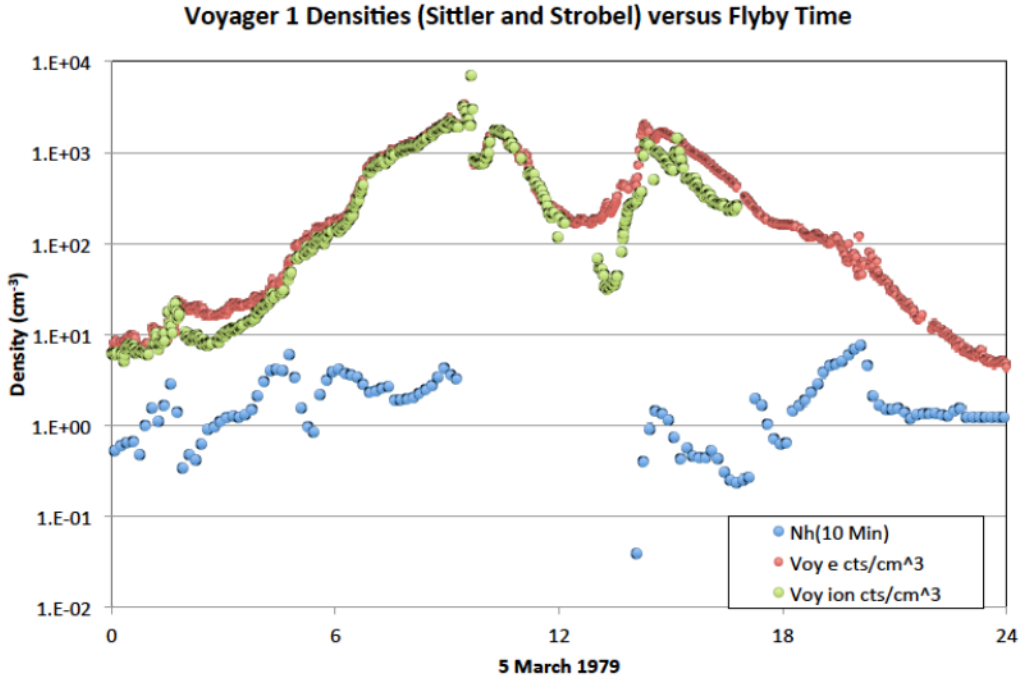

Figure 11. Voyager 1 Jupiter flyby densities from Sittler and Strobel (1987). Interpolated 10--minute averages of Nh, the estimated "hot" electron density; the estimated electron density (Ne(cold) = "Voy e cts/cm^3"); and "Voy ion cts/cm^3", the estimated cold ion density.

3.1.2 Galileo Data—Frank, Paterson, Bagenal, and Delamere

Whereas the Voyager plasma data have been reviewed and analyzed by many teams over the last few decades, the Galileo data have not been as extensively studied. Although Frank and Paterson have published analyses of several specific orbits of Galileo PLS data (e.g., Frank and Paterson, 2002), their studies do not lend themselves to a detailed statistical analysis of the overall PLS database. Fortunately they have published virtually all the data in a very extensive PLS database in the PDS. Recently, Bagenal and Delamere (2011, 2014) have begun a comprehensive review of the PLS PDS ion data. In particular, they published the "cleaned" ion data on-line at http://lasp.colorado.edu/mop/galileo/pls/index.html (Bagenal and Delamere, 2014). The orbital parameters and fits to the ion distribution function include: Orbit, UTC Time, Latitude, East Longitude, Local Time, Radius, Vr (ion bulk radial velocity), Vr error, Vtheta (ion bulk velocity in theta direction), Vtheta error, Vphi (ion bulk velocity in the phi direction), Vphi error, Ion Temperature, Temp error, Ion Total Density, and Density error. The data cover the entire Galileo mission at Jupiter for radial distances between 5 Rj and 30 Rj. Figure 12 is a plot of the total ion density that they computed compared with the Voyager ion densities versus distance from Jupiter.

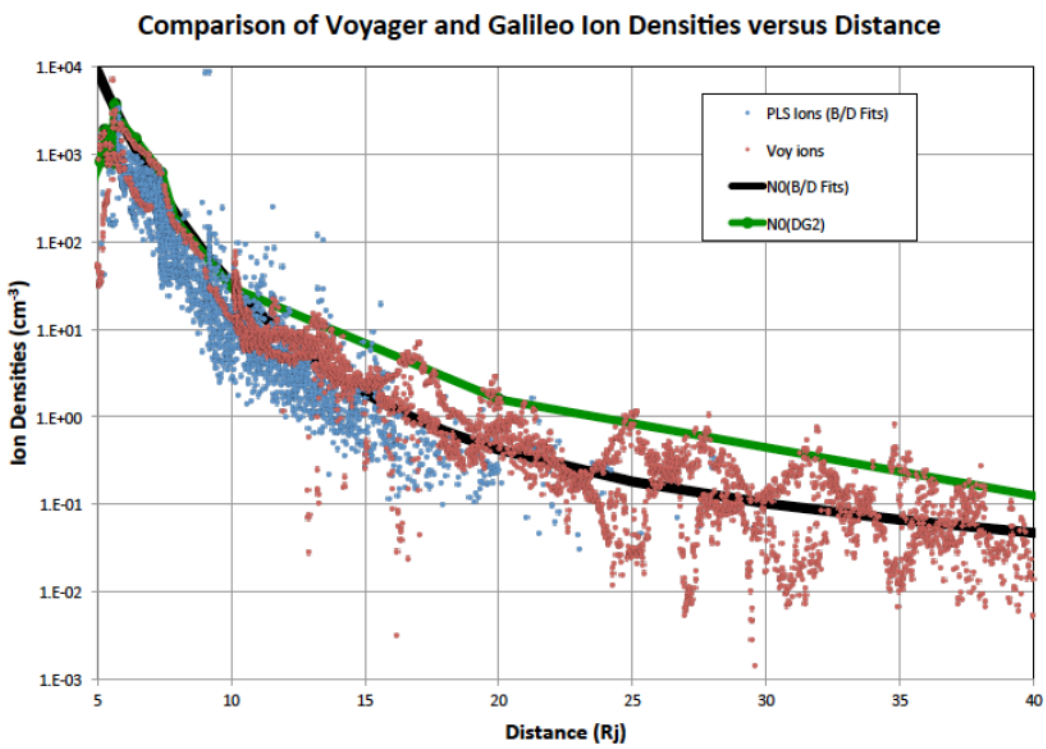

Figure 12. Voyager and Galileo ion cts densities versus distance from Jupiter in Rj. The Galileo data are PLS data (Frank et al. (1992)) in the PDS and as analyzed by Bagenal and Delamere (2011). The equatorial fits, "N0", to the ion density provided by Bagenal and Delamere (2011) and by the DG2 model are also shown.

Estimates of the Voyager and Galileo temperatures versus distance from Jupiter are plotted in Figure 13. The Voyager electron and ion temperature data are the same as presented in Figs. 8, 9, and 10. The Galileo ion data are PLS data provided by Frank and colleagues (see Frank et al. (1992) or Frank and Paterson (2002)) in the PDS and as analyzed by Bagenal and Delamere (2011). For reference, the equatorial fits to the ion temperature provided by Bagenal and Delamere (2011), the original DG1 equatorial electron/ion temperature, and the DG2 electron temperature are also included. These functions will be discussed in Section 3.2.

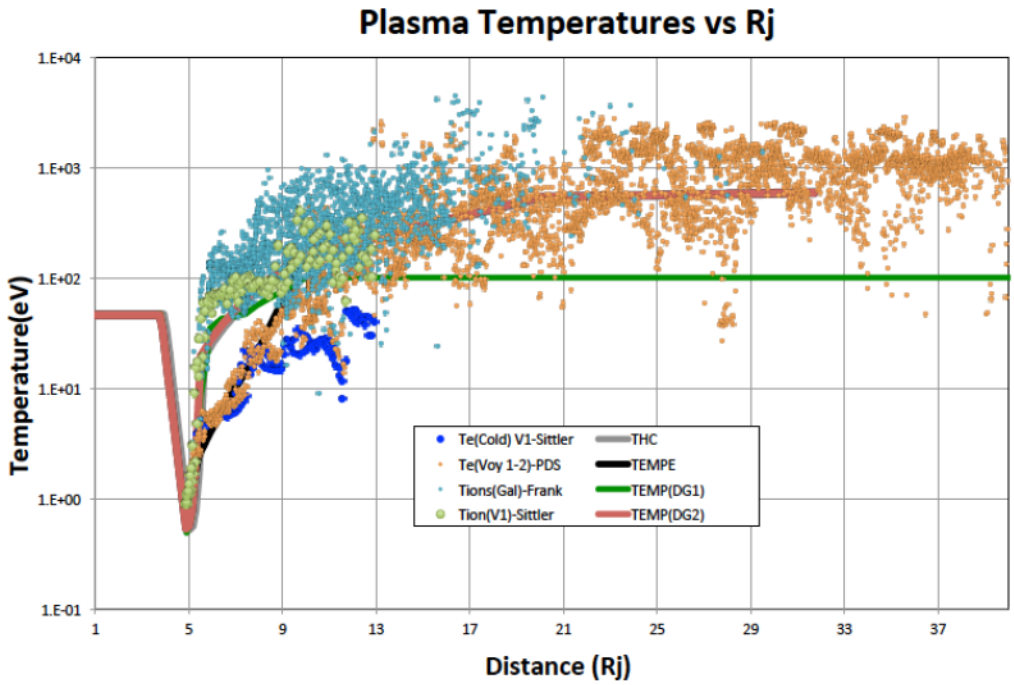

Figure 13. Voyager and Galileo temperature versus distance from Jupiter. The Voyager electron and ion temperature data are the same as presented in Figures 8, 9, and 10. The Galileo PLS ion data are from PDS as analyzed by Bagenal and Delamere (2011). The temperature fits are from Bagenal and Delamere (2011), the DG1, and the DG2 models.

As far as the authors are aware, no similar comprehensive analysis like that of the Galileo PLS ions or the PLS electron data has been carried out. Indeed, the volume of data available in terms of energy and pitch angle is nearly overwhelming. Furthermore, our analysis indicates that below ~500 eV and inside ~10–12 Rj the electron data have a large background count rate (see Fig. 14 and remarks associated with it). Rather than attempt a detailed analysis of the electron spectra channel by channel and as a function of pitch angle—a level of effort beyond the limited scope of the current task—it was decided to use the PDS "Galileo Jupiter Plasma Resampled Browse Spectra" (GO-J-PLS-4-SUMM-BROWSE-V1.0, PLS SUMMARY E4). This database contains spin-averaged electron count rates from the PLS E4 detector acquired at Jupiter between 1995 and 2003. The E4 detector was perpendicular to the spacecraft spin axis and covered an 81°–102° polar angle. Electron count rates for 14 energy bands for the energy per unit charge (E/Q) range of 3.9–48,790 V are available (see Table 4). The data covered the radial distances from ~3 Rj to ~140 Rj (because of high background rates, we will only be using the data between ~12 and 40 Rj).

We note that the PLS experimenters (Frank et al., 1992) specifically state that these spin-averaged data are not intended for detailed analysis but rather to identify regions of interest—they encourage the use of the more detailed PLS data. Their primary concern is that effects due to spacecraft charging and background from high energy, penetrating radiation have not been removed. In our analysis that follows, we will specifically correct for the noise background by limiting the range of our study to those channels that we believe are not affected. As these channels have energies above several hundred volts, which is above the tens of volts expected from spacecraft charging for the majority of the data, we have further assumed charging will not impact our fits as the expected levels (again roughly tens of volts) are well below the energy range studied.

Table 4. PLS E4 energy channels, geometric mean energy, and channel energy width. As the particles are electrons, it is assumed that 1 E/Q in volts is equivalent to 1 eV in energy (Frank et al., 1992).

Energy Channel	Energy(eV)	Delta E(eV)
3.9–6.7	5.1	2.8
8.0–13.5	10.39	5.5
16.1–26.9	20.81	10.8
31.9–53.1	41.16	21.2
62.6–104.	80.69	41.4
123.1–204.3	158.59	81.2
227.–422.1	309.54	195.1
510.0–892.5	674.67	382.5
1071–1819	1395.76	748
2159–3519	2756.36	1360
4250–7225	5541.32	2975
8194–14110	10752.55	5916
16694–27710	21507.92	11016
32300–48790	39697.82	16490

The first step in analyzing the spin-averaged E4 electron data was to average the data in L and Rj bins by energy channel. Figure 14 shows the results of that averaging process, namely the average count rate per energy channel at the indicated distance (the average for a distance interval from 8 Rj to 37.5 Rj in steps of 1.5 Rj). The effects of the noise background, presumably due to penetrating energetic electrons (E > 10 MeV), are clearly visible. To correct for this, the average count rate in the lowest energy channel (3.9–6.7 V) as a function of distance was subtracted from each average count rate. The channel energy steps and "mean" energies (actually the geometric mean of the channel energies) are listed in Table 4. The results were then converted to flux using the relationship:

$$dJ_i(E_i,Rj)/dE = CTS(E_i,Rj)/(dE_i * GF_i) \qquad (3)$$

where:

dJ_i/dE_I	=	Electron number flux (particles/cm^2-s-sr-eV)) for a given E_i and Rj
$CTS(E_i,Rj)$	=	Average counts per second for a given E_i and Rj
E_i	=	Average energy (eV) for channel "i"; geometric mean assumed
dE_I	=	Channel width for energy E_i (eV)
GF_i	=	Geometric Factor; for PLS E4 detector = 5e-5 cm^2-s-sr; (Frank et al., 1992).

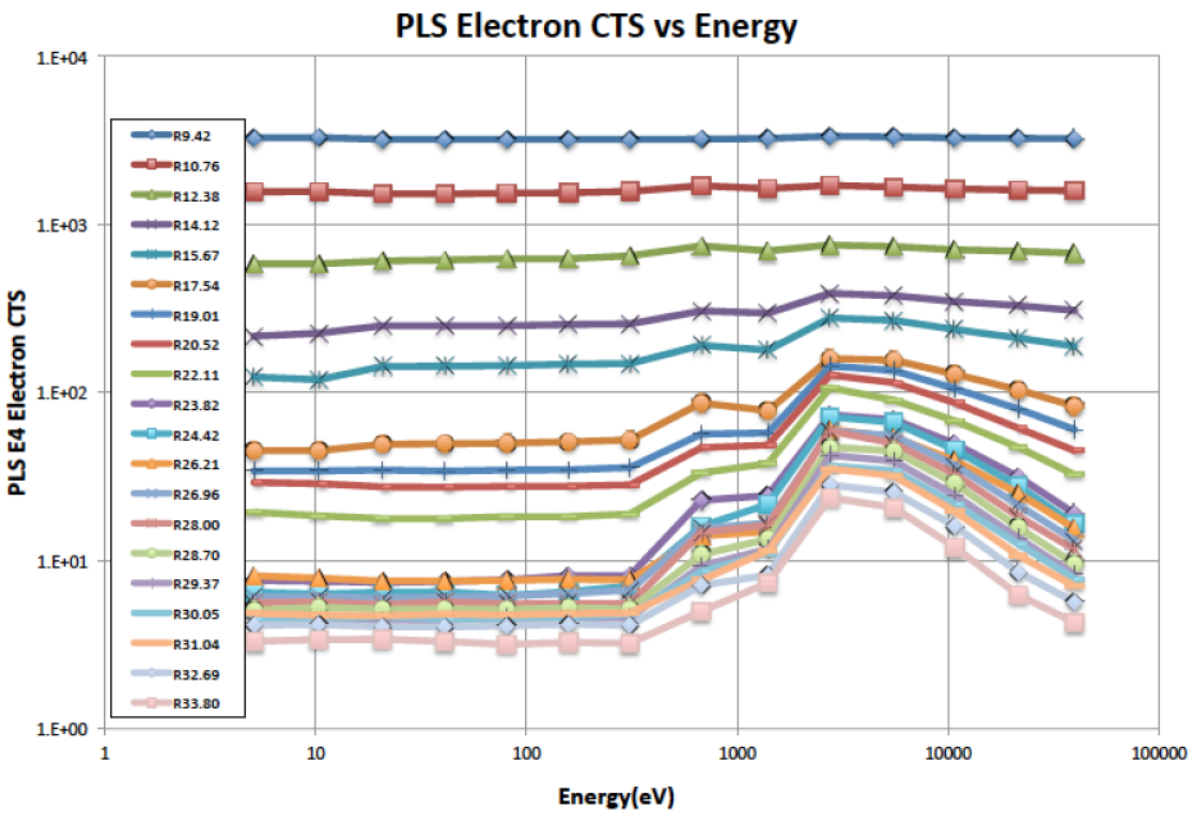

Figure 14. Plot of the PLS E4 electron spin-averaged count rates averaged over Rj intervals of 1.5 Rj versus energy.

Figure 15 is a comparison of two published PLS E4 electron spectra (Frank and Paterson, 2002) at ~24 Rj (17:15 UT) and two PDS E4 spin averaged data (labeled PLS E4 17:09 and 17:18) bracketing the observations to demonstrate that the conversion from CTS to flux is valid. Also plotted is our estimate of the background fluxes at 24 Rj. The two E4 reference spectra, which were chosen by Frank and Paterson to illustrate pitch angle variations, compare well with the two E4 average spectra from the PDS. The energies from the reference spectra appear to be uniformly displaced to slightly higher energies than the mean energies calculated in Table 4—our E4 energies compare closely, however, with later published plots.

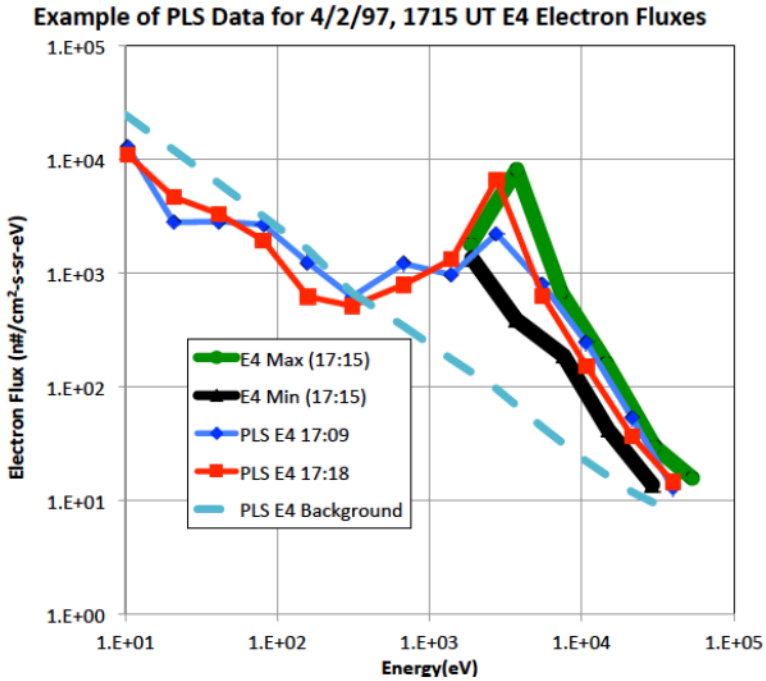

Figure 15. Comparison of published PLS E4 electron spectra (Frank and Paterson, 2002) at ~24 Rj and 17:15 UT and PDS E4 spin averaged data at 17:09 UT and 17:18 UT for the same time period using Eq. (3). Also plotted is the estimate of the background fluxes at 24 Rj.

The average count rates versus distance (Figure 14), corrected by subtracting the background at 5.5 eV, have been converted to differential particle fluxes. Two examples, at 10 Rj and 35.7 Rj, are provided in Figure 16. The Maxwellian fit values to the data in Figure 14 are tabulated in Table 5. Listed as a function of distance are the total electron density (cm^{-3}), "average" electron temperature (eV), "RMS" electron temperature (eV), low energy electron density (Ne1, cm^{-3}), low energy electron temperature (Te1, eV), high energy electron density (Ne2, cm^{-3}), and high energy electron temperature (Te2, eV). These parameters and their derivations are defined in Garrett and Deforest (1979). The electron densities are plotted in Figure 17 and the temperatures in Figure 18.

3.2 Updating the DG1 Model

The original DG1 model was carefully fit to Pioneer and Voyager data as described in Divine and Garrett (1983). Each fit component was tested against the data and adjusted to minimize any associated errors. As discussed earlier, the fits to the plasma data are defined in Table 1. The original model has also been adjusted to take into account the corrections to the Voyager data and the new findings from the Galileo PLS. In addition, the radiation model was updated to the latest versions of the GIRE electron and proton models, the warm electron and proton environments were modified to fit the new Galileo data, and a simple ionosphere model added to anticipate the upcoming Juno mission results in that region. The steps taken to implement these updates are described in the following. The results are then compared with actual data to demonstrate the validity of the updated model. Finally, the model is used to provide predictions of the various jovian plasma components to demonstrate the utility of the model for predicting the environments to be encountered a possible Europa mission.

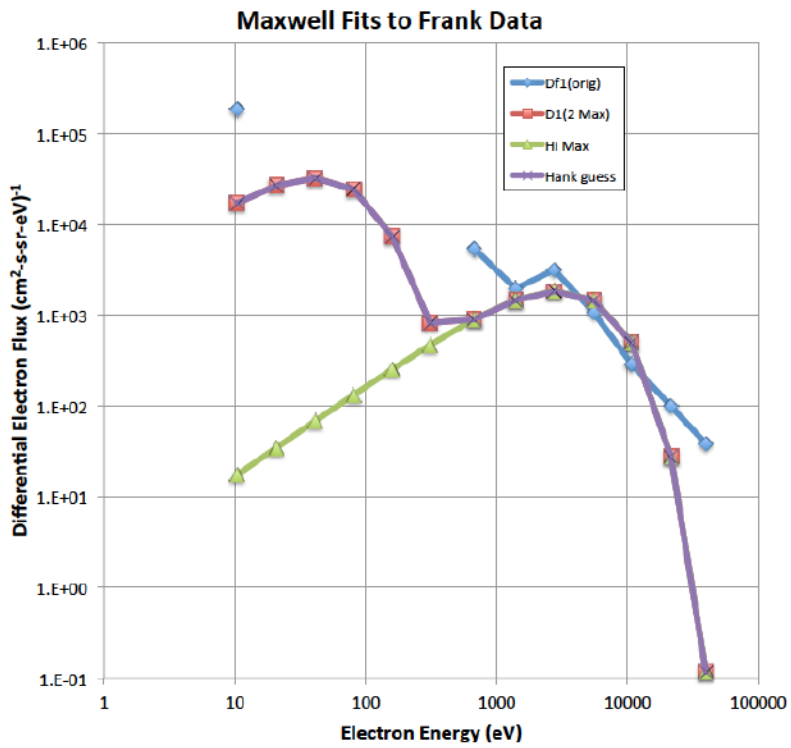

a)

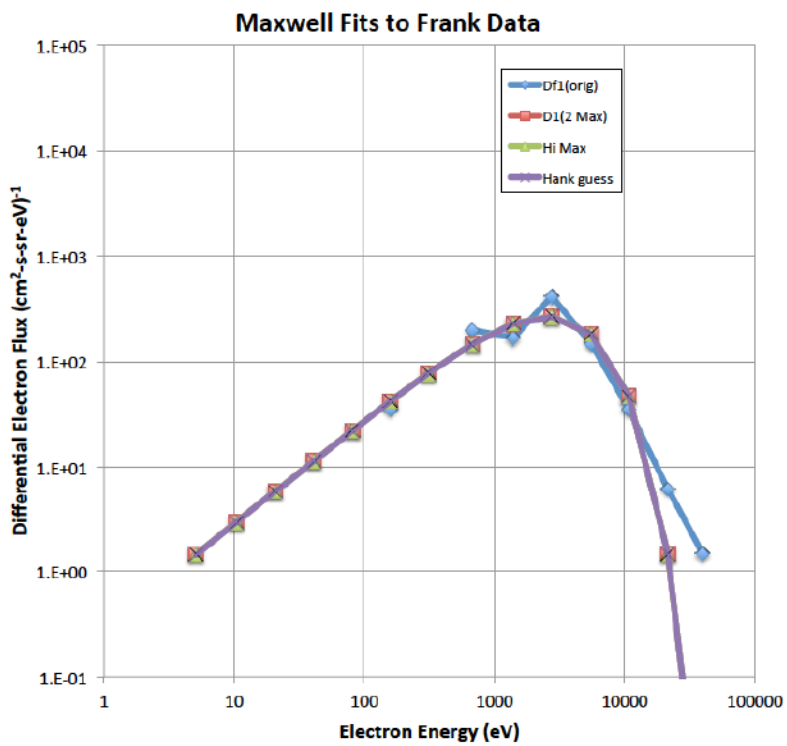

b)

Figure 16. Representative electron differential spectra fits at a) 10 Rj and b) 35.7 Rj (blue curves) based on the average count rates (corrected for bias effects) in Figure 14. Also shown are three different Maxwellian-based fits to the data.

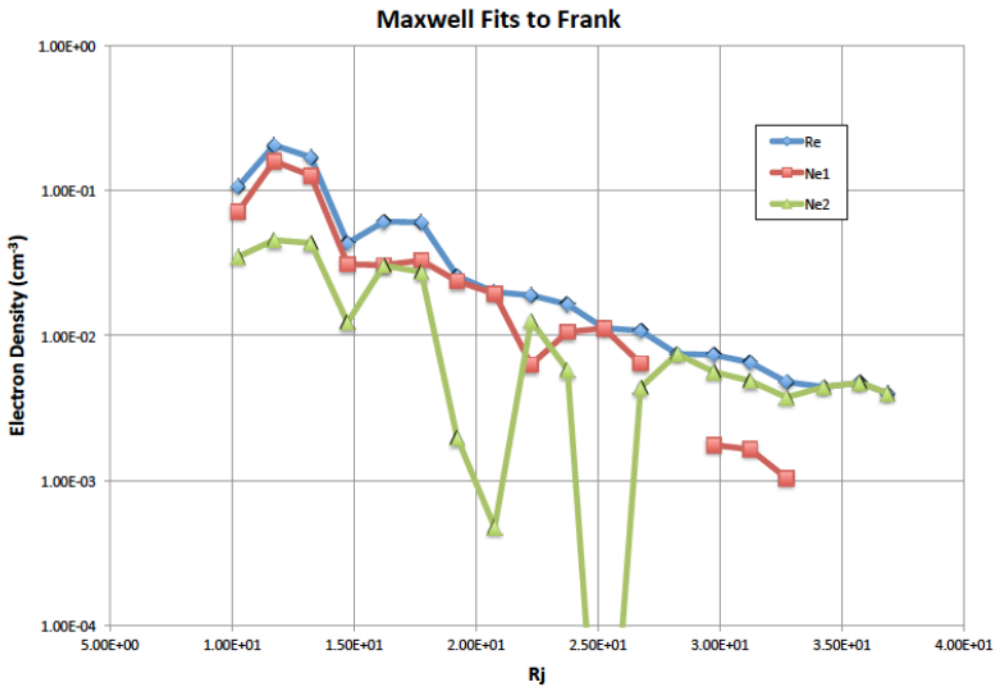

Figure 17. Fits to the E4 PLS averages from the PDS. Values plotted are the electron total density (cm^{-3}), low energy electron density (Ne1, cm^{-3}), and high energy electron density (Ne2, cm^{-3}).

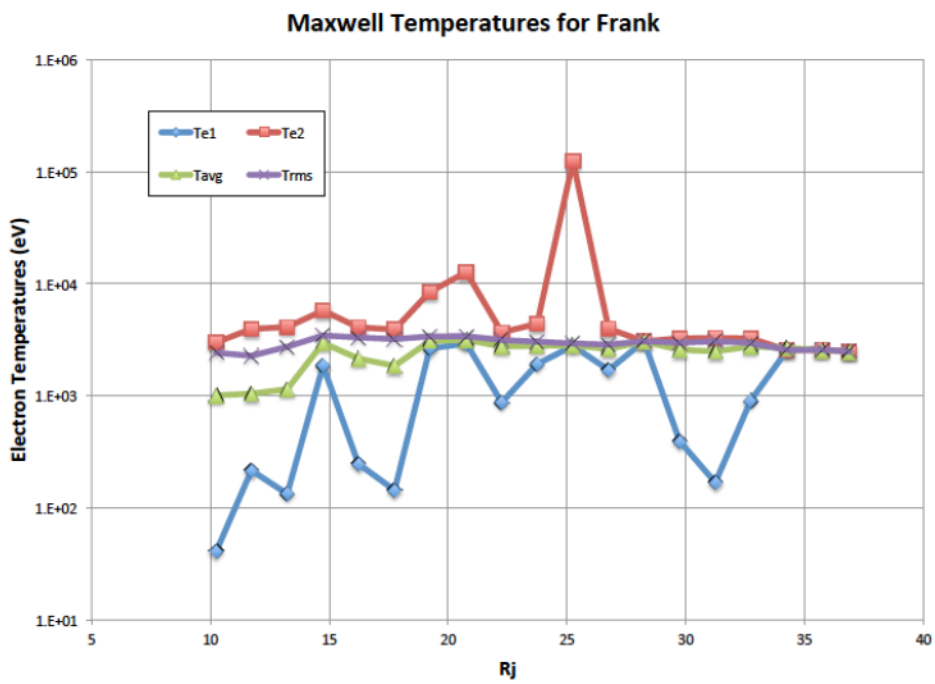

Figure 18. Fits to the E4 PLS averages from the PDS. Values plotted are the "average" electron temperature (eV), "RMS" electron temperature (eV), the low energy electron temperature component (Te1, eV), and high energy electron temperature component (Te2, eV).

Table 5. Fitted Maxwellian components to Figure 14 count rates as corrected for background and converted to flux using Eq. (3).

Rj	Rtot	Tavg	Trms	Ne1	Te1	Ne2	Te2
10.25	1.07E-01	1009	2425	7.18E-02	41	3.50E-02	2998
11.72	2.06E-01	1046	2275	1.60E-01	216	4.57E-02	3961
13.23	1.71E-01	1147	2736	1.27E-01	134	4.36E-02	4107
14.74	4.35E-02	2963	3463	3.11E-02	1857	1.24E-02	5761
16.23	6.11E-02	2150	3312	3.06E-02	246	3.04E-02	4072
17.75	6.06E-02	1855	3210	3.31E-02	144	2.75E-02	3918
19.23	2.57E-02	3083	3390	2.38E-02	2643	1.97E-03	8454
20.77	1.99E-02	3158	3401	1.95E-02	2929	4.75E-04	12721
22.26	1.90E-02	2753	3143	6.30E-03	871	1.27E-02	3692
23.75	1.64E-02	2789	3039	1.06E-02	1916	5.79E-03	4397
25.25	1.12E-02	2809	2936	1.12E-02	2791	-	-
26.75	1.08E-02	2621	2862	6.43E-03	1702	4.39E-03	3977
28.24	7.48E-03	3050	3065	0.00E+00	3065	7.48E-03	3065
29.75	7.37E-03	2574	2977	1.75E-03	394	5.62E-03	3258
31.24	6.51E-03	2495	3061	1.64E-03	168	4.87E-03	3282
32.73	4.79E-03	2747	2960	1.04E-03	903	3.75E-03	3261
34.27	4.43E-03	2676	2562	0.00E+00	2562	4.43E-03	2562
35.74	4.74E-03	2546	2579	0.00E+00	2579	4.74E-03	2579
36.88	3.99E-03	2477	2478	0.00E+00	2478	3.99E-03	2478

3.2.1 Updating the Model: General Comments

In DG1and DG2, the plasma environment is represented in terms of a cold electrons species (subscript i = 0), a cold proton environment (i = 1), warm electrons and protons, and six positive ion species (i = 2,…,7 as defined in Table 1 and Eq. (1)). Each cold species is defined by an isotropic Maxwellian distribution (Eq. (1) and Table 3) and the convection velocity *Vcnc*. The ions and electrons were all assumed in DG1 to have a common temperature relative to the convection velocity (note: the electron temperatures have been corrected between 5.3 and 7.9 Rj in DG2). In both models, for a given ion mass $a = A_i m_p$, charge $z_i^* e$, and number density $N_i = g_i N_0$. N_0 is the cold electron concentration, and charge neutrality is strictly maintained for the cold components (excluding the cold protons) by requiring:

$$\sum_{i=2}^{7} g_i \, z_i^* = g_0 = 1 \qquad (4)$$

where g_i is the fraction of the normalized charge density (assumed to equal the electron charge density "1"; i.e., the total ion charge density equals the total electron charge density). The cold protons ($i = 1$) and warm protons were approximately balanced by the warm electrons in the old DG1 model and in the new DG2 model—see Section 3.2.4. The proton mass m_p is 1.673e-27 kg, the electron atomic mass A_0 is 5.45e-4 AMU, and the charge e is 1.602e-19 C. The specific composition assumptions (see Table 1) and the data source/assumptions are described in Divine and Garrett (1983). The "mean" composition mass (M), "mean" charge (Q), and the charge ratio (M/Q) as functions of distance along the equatorial plane are plotted in Figure 19 along with the corresponding values from the Bagenal-Delamere model (see Delamere et al., 2005).

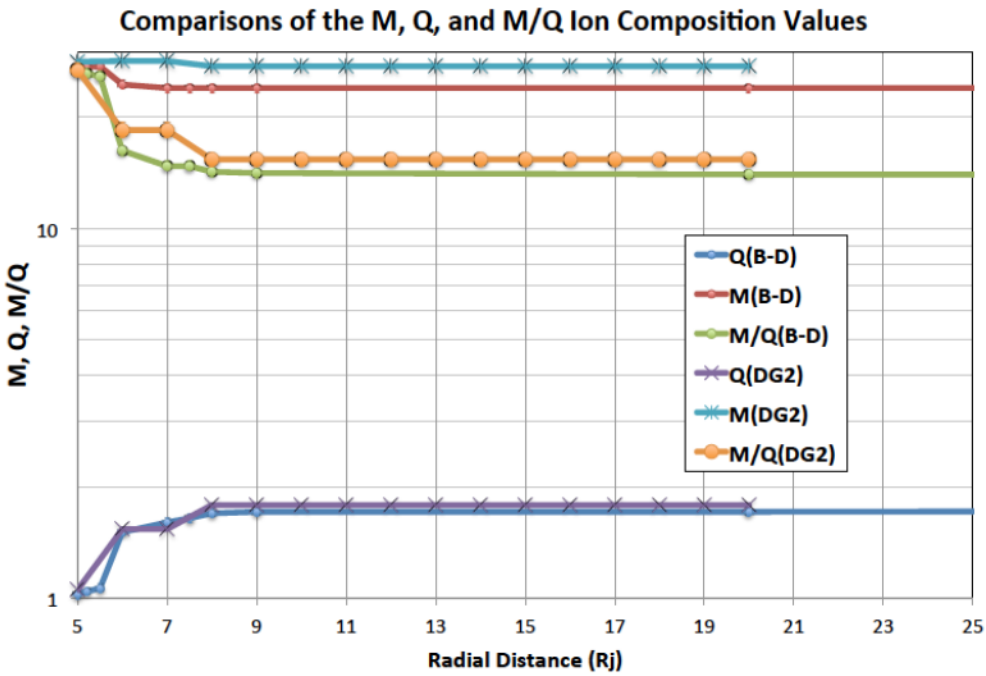

Figure 19. "Mean" composition mass (M), "mean" charge (Q), and the charge ratio (M/Q) as functions of distance along the equatorial plane for the DG1/DG2 models. Also plotted are the corresponding values (B-D) from the Bagenal-Delamere model (see Delamere et al., 2005).

The plasma torus and extended jovian plasma sheet outside ~3.8 Rj are believed to fall off approximately exponentially with a scale height H with distance z from the centrifugal equator. That is (Hill and Michel, 1976):

$$n(z,r) = n_0(r)e^{-\left(\frac{z}{H(r)}\right)^2} \tag{5}$$

where:

$n(z,r)$	=	Number density (electron or ion) as a function of z and r
$n_0(r)$	=	Number density (electron or ion) along equator as a function of r
z	=	Distance above the centrifugal equator (see Table 2) (i.e., the distance along the spin axis in cylindrical coordinates)
r	=	Distance from Jupiter in the equatorial plane (i.e., the radial distance in cylindrical coordinate); $r = R\cos(\lambda)$
R	=	Distance (in spherical coordinates) to location in units of Rj
λ	=	Jovian latitude
H	=	Scale height along the centrifugal equator as a function of r. H is plotted in Figure 20.

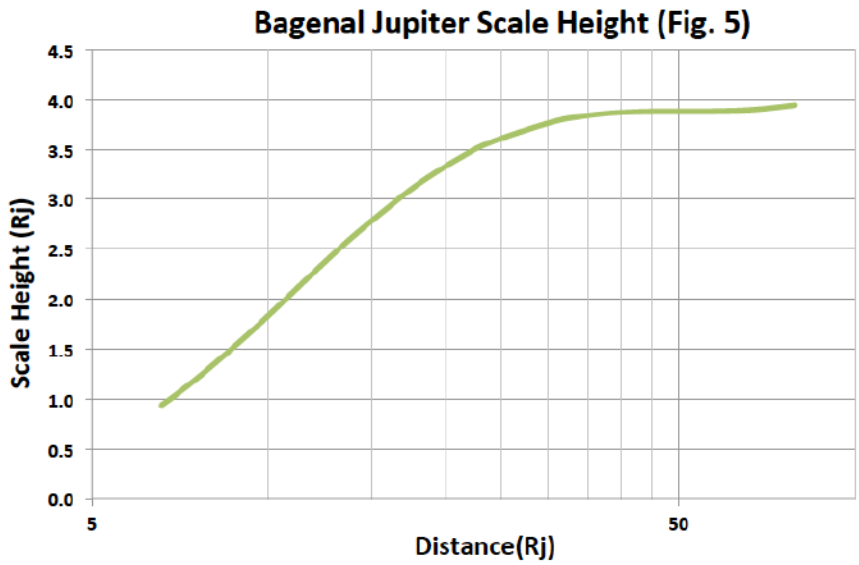

Figure 20. Scale height versus distance from Jupiter from Bagenal and Delamere (2011) Table 1 and Eq. (6).

H, the scale height, is defined in Table 1 for the DG1 model. At all distances in the DG1 and DG2 models, H is measured relative to the plasma equator. The latter is assumed be inclined by an angle corresponding to the centrifugal equator not the dipole equator (this varies from 7° to 10.77°—Table 1). A major change for the DG2 model, however, was to redefine the scale height for distances >5.5 Rj to agree with Bagenal and Delamere (2011). In particular, H will be defined for R > 5.5 Rj by the Bagenal-Delamere Eq. (6):

$$Log_{10}(H(x)) = a_1 + a_2 x + a_3 x^2 + a_4 x^3 + a_5 x^4 \qquad (6)$$

where:

x = $\text{Log}_{10}(r/6)$; again, r is in cylindrical coordinates

a_i = Coefficients defined in Table 6

Table 6. Coefficients used to define the scale height, H. Adapted (e.g., with the correction "x = Log_{10}(r/6)", not "x = Log_{10}(r)") from Bagenal and Delamere (2011) Table 1 and Eq. 6.

a_1	–0.116
a_2	2.140
a_3	–2.050
a_4	0.491
a_5	0.126

The second major change between DG1 and DG2 was to link the cold ion and electron temperatures for R $\geq$ 5.5 Rj to H by the following equation (Eq. (3); Bagenal and Delamere, 2011):

$$T(H) = A_i (H/0.64)^2 \qquad (7)$$

where:

T(*H*)	=	Cold ion and electron temperature in eV as a function of scale height H
A_i	=	~20 atomic mass units (AMU) corresponding to a mixture of sulfur and oxygen (Bagenal and Delamere, 2011)

Bagenal and Delamere (2011) state that the uncertainties in the composition, A_i, are a factor of ~2. Although this is consistent with the DG1 model, which suggests a value half their estimate (Table 1), we have assumed their new value. The improvements in our final data fits to the Voyager data will prove to bear out the assumption of ~20 AMU (compare Figure 26 to Figure 27 for example).

3.2.2 Updating the Model: Inner Plasmasphere

The inner plasmasphere (1.0 Rj < R < 3.8 Rj) is basically the extension of the jovian ionosphere. Within ~3.8 Rj, the distance variable is therefore primarily R (the distance from Jupiter in spherical coordinates), not L. Currently there is only limited data on the jovian ionosphere and plasmasphere—the Juno mission will hopefully map this region in detail. As a result, except for the region below 8500 km, no changes were made to the basic DG1 model inside 3.8 Rj. However, to provide a means for comparing (and later updating) the ionospheric region between the "surface" of Jupiter (defined as the 1 ATM pressure profile or, mathematically, 1 Rj*(1-0.06487*sin(λ)^2)) and ~8500 km, a simple module has been developed that predicts the cold electron density and temperature in this range. The jovian ionosphere appears to be highly variable, however, and there are a variety of ionospheric profiles to choose from. To provide a starting point for modeling the ionosphere, we chose a representative electron profile based on Yelle and Miller (2004)—the density of this profile was assumed to peak at 2000 km and 2.28e5 cm^{-3} at a temperature of ~0.12 eV. To balance the electron charge, the cold protons were equated to the cold electron densities and temperatures. The detailed profiles for the density and temperature are presented in the Appendices.

3.2.3 Updating the Model: Temperatures for R ≥ 3.8 Rj

Conveniently, the Voyager 1 data overlap the cool torus and warm torus (Sittler and Strobel, 1987). Of special relevance are the Voyager 1 cold electron temperature data (Fig. 13). The observations imply that the cold electron temperatures depart somewhat from the cold ion temperatures in the torus. This difference was fit between 5.3 Rj and 10 Rj with the following formula:

$$T_{ec}(r) = 0.0001862\, r^{5.625} \qquad 5.3\text{ Rj} < r < 7.9\text{ Rj} \qquad (8)$$
$$= 10^{-2.11+0.433r} \qquad 7.9\text{ Rj} < r < 10\text{ Rj}$$

where:

r	=	Distance from Jupiter in the equatorial plane (i.e., the radial distance in cylindrical coordinate); $r=R\cos(\lambda)$

Bagenal et al. (1985) have identified and corrected an error of X2 in their original estimates of the Voyager ion temperatures between 5–10 Rj. As the DG1 model assumed their original values, it was necessary to update the ion temperature values. The Sittler and Strobel (1987) Voyager temperatures used here have been corrected for this issue. The Galileo PLS data are not affected by the Voyager error. To correct the error in the original DG1 model, the DG2 version has adopted the Bagenal and Delamere scale height variation (Eq. (6)) based on the Galileo data and their relationship between the cold ion and proton temperatures (Eq. (7)) for $R \geq 5.5$ Rj. Likewise, the cold electron temperature has been assumed to equal the cold ion temperature for $R > 10$ Rj. These temperature variations are compared to the original DG1 temperature predictions in Figure 21. The DG1 model assumes beyond 7.9 Rj that the

temperature varies from ~15 eV in the plasma disk to 100 eV above the disk. The Bagenal-Delamere model in contrast assumes a uniform temperature in distance above or below the plasmasheet but varying with distance from about 20 eV at 5.3 Rj to ~400 eV at 20 Rj (see Figure 21 and later, for the full-up models, Figure 33). As will be presented, this makes a major difference in the DG1 versus DG2 temperatures and is a significant improvement over the DG1 model predictions of the Voyager data.

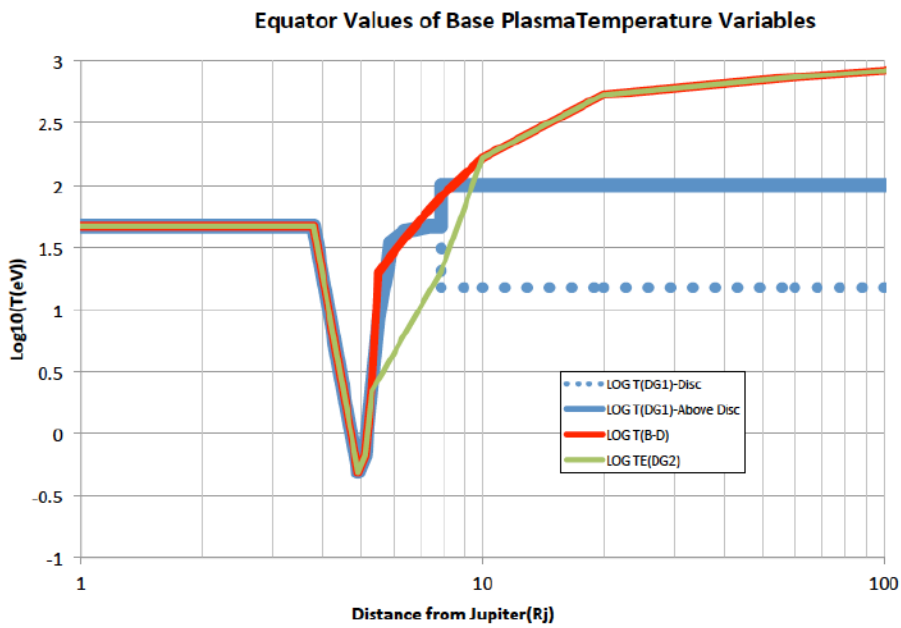

Figure 21. Comparison between the original DG1 cold plasma and electron temperature variations and the new variations for the DG2 model.

In reviewing the cold proton temperature data, it was determined that there were no new data on that component since the DG1 model was developed (see, however, the new ionospheric component Appendix B). As in the DG1 model, it has been equated to the DG2 cold ion temperature. Likewise, there was no new data on the warm proton temperature component so it has been kept constant at 30 keV. Sittler and Strobel (1987) have, however, computed a "hot" electron component—Figure 10. It is assumed here that their "Te_h" is equivalent to the Frank and Paterson (2002) "*Te(warm)*" as the latter has temperatures in the 2–10 keV range also. The two data sets are plotted together in Figure 22. *Te(rms)* and *T(avg)* from Table 5 were assumed for the Galileo values as they best represented a mean temperature for the warm electrons. Also shown is a fit "*Te(W)*" to both the Voyager and the Galileo data:

For:

R < 3.8 Rj: $Te(W) = 46$ eV

3.8 Rj < R < 12 Rj: $Te(W) = 3654\, e^{\left(\frac{R-12}{1.875}\right)}$ (9)

R > 12 Rj: $Te(W) = 10^{-0.0055*R+3.6228}$

where:

Te(W) = Warm (*Te*<10 keV) electron temperature as a function of *R* in Rj

As the Galileo data cover a much broader energy range (~4 eV to ~50 keV) than the Voyager data (1 eV to 6 keV), the former was deemed more appropriate in the outer magnetosphere. Equation (9) explicitly

assumes that the warm electron *Te(W)* approaches the Voyager "Te_h" data inside ~12 Rj. In the absence of any data, it is also assumed that *Te(W)* approaches the cold electron population inside 3.8 Rj. (Note: the determination of the "temperature" here is unfortunately somewhat ambiguous as it depends critically on the energy range over which the data are fit.)

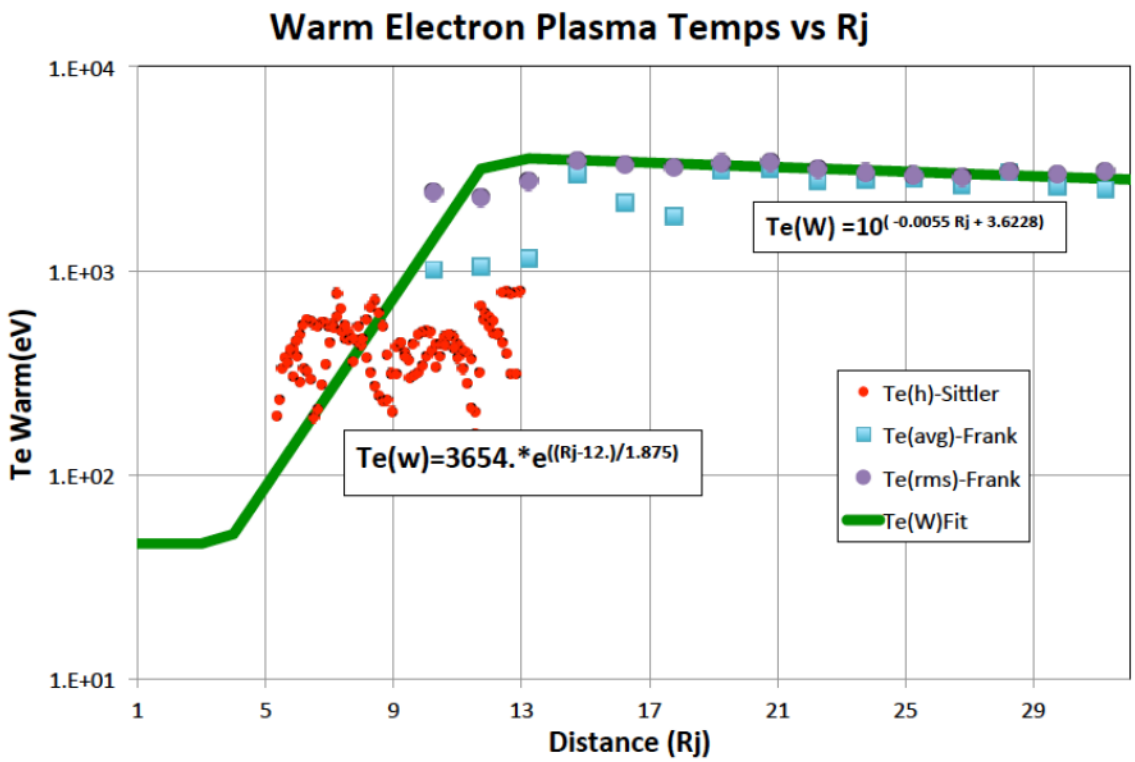

Figure 22. Plot of the warm electron temperatures measured on Voyager 1 (Sittler and Strobel, 1987) and by the Galileo PLS as determined by this study. The latter data have been fit to the Galileo *Tew* Galileo data between ~12–30 Rj (Eq. 9).

3.2.4 Updating the Model: Number Density Variations for R > 3.8 Rj

In the original DG1 model, the cold electron and ion number densities were determined from a careful fit to the Voyager PLS, Planetary Radio Astronomy (PRA), and the Plasma Wave Subsystem (PWS) measurements in the equatorial plane. Figure 12 compared some of those original Voyager measurements to the more recent Galileo (after Bagenal and Delamere's website) number densities. The model fits along the equator for the DG1 and Bagenal/Delamere models are replotted along with a fit by Frank (from Bagenal and Delamere (2011)) in Figure 23 between 1 and 100 Rj. The DG plot is identical along the Equator for both DG1 and DG2. The Bagenal and Frank number density functions are as defined in Bagenal and Delamere (2011). The plots imply that the ion number densities from Galileo and Voyager do not quite agree with the Galileo data (the latter being somewhat lower outside ~15 Rj). Whether this is a temporal variation, computational, or instrumental is not clear. Given, however, that the DG1 curve appears to fit the "maximum" densities (e.g., the equatorial peak values) better than the other models (Figure 12), it was used as the basis of the DG2 equatorial model. To assure charge neutrality, the cold electron number density is set equal to the total ion charge density (not number density) as discussed earlier. The latter is given by Eq. (4)—the cold proton population is not included, however, as it is not well characterized and it was decided to balance it with the warm electrons and protons.

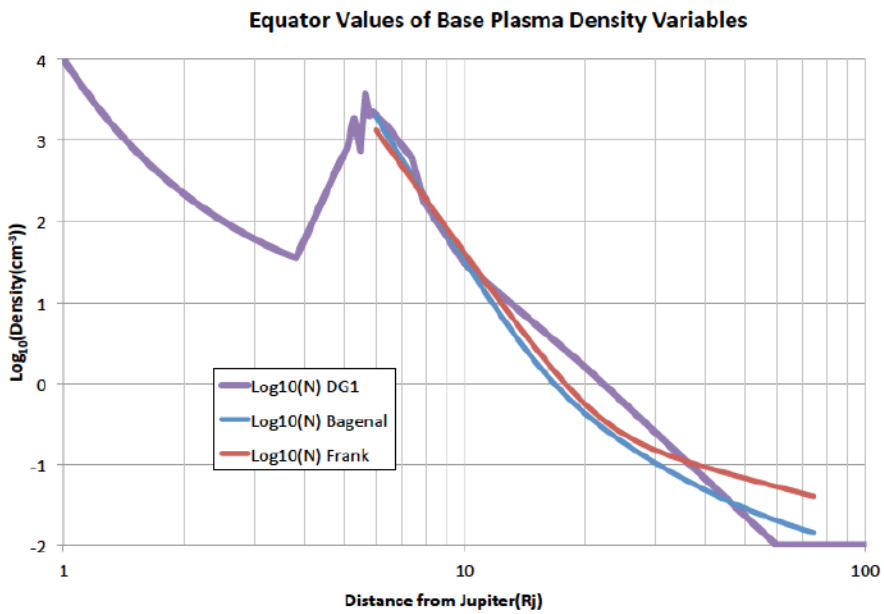

Figure 23. Plots of the ion densities versus Rj for the DG1/DG2, Bagenal, and Frank fits. The Bagenal and Frank fits are defined in Bagenal and Delamer (2011).

As discussed in Section 3.2.1, the number density outside of 5.5 Rj is assumed to decrease exponentially away from the plasmasheet centrifugal equator as defined in Eq. (5). As the cold ion composition also varies differently with species and *R* (Table 1), this leads to some very complex density contours. Several of these are presented in the appendices, and the reader is referred there for various graphical representations.

The next set of density components of the DG2 model to discuss are the cold proton, warm electron, and warm proton densities. As has been discussed, these are the least well modeled of the plasma components. Figure 24 is an updated version of the original Figure 6 in Divine and Garrett (1983) comparing a simple fit to the densities with distance. The original sources are listed in the figure. Figure 25 compares the "new" Voyager 1 (Sittler and Strobel, 1987) data with the Galileo PLS electron data fits (Table 5, *Rtot*). Unlike the "warm" temperatures which have to be derived from two different plasma moment calculations, the "warm" density values, as they are the first plasma moment, are better defined for the two instruments and appear to agree quite well for the 1–10 keV Voyager and 1–50 keV Galileo energy ranges (most of the warm plasma density should be between 5–10 keV).

As should be clear from Figure 25, the original warm proton curve appears to also fit the electron populations. This implies that the warm electron density is approximately equal to the warm proton density. That is, in DG2, the warm proton and electron densities along the centrifugal equator will be assumed to be given by:

For:

1–3.8 Rj: $NeW(R) = 2.44e\text{-}3$ (10a)

3.8–6.565 Rj: $NeW(R) = 10^{0.96\,R-6.26}$ (10b)

6.565-18.335 Rj: (10c)

$$NeW(R) = 10^{1.97736e-6\,R^6-2.1645e4\,R^5+8.83507e3\,R^4-0.173893\,R^3+1.72711\,R^2-8.17198\,R+14.5274)}$$

18.335–48 Rj: $NeW(R) = 10^{1.34326e3\,R^2-\,0.126661\,R+0.434066}$ (10d)

>48. Rj : $NeW(R) = .00281$ (10e)

where:

$NeW(R)$ = warm electron density versus R along the centrifugal equator; cm^{-3}

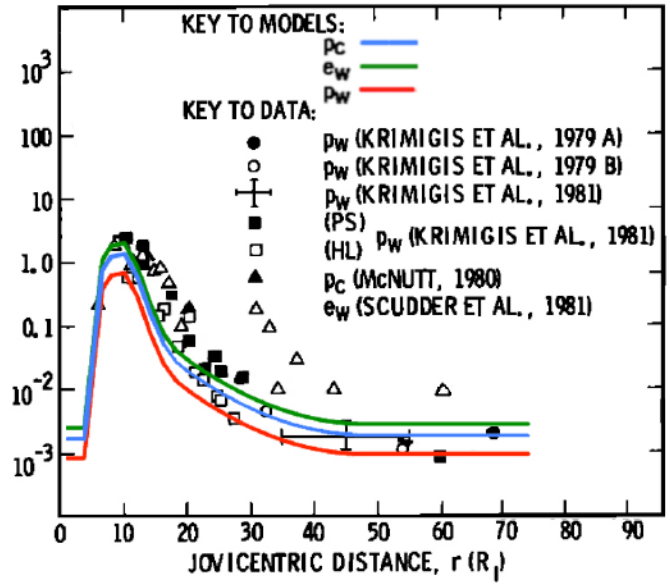

Figure 24. Cold proton, warm proton, and warm electron densities. The figure is an update of Figure 6 in Divine and Garrett (1983). The observations are from Krimigis et al. (1979a,b), McNutt (1980) and Scudder et al. (1981). The model curves are for Eq. 10.

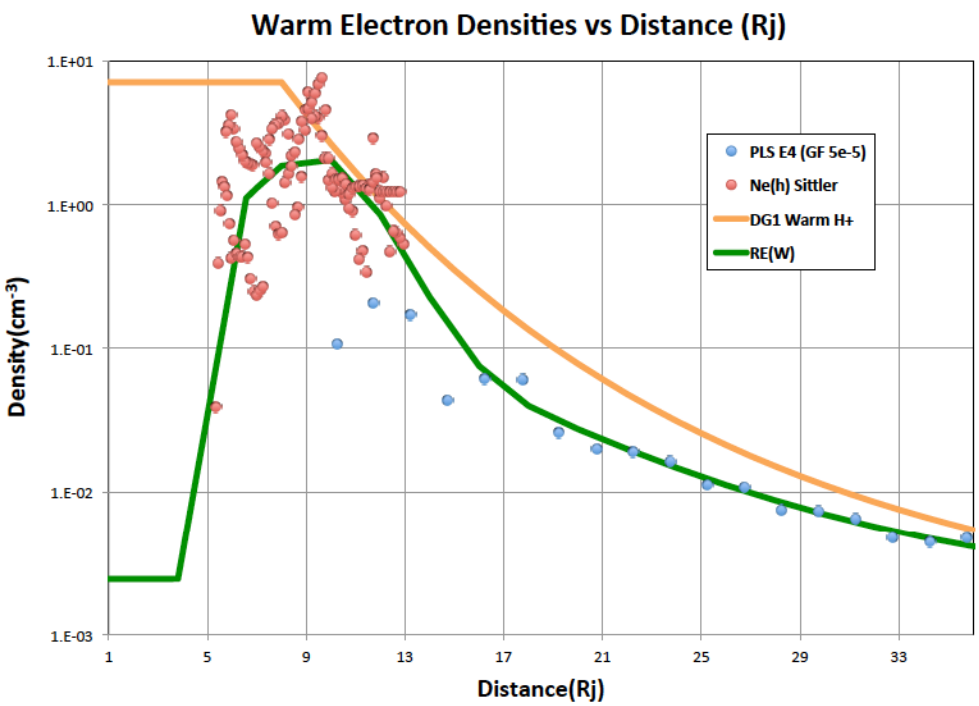

Figure 25. Plot of the warm electron densities measured on Voyager 1 (Sittler and Strobel, 1987) and by the Galileo PLS (as determined in this study). Also plotted are the original warm proton curves from the Divine and Garrett (1983) DG1 (their Eq. 15) and the new DG2 fit (Eq. 10) along the centrifugal equator for comparison.

The density of the cold and warm protons and warm electrons were chosen in DG1 to guarantee charge neutrality with $NpW = 1/3\ NeW$, $NpC = 2/3\ NeW$. As we have no other new data, we have chosen to keep these ratios in DG2 (a few points in Figure 24 from McNutt (1980) appear to support this assumption). We note, however, that the two proton components are really not well defined and might be best set to zero.

As in the case of the other cold plasma components, these densities (warm electrons and protons and the cold protons) are also assumed to fall off exponentially away from the centrifugal equator. These variations off the centrifugal equator are as follows:

For:

1-6.565 Rj: $NeW(Z,R) = NeW(R)$ (11a)

> 6.565 Rj: $NeW(Z,R)=NeW(R)\ e^{(-|Z-Z|/2)}$ (11b)

where:

$NeW(Z,R)$	= warm electron density for $\|Z\| > 0$; cm^{-3}	
Zo	$= R\ sin(\lambda)$	
Z	$= R\ tan(10.77°)\ cos(W_{long}-21°)$	6.565 Rj<R<20 Rj
	$= 20\ tan(10.77°)\ cos((W_{long}-21°)-.015708*(R-20))$	20 Rj<R

The latter variations are adapted from Divine and Garrett (1983) Eqs. 13 and 14.

3.2.5 Updating the Model: Summary

This concludes the discussion of the changes made in DG1 to accommodate new and updated data from the Voyager and Galileo spacecraft. To reiterate, the Voyager data were primarily from Sittler and Strobel (1987) as corrected by Bagenal et al. (1985). The Galileo data were based on extensive studies by Frank and Paterson and their colleagues of the PLS data. Bagenal and Delamere (2011) and at their website (Bagenal and Delamere, 2014) provided a new, very detailed analysis of the Galileo PLS ion data. Several of their fits and the "cleaned" database they provided were used to readjust several of the DG1 parameters. In particular, the ion densities were pinned to their scale height formula. The temperatures were then equated to the scale height variations outside of 5.5 Rj through Eq. (7) as adapted from their model of the ions. This latter change was significant as it implies that the temperature decreases in cylindrical rather than spherical radial distance. The original DG1 model assumed that the temperatures were constant with spherical distance for R > 7.9 Rj but increased from 15 eV to 100 eV as one moved away from the center of the plasmasheet. The Galileo PLS electron data as provided by the PDS between 1–50 keV were carefully corrected for background noise levels and averaged in radial distance in this study to give an estimate of the "warm" electron density and temperature. The latter were used to update the DG1 values for the warm electrons and protons and cold protons. Finally, a simple ionosphere model has been added for altitudes below 8500 km with the intentions of modifying it as data becomes available from Juno.

3.3 Comparisons of the DG2 Plasma Model with Data

Ultimately the utility of a model needs to be tested with respects to the actual data. Unfortunately this is made somewhat difficult in the current situation as the data were derived from several different instruments on missions spanning approximately 30 years. It is hard to distinguish in this study between long-term temporal variations in the jovian plasma, differences in instruments, and differences or errors in the original analyses. On the positive side, except for those specific cases identified in the preceding (e.g., the definition of temperature and the differences in averages between the Voyager and Galileo ion

densities), the plasma parameters overall appear to be consistent between the various spacecraft. To demonstrate this, each of the data sets will be compared with the new DG2 (and DG1) model.

Figures 26 and 27 are plots of the Voyager 1 and 2 cold electron and ion densities versus time (Sittler and Strobel (1987) as adapted from the PDS) compared to the original DG1 and DG2 plasma models. "*RHOE*" is the cold electron density and "*Total ions*" the sum of all the cold ions (including the cold protons). While both models do a good job of fitting the data along the equator (the maximum density should be at the plasmasheet equator), the DG2 model does a much better job off the equator in fitting the Voyager variations (the sudden large impulse early in the Voyager 1 data is believed to be due to the spacecraft being in or near the jovian magnetopause).

Figure 28 compares the Voyager 1 and 2 electron temperatures versus time for the DG1 and DG2 electron and ion temperature predictions during the Voyager flybys of Jupiter. The Voyager data are from the PDS (Sittler and Strobel, 1987). "*TEMP(DG1)*" are the cold ion and electron temperatures for the DG1 model. "*TEMP(DG2)*" and "*TEMPE*" are the cold ion and electron temperatures respectively for the DG2 model. The DG1 values, except near perijove, do not fit the Voyager temperatures very well. The DG2 model in contrast does a good job of fitting the data. Near perijove, the DG2 cold electron predictions (*TEMPE*) fit the Voyager electron data much better than the DG1 predictions.

As presented earlier, Fig. 13 plotted the Voyager 1 electron and ion temperature data (Sittler and Strobel, 1987) as functions of *R*. Also plotted were the Galileo PLS cold ion temperature data (as analyzed by Bagenal and Delamere (2011), see their website). Figure 28 clearly shows the difference between the Voyager electron ("*TEMPE*") and ion ("*Tion(V1)-Sittler*") temperatures (Sittler and Strobel, 1987)—the DG2 fit (Eq. (8)) between 5.3 and 7.9 Rj fits the cold electron data much better than either the DG1 or the Bagenal/Delamere fit (Eqs. (5), (6), and (7)). Conversely, the Galileo and Voyager 1 ion temperature data and the Voyager electron data beyond 7.9 Rj are well fit by the Bagenal/Delamere temperature model (Bagenal and Delamere, 2011).

Figure 29 compares the Voyager PDS electron and ion density data versus distance from Jupiter (Rj). Also plotted are the DG2 estimated density values corresponding to the Voyager locations. Similarly Fig. 30 compares the Galileo PLS ion data (as analyzed by Bagenal and Delamere (2011)). While the DG2 model appears to fit reasonable well, the DG2 model (as it is tied to the Voyager equatorial values) begins to exceed the Galileo data around 10 Rj as observed in Fig. 12.

The "warm" electron and proton components of the DG2 model were compared with data in Fig. 22 (electron temperature) and Figs. 24 and 25 (electron and ion density). Given the issues with the limited data and with the background in the Galileo PLS, the DG2 model appears at least qualitatively to adequately approximate the data that are available.

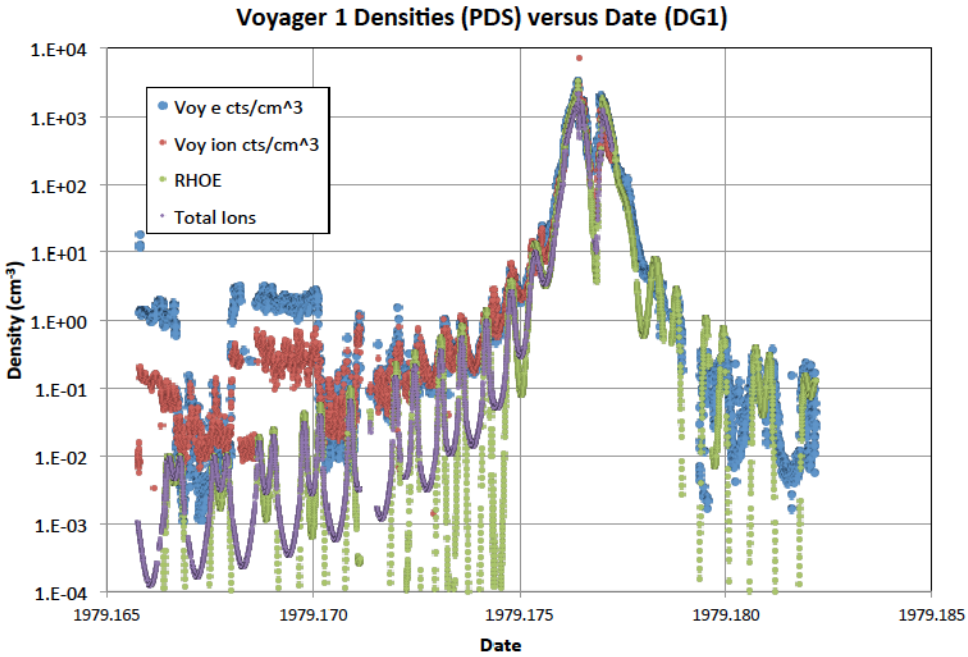

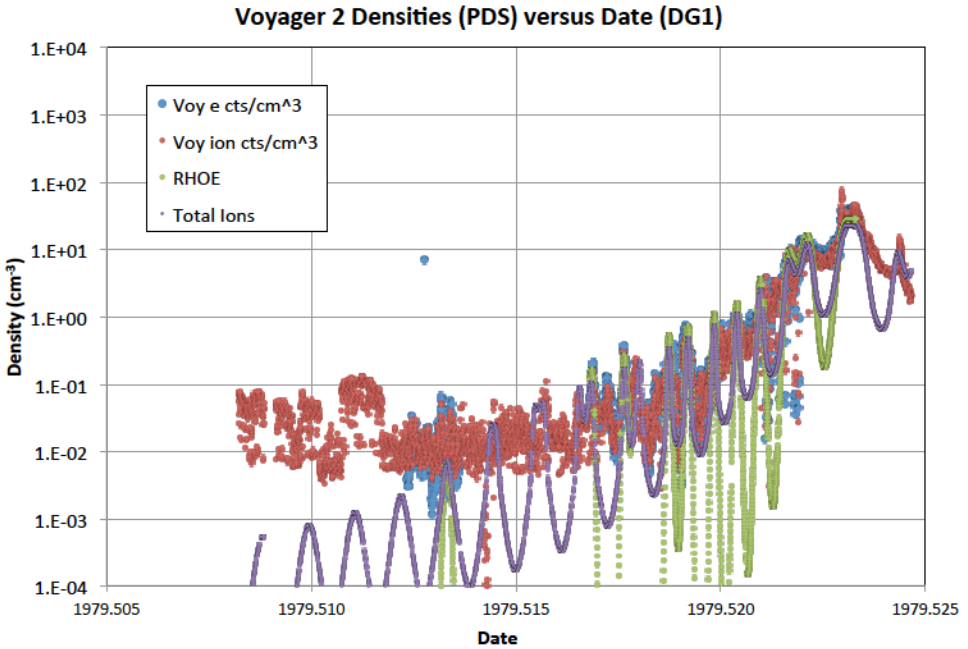

Figure 26. Voyager 1 and 2 cold electron (Voy e) and ion (Voy ion) densities versus time (see Sittler and Strobel (1987) as adapted from the PDS) compared to the original DG1 plasma model. "RHOE" is the cold electron density and "Total Ions" the sum of all the cold ions (including the cold protons).

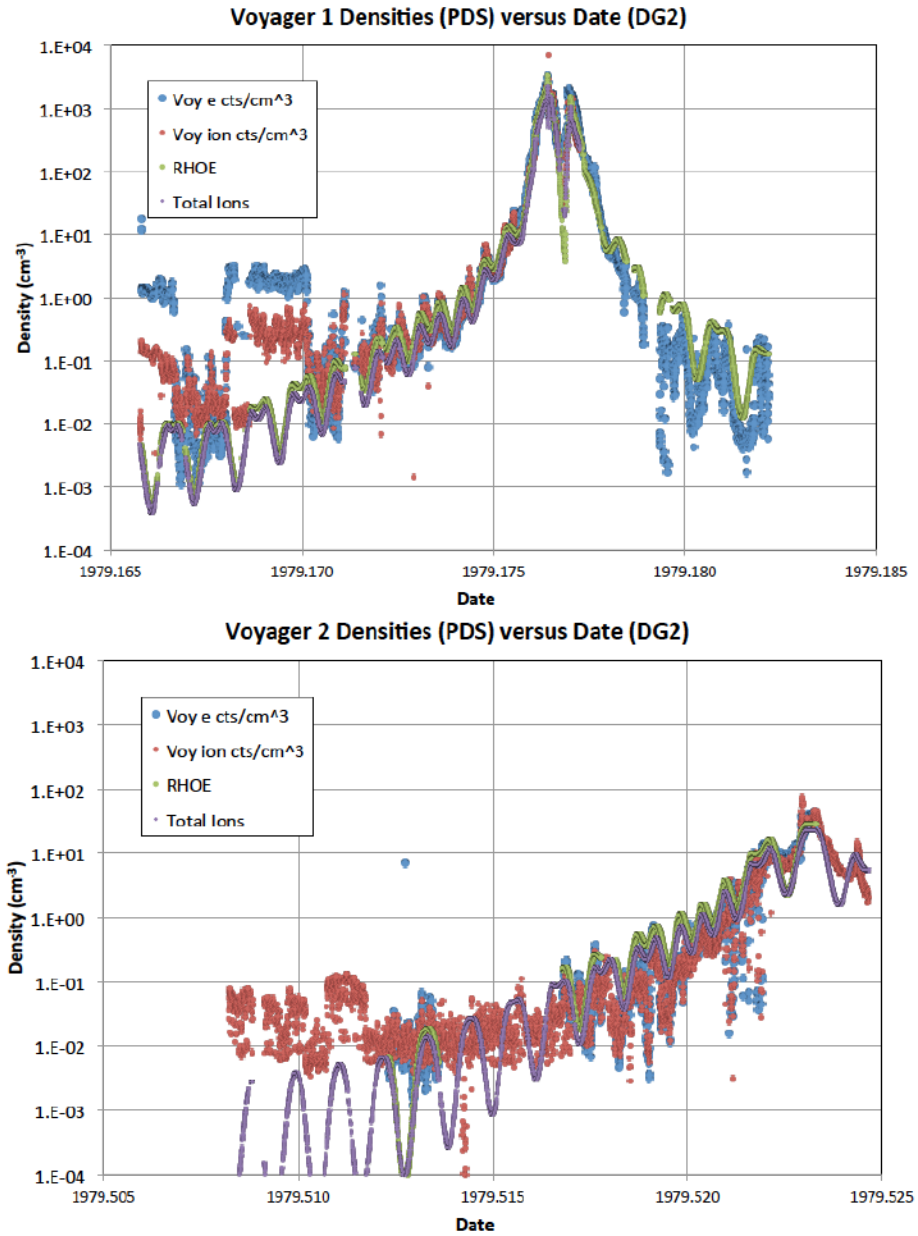

Figure 27. Voyager 1 and 2 cold electron (Voy e) and ion (Voy ion) densities versus time (see Sittler and Strobel (1987); data adapted from the PDS) compared to the new DG2 plasma model. "*RHOE*" is the cold electron density and "*Total ions*" the sum of all the cold ions (including the cold protons).

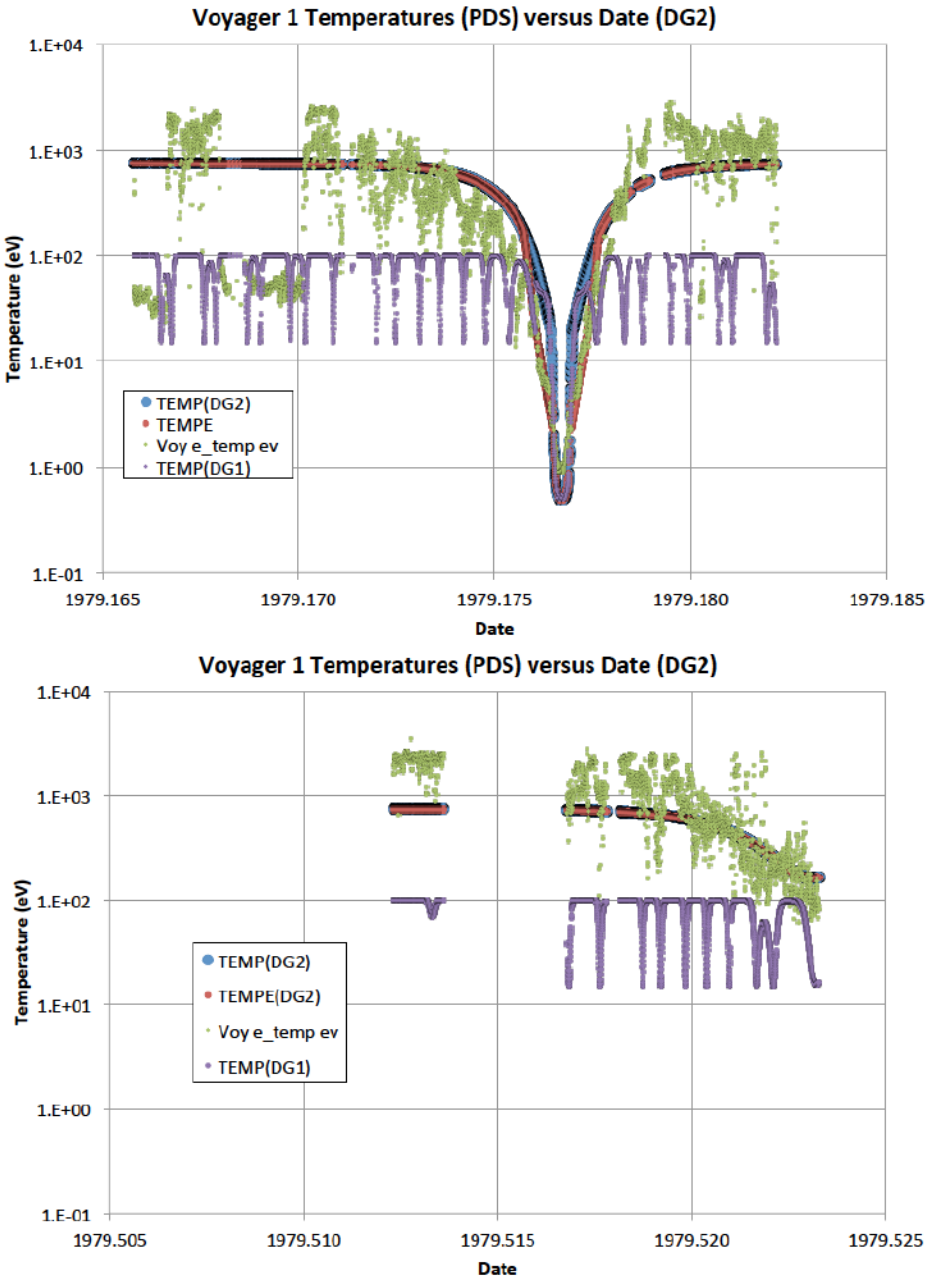

Figure 28. Voyager 1 and 2 electron temperatures versus time compared with DG1 and DG2 electron and ion temperature predictions during the Voyager flybys of Jupiter. The Voyager data (Voy e) are from the PDS (Sittler and Strobel, 1987). "TEMP(DG1)" are the cold ion and electron temperatures for the DG1 model. "TEMP(DG2)" and "TEMPE" are the cold ion and electron temperatures respectively for the DG2 model.

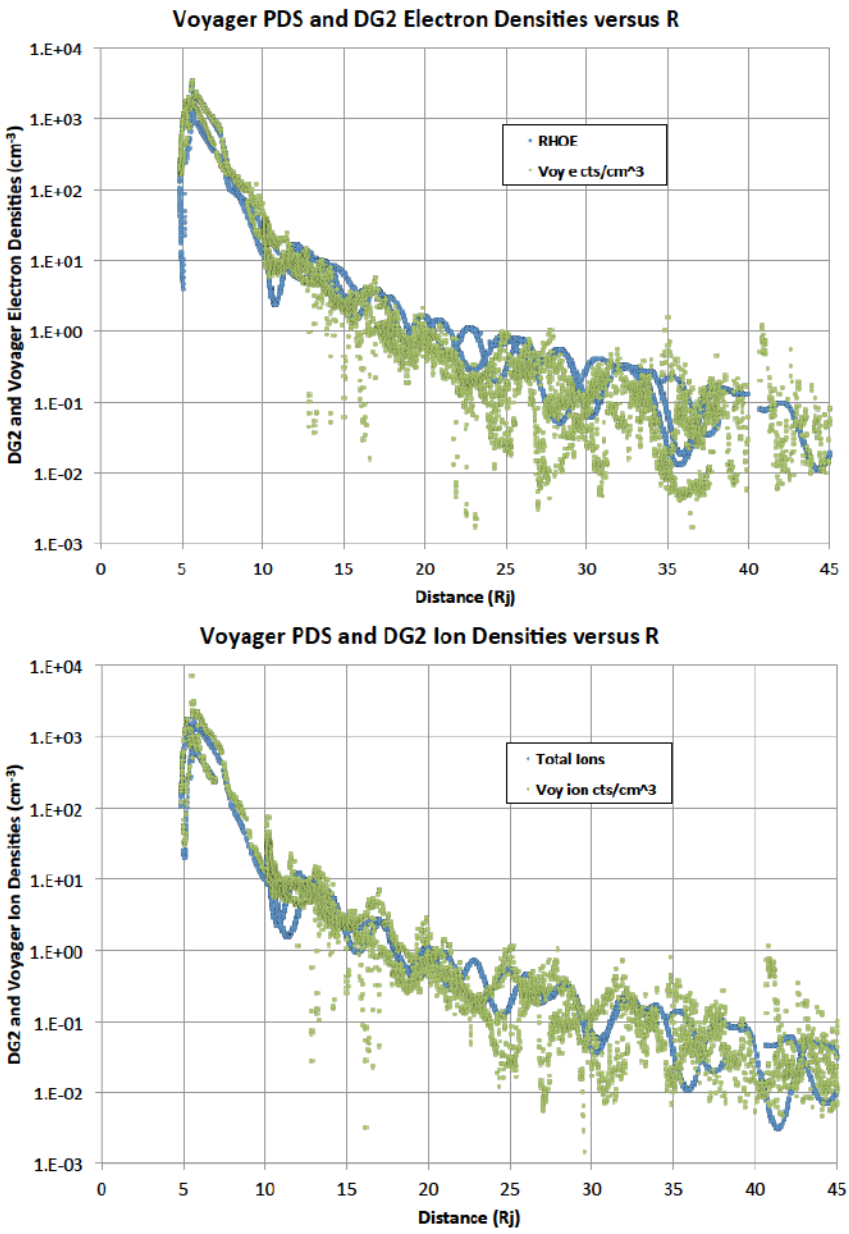

Figure 29. Voyager PDS cold electron and ion data (green dots) and DG2 predictions (blue dots) versus distance from Jupiter (Rj).

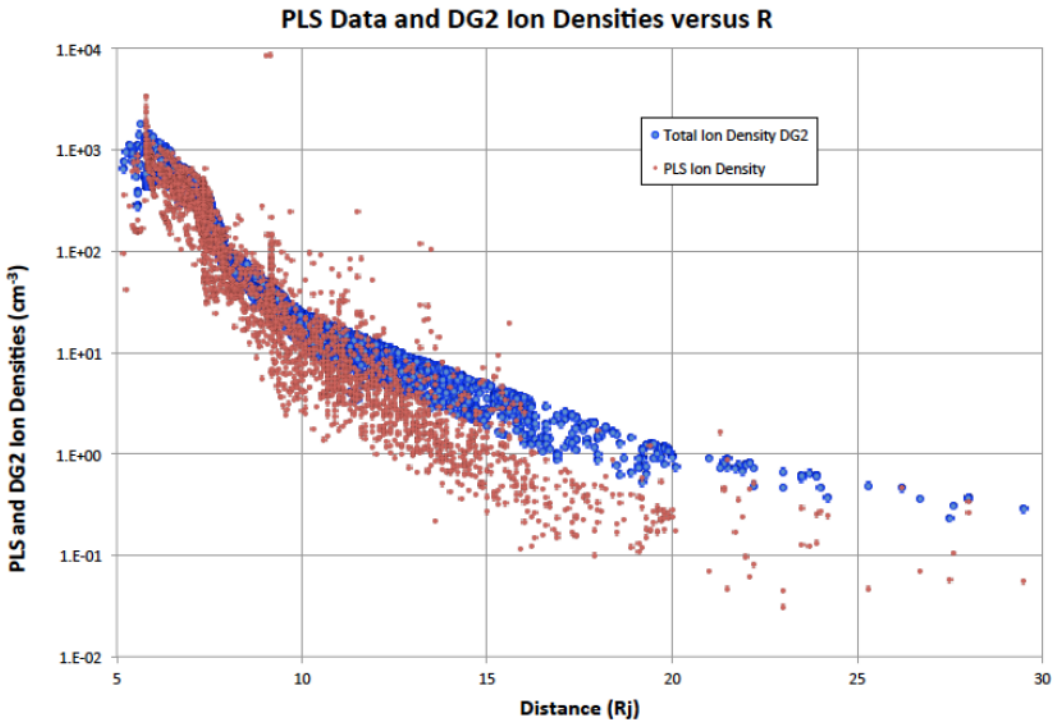

Figure 30. Galileo ion data (Bagenal and Delamere, 2011) and DG2 predictions versus distance from Jupiter (Rj).

3.4 DG2 Model Predictions: Contour Plots

The DG2 model allows not only estimates of the plasma environment along a trajectory but two-dimensional meridional plots that are very useful in understanding the basic properties of the jovian magnetosphere. Figure 31 is an example and shows how the cold electron density varies in latitude and radius for the 110° W System III meridian. Figure 32 compares a similar contour at 110° W for the cold ions (excluding the protons) to a total ion density meridional contour in Figure 33 as suggested by the Bagnel and Delamere (2011) model.

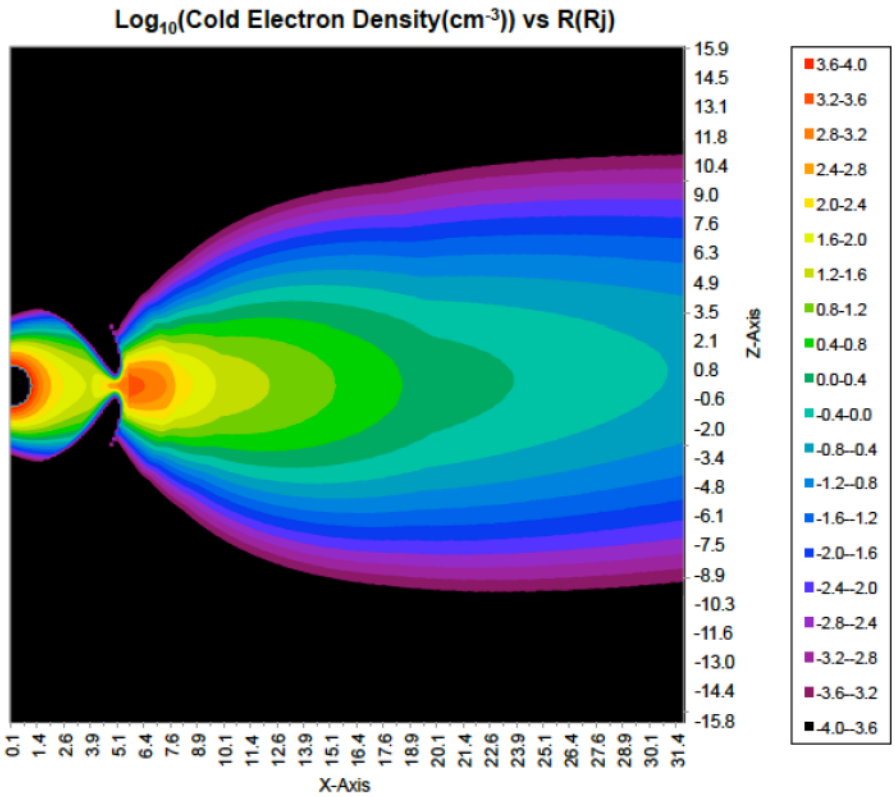

Figure 31. Log_{10} of the Cold Electron Density (cm^{-3}) versus *R*(Rj) at 110° W longitude.

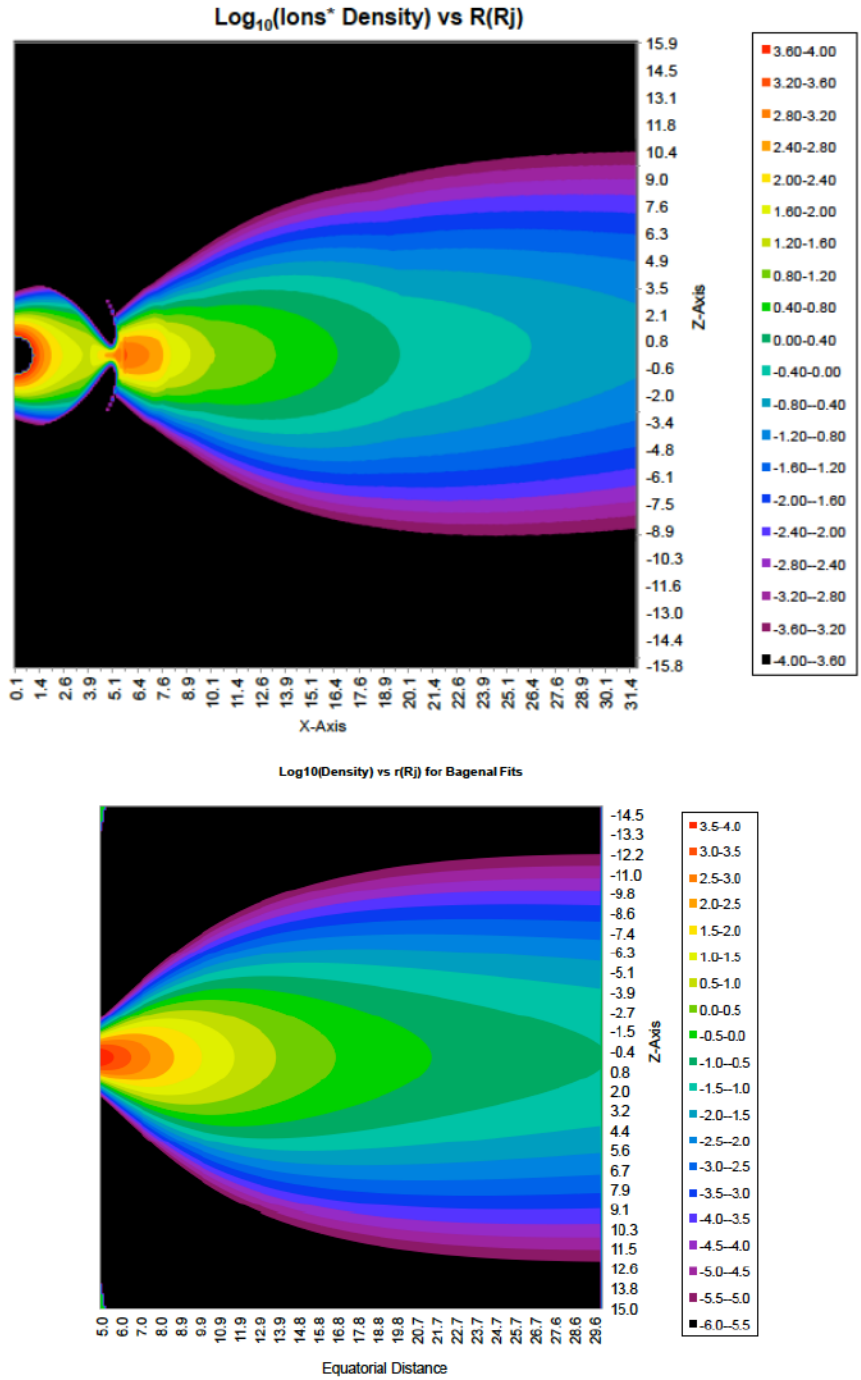

Figure 32. Log_{10} of the Cold Ion Density (cm^{-3}) versus R(Rj) at 110° W Longitude. Top contour is for the sum of the DG2 ions (excluding the protons) while the bottom contour is for an average contour suggested by the Bagenal and Delamere (2011) parameters. Note difference in scales.

Figure 33 compares the DG1 and DG2 cold ion temperature contours for 110° W longitude. The figure demonstrates how different the two models of the ion temperature are in their latitude variations. As discussed, the plasma temperature for R > 7.9 Rj varies with distance above or below the plasmasheet in the DG1 model while the temperature varies radially in cylindrical coordinates in the DG2 model. In the

earlier comparisons with the Voyager data, the DG2 model (based on the Bagenal and Delamere model) appears to better fit the actual data. The reality probably lies between the two limits.

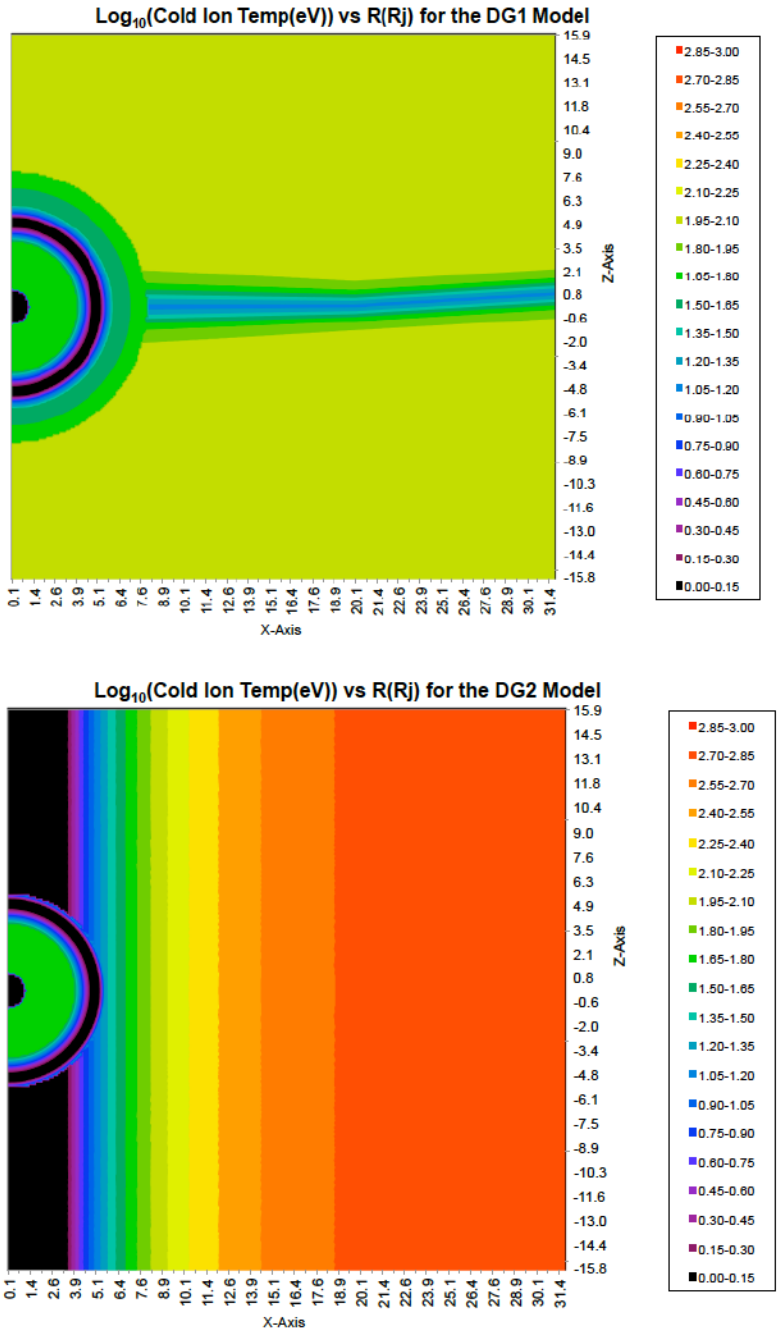

Figure 33. Log_{10} of the Cold Ion Temperature versus R at 110° W Longitude. The top contour is the DG1 ion temperatures while the bottom contour is for the DG2 ion temperatures.

Another useful fit to the electron and proton environments is represented by a Kappa distribution. This environment fit is described by a number density, temperature, and Kappa value (Eq. (2)). The parameter fits to the electron distribution are plotted in Fig. 34. The corresponding proton parameters are presented

in Fig. 35. These Kappa particle distributions will be employed to estimate spacecraft surface potentials—see Figure10 in Garrett et al. (2012) for an example.

Several other contour plots are included in Appendix A, Figs. A1–A8. Of potential interest are the plots of the convection velocity and the cold proton density, and the warm electrons and protons.

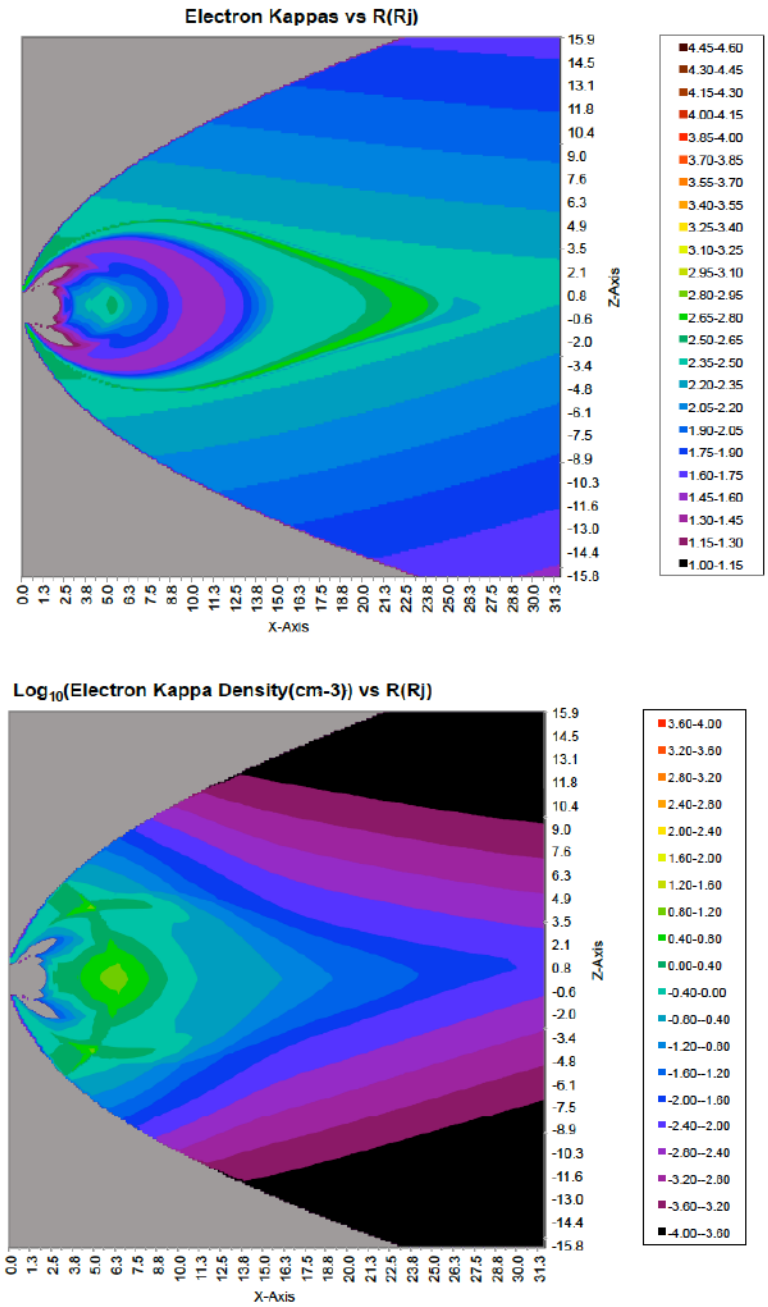

Figure 34. Meridional contour plots of the three electron Kappa plasma distribution parameters (Kappa value, density, and temperature) as modeled by the DG2 plasma model. The gray contours correspond to regions where the program could not fit a Kappa distribution—typically this was where there is no high energy electron data (e.g., outside ~60 L).

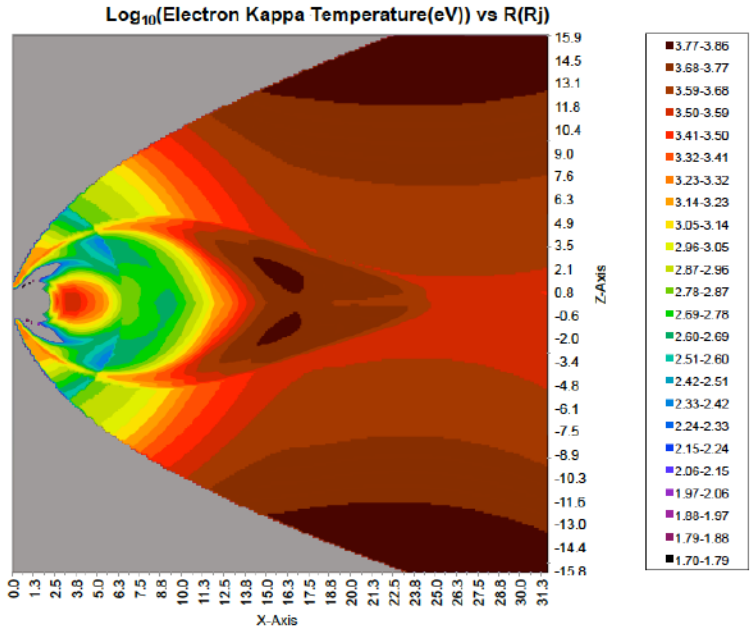

Figure 34. (Continued) Meridional contour plots of the three electron Kappa plasma distribution parameters (Kappa value, density, and temperature) as modeled by the DG2 plasma model. The gray contours correspond to regions where the program could not fit a Kappa distribution—typically this was where there is no high energy electron data (e.g., outside ~60 L).

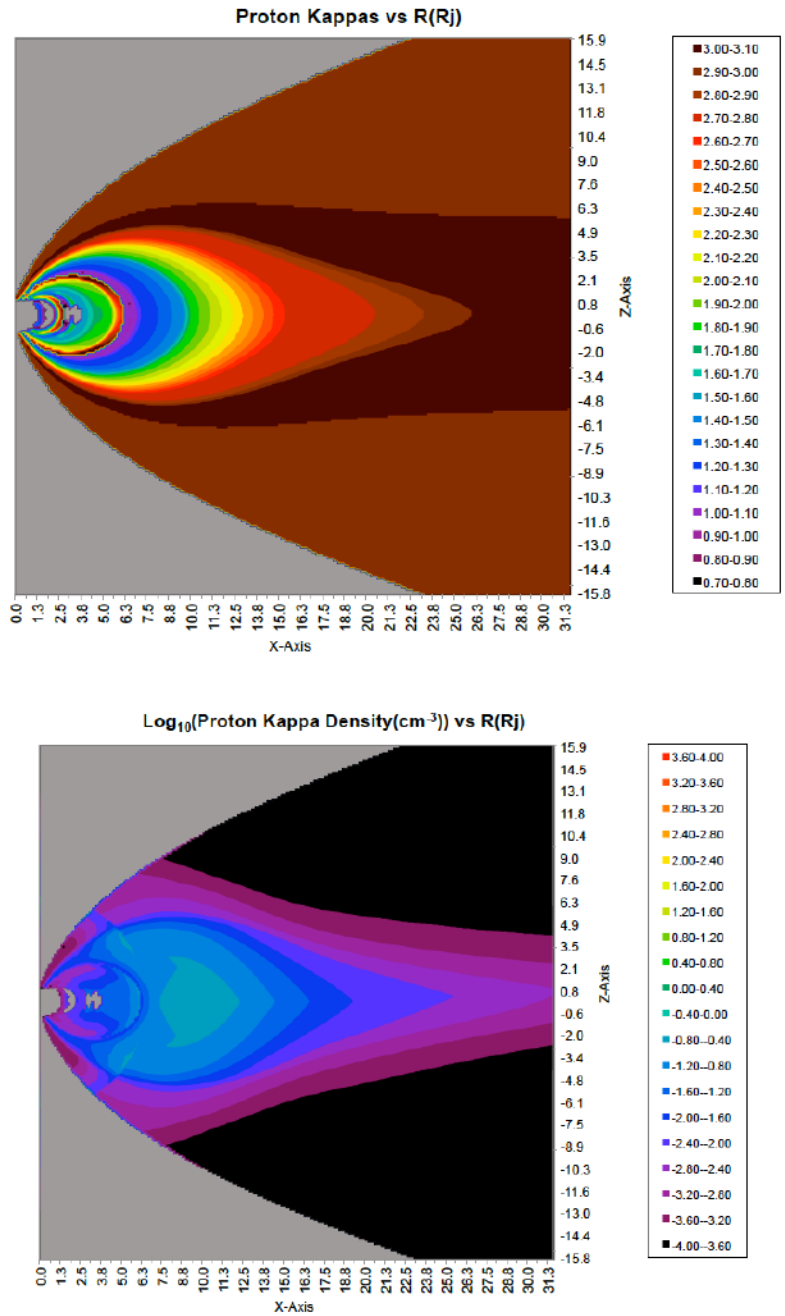

Figure 35. Meridional contour plots of the three proton Kappa plasma distribution parameters (Kappa value, density, and temperature) as modeled by the DG2 plasma model. The gray contours correspond to regions where the program could not fit a Kappa distribution—typically this was where there is no high energy proton data (e.g., outside ~60 L).

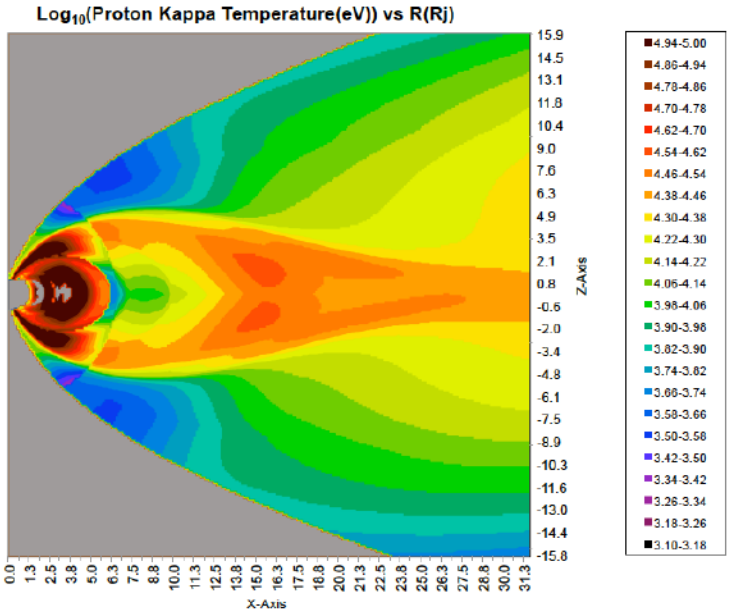

Figure 35. (Continued). Meridional contour plots of the three proton Kappa plasma distribution parameters (Kappa value, density, and temperature) as modeled by the DG2 plasma model. The gray contours correspond to regions where the program could not fit a Kappa distribution—typically this was where there is no high energy proton data (e.g., outside ~60 L).

4 THE AURORAL ELECTRON FLUX

In addition to the background plasma, which typically dominates the charging environment, the 10–100 keV auroral electron environment has to be defined to accurately compute surface potentials. The auroral electron currents need to be determined for those times when a spacecraft is on magnetic field lines connecting to the auroral zone as these can represent the periods of highest negative potential. Unfortunately, there are only very limited data on the actual auroral particle fluxes at Jupiter. Aside from passes over Io, Europa, and Ganymede and in the equatorial plane by the Voyagers and Galileo, the only "in-situ" data pertinent to aurora are UV and IR optical observations in the jovian upper atmosphere. These optical observations, based on theoretical arguments, have been inverted to provide predictions of the auroral electron fluxes at the base of the flux tube/field lines in the atmosphere. A particularly useful reference in this regard is that of Ajello et al. (2001). The Ajello paper presents a comprehensive model of the jovian auroral emissions and the electron fluxes necessary to produce them. For the purposes of this study, Ajello et al. (2001) provides two representative "in-situ" estimates of the incident auroral electron fluxes (Figs. 36a and 36b). Ajello et al. (2001) assumed two types of distributions and then adjusted the characteristic energies and energy fluxes to match the optical observations. Figure 36a assumes an incident flux given by a single Maxwellian distribution (Eq. (1)) having a characteristic energy of 25 keV and a density of 1 cm^{-3} giving an energy flux (Q) of 65 ergs/cm^2-s. The second functional form, Fig. 36b, assumes a sum of 3 Kappa distributions (Eq. 2) with characteristic energy fluxes of 20, 30, and 50 ergs/cm^2-s. The Maxwellian and Kappa distribution parameters are listed in Table 7. Here we assume that these fluxes propagate down along the field line to the equator and, in the absence of loss mechanisms, provide a "worst case" estimate of the equatorial auroral fluxes. The aurora are, however, highly variable and their fluxes come and go frequently between ~15–30 Rj.

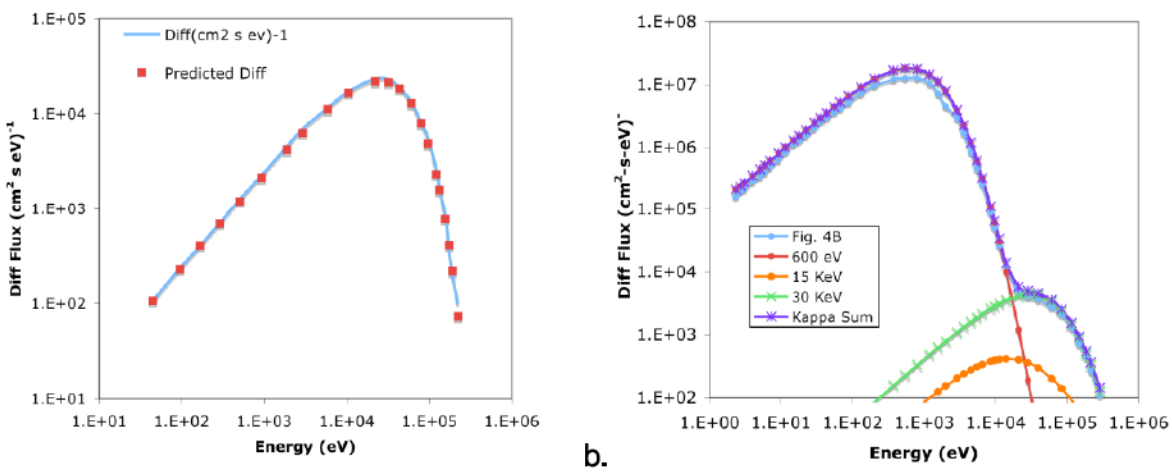

Figure 36. Plots of auroral electron fluxes incident on Jupiter's upper atmosphere as estimated by Ajello et al. (2001). A) A Maxwellian distribution function fit (Eq. (1)); B) A 3 Kappa distribution fit (Eq. (2)).

Table 7. Fits to predicted auroral oval electron fluxes for Figure 36: (a) Maxwellian distribution, (b) Kappa distributions, and, (c), for Kappa fits to the diffuse aurora over the polar caps (Figure 37) at various distances along the equatorial plane.

(a) *Maxwellian Aurora*

ρ_E	T_E	
0.57	25000	

(b) *Kappa Aurora*

ρ_{EK}	T_{EK}	κ
82.5	600	7
0.0126	15000	2.1
0.14	30000	7

(c) *Diffuse Aurora*

Rj	ρ_{EK}	T_{EK}	κ
1.2	5.20	800	2.50
2	6.00	1500	3.00
15	2.00	1500	2.40
25	0.30	3200	2.40

In addition to the aurora in the narrow auroral zone, Figure 3 indicates the presence of somewhat dimmer, diffuse aurora over the polar cap. Bhattacharya et al. (2001) estimated these diffuse polar auroral fluxes assuming that the plasma distributions measured between 15 Rj and 30 Rj at the jovian equator by Galileo are representative of the particle fluxes along a jovian magnetic field line (note, particle losses/sources and acceleration mechanisms can alter this assumption). Figure 37 (adapted from Figure 2 of Bhattacharya et al. (2001)) is their estimate of the diffuse spectrum at ~18.4 Rj in the jovian equatorial plane. The fit parameters for the high energy electron spectrum are noted in the figure. Based on other Galileo data, Bhattacharya et al. (2001) observed that the electron energy flux can at times reach ~100 ergs/cm^2-s at 15 Rj but then falls to ~10 ergs/cm^2-s at 25 Rj. To approximate a "worst case" diffuse aurora for charging estimates based on these findings, Garrett et al. (2008) assumed an energy flux of ~100 ergs/cm^2-s. The "warm" electron distributions from the DG1 model were then linked with this distribution to provide a set of "worst case" Kappa distributions for electrons from 1 eV to 1 MeV over the polar cap and in the 15–25 Rj equatorial region.

Summarizing the above, Table 7 tabulates the final "worst case" estimates of the electron auroral environment for the jovian auroral zone (assumed to be ±5° around the bright north and south auroral zone center lines in Figure 3a) and the polar diffuse aurora at higher magnetic latitudes. Table 7 assumes either the auroral electron spectra of the Ajello et al. (2001) Maxwellian (Case a) or multiple Kappa distributions (Case b) for the auroral zone or the diffuse aurora (a combination of Figure 36 and the appropriate "warm" electron environments of Divine and Garrett (1983)) over the polar caps.

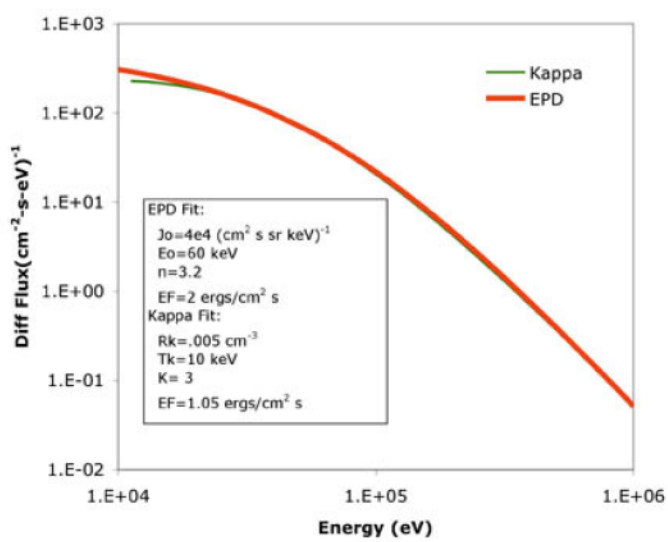

Figure 37. Omni-directional energy spectrum for the diffuse aurora (based on Eq. 1 in Bhattacharya et al. (2001)) at 18.4 Rj in the equatorial plane as measured by the Galileo Energetic Particle Detector(EPD) instrument.

5 NASCAP-2K SPACECRAFT CHARGE MODEL UPDATES

5.1 Overview

Surface charging is a potential concern for all spacecraft at Jupiter as the plasma environment between L~15–25 is subject to intense and highly variable auroral electron fluxes (these L-shells delineate the main energetic auroral region as discussed earlier). Estimates of the surface potentials along these L-shells range from a few volts positive to several kilovolts negative. Since differential potentials in excess of 100 V are suspected of causing arcing on spacecraft surfaces, the mitigation of such differential potentials is a serious concern for jovian missions, particularly for ones with large solar arrays like Juno or the proposed Europa mission. To estimate these differential potentials, Nascap-2K was used as the tool of choice. Nascap-2k is an advanced spacecraft charging code that has been successfully used for a variety of spacecraft charging simulations. The auroral distribution functions currently available in the Nascap-2k program, however, are limited to Maxwellian distributions for low energy particles and Fontheim distributions for high energy electrons. The latter distribution is the sum of a Maxwellian, a power law spectrum, and a Gaussian distributions and is intended to approximate an auroral distribution. Figure 38 compares a Fontheim distribution (Fontheim et al., 1982) to the corresponding jovian auroral distribution of Ajello et al. (2001)—the "3 Kappa distributions" presented earlier. While the Fontheim distribution approximates the 3 Kappa distributions, there are significant small scale differences. The purpose of this study task was to incorporate Kappa distributions into the Nasap-2k program and to compare the differences between the spacecraft potentials estimated by the different distributions. Nascap-2k was then used to estimate the effects of the jovian plasma environment on two potential Europa mission designs—one using radioisotope power systems (RPS) and the other large solar arrays.

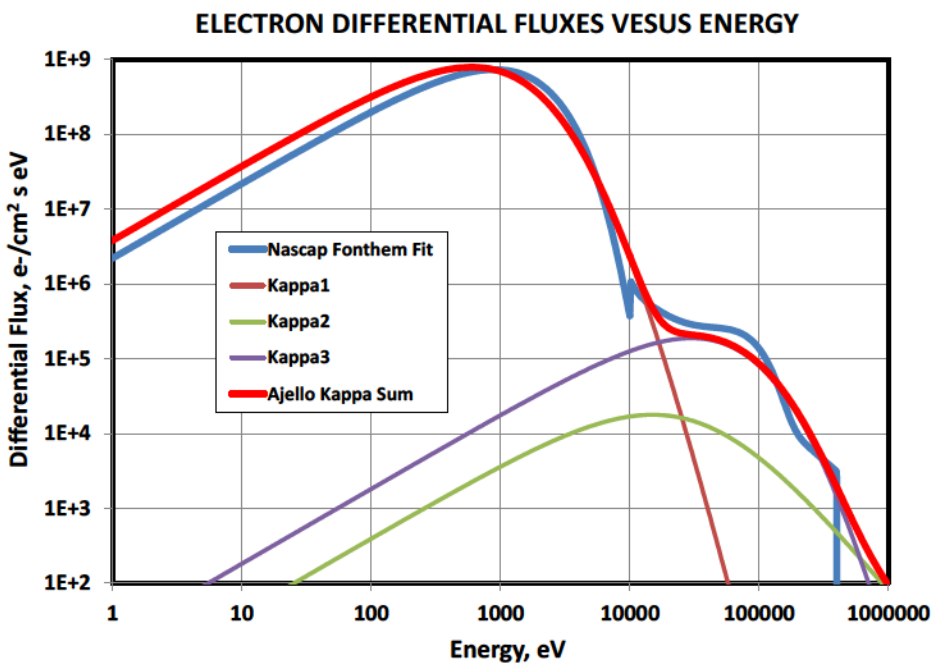

Figure 38. Fits to the electron differential fluxes for the jovian aurora as defined by Ajello et al. (2001) in Figure36b. The Kappa fits are as described earlier. Also plotted is the Nascap-2k Fontheim distribution (sum of a Maxwellian, a power law spectrum and a Gaussian distributions) fit to the Ajello et al. spectrum.

5.2 Incorporation of Kappa Distributions into NASCAP-2K

Over the summer of 2014, B. Belland (JPL Summer Intern) modified the Nascap-2k code to incorporate multiple Kappa distributions into the tool. The detailed modifications and steps necessary to include them are detailed in Belland (2014). These consisted of two steps: 1) modify the Nascap-2k code so that it could accept user-input Kappa distribution parameters and 2) verify whether the results of the modification match expectations. These two steps are described in the following.

The first step was to modify the Nascap-2k code. This consisted of reviewing the source code for Nascap-2k (written in Java, C++, and Fortran) and determining what parts of the code needed to be changed. The electron thermal current and ion thermal current, the secondary electron current due to ions and electrons, and the backscattered electron distributions were all dependent on the distribution input parameters as indicated in the graphical user interface (GUI) shown in Figure 39. The C++ codes corresponding to Kappa distributions were added to the Auroral Environment section, and the Java codes were modified to make inputting Kappa distribution parameters through the GUI possible. Figure 40 illustrates the final product showing how the Kappa components have been added to the GUI.

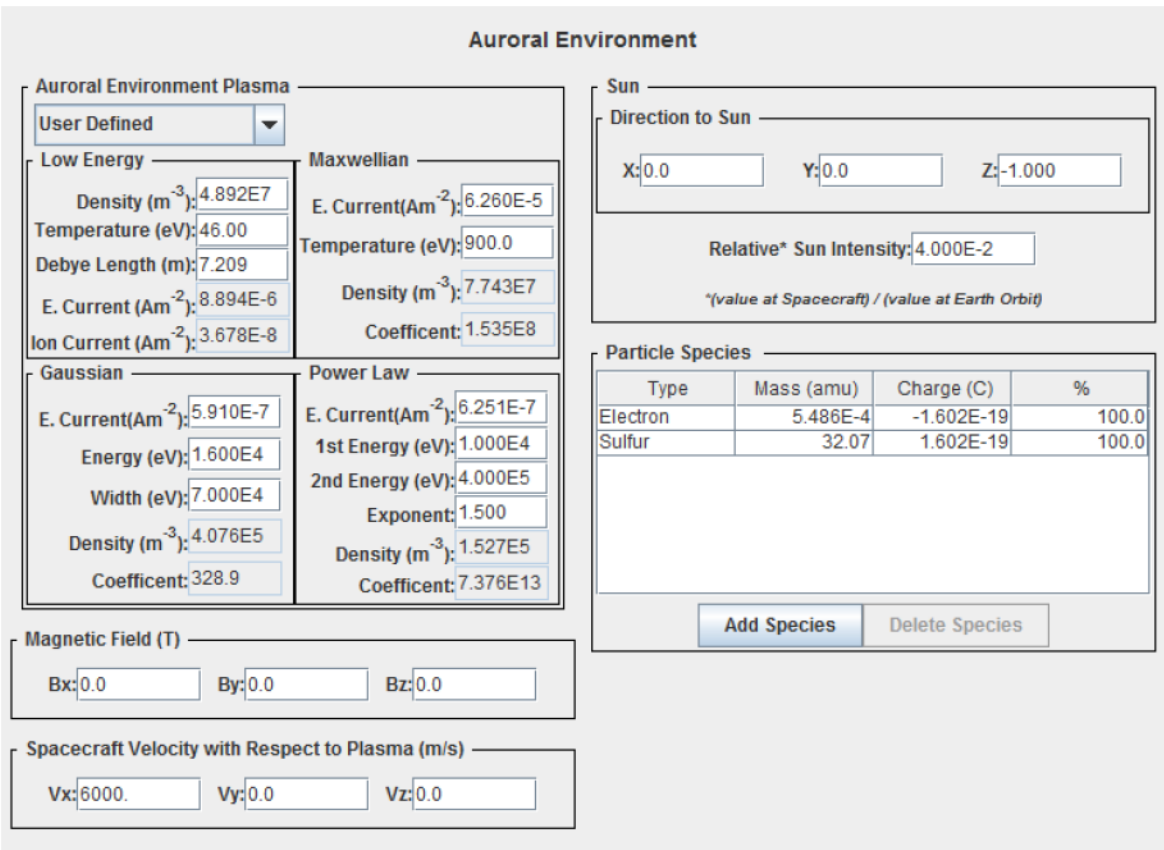

Figure 39. The Nascap-2k Auroral Environment parameter input screen before modification.

To verify that the Kappa distribution added to the auroral environment worked, the potentials on a simple spacecraft due to single electron Kappa distribution were calculated. The potential due to the newly added Kappa distribution in the auroral environment" was compared with an estimate using the Kappa distribution in the "GEO Plasma Environment" (e.g., geosynchronous orbit) Nascap-2k program section (note: Earth's geosynchronous orbit represents a standard spacecraft charging test environment). The latter was available in a previous Nascap-2k version with exactly same Kappa parameters. An example file "GeoChargingKappa", which came with the installation package, was used. (Unfortunately, the

Kappa distribution function in "GEO Plasma Environment" cannot be used with other environments such as Maxwellian distribution, Fontheim distribution, or another Kappa distribution.) The results were found to be identical confirming the accuracy of the new program module.

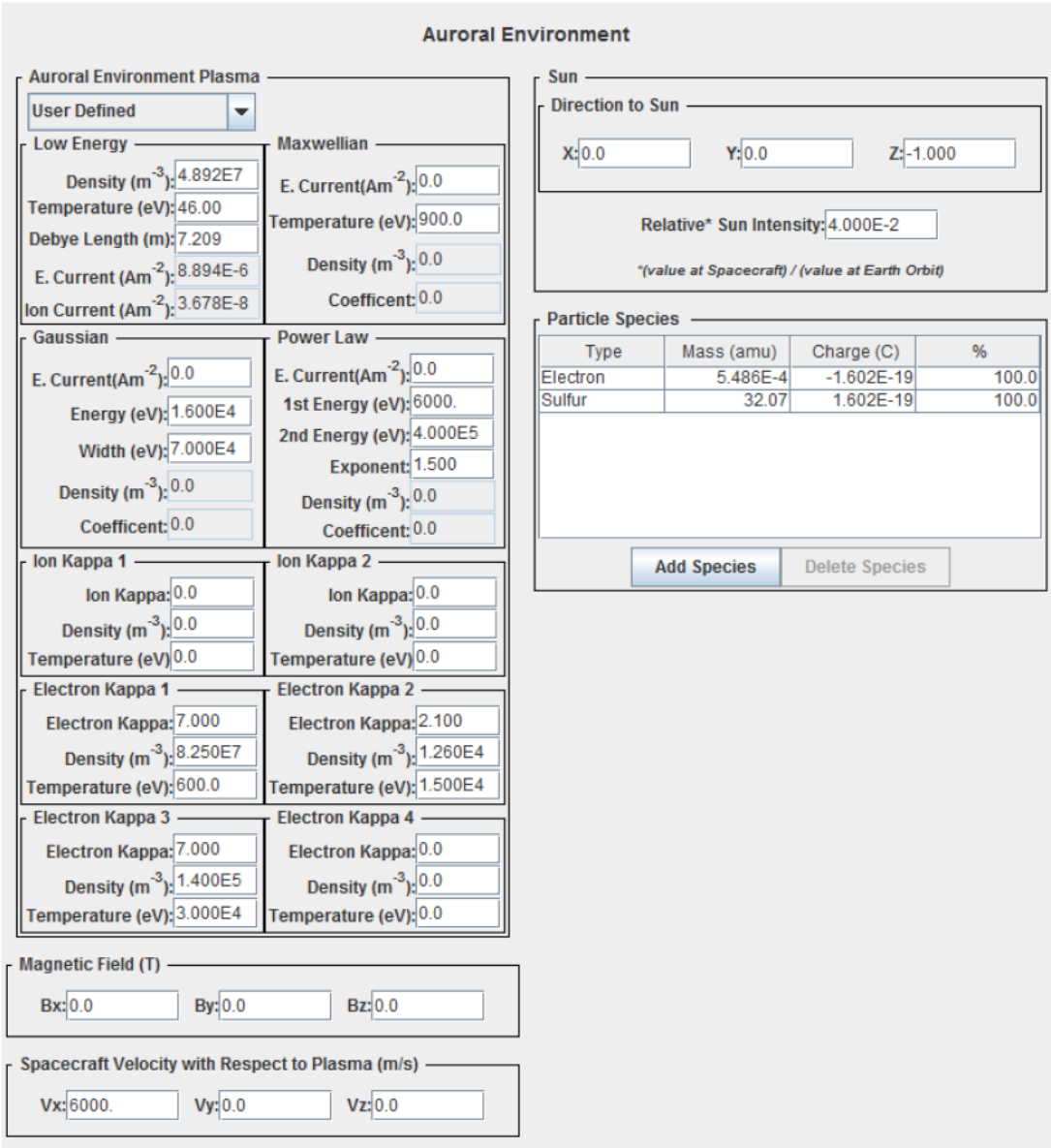

Figure 40. The modified Nascap-2k Auroral Environment parameter input screen with additional Kappa parameter input boxes as added. Up to four electron Kappa distributions and two ion Kappa distributions can be modeled in addition to the pre-existing Fontheim distribution.

Also, the variations due to the differences between the Ajello three Kappa distribution model (Garrett et al., 2008) and the Ajello Fontheim model for the Jovian plasma (Fig. 38) were studied. The latter parameters were updated to units compatible with the latest version of Nascap-2k. Figure 41 compares the results for the Fontheim and the three Kappa fits using the input parameters in Figs 39 and Figure 40, respectively. The results are similar but there are (as would be expected) small differences in the final potential and time profiles between the Fontheim and the three Kappa distributions. Comparisons for other ranges of parameters show other minor variations between the two distributions. For now it should

be noted, however, that the Kappa fits have the advantage of being continuous whereas the Fontheim distribution has small discontinuities as illustrated in Fig. 38. Indeed, it may be these discontinuities that cause the Fontheim distribution to sometimes generate unstable time profiles.

To summarize, the Kappa distribution was added to the "Auroral Environment" component of the Nascap-2k model. The results were identical when compared to Nascap-2k's GEO environment using the single electron Kappa distribution. It was also tested for a Juno case in the jovian auroral environment. In comparison tests, it and the Fontheim distribution produced comparable results.

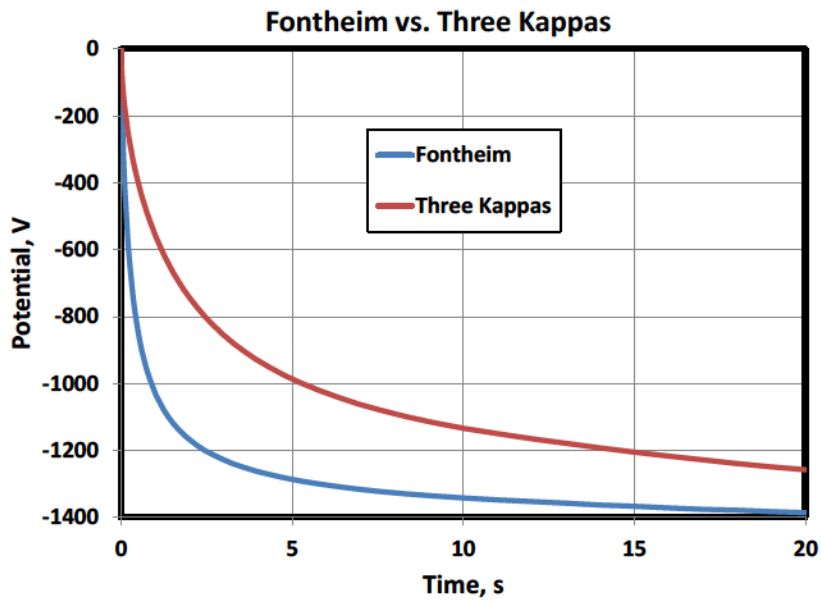

Figure 41. Comparison between the Ajello 3 Kappa distribution and the Fontheim approximation. The spacecraft potentials versus time are plotted.

5.3 NASCAP-2K Europa Clipper Charging Computations

In the final task of this project, the modified Nascap-2k tool was used to analyze the charging of two different models of a possible Europa mission spacecraft—a version powered by an RPS and another version powered by a large solar array. A jovian auroral environment at 15 Rj from Garrett et al. (2008) was used for the simulations. Figure 42 is a three-dimensional plot by Nascap-2k of the RPS version. The spacecraft is shown covered in conductive black Kapton with two small non-conductive material (Teflon) test patches. The black Kapton is assumed to have a secondary emission coefficient (δ_{max}) of 2.1. This is the default value in Nascap-2k for (yellow) Kapton (the meaning of δ_{max} is explained in Fig. 43 and is the maximum secondary electron yield versus impact energy for a given material). Figure 44 is for the same design, only with $\delta_{max} = 0.87$ as actually measured in the laboratory by J. R. Dennison and associates at Utah State University—this value is also supplied by Nascap-2k in a separate 'materials' file. The potential for the $\delta_{max} = 2.1$ was ~+2 V whereas, for $\delta_{max} = 0.87$, the potential reaches –1650 V. The RPS spacecraft potential is thus *very* sensitive to the black Kapton secondary emission material properties—a potential concern for any Europa design where charging is an issue.

Figure 45 is a similar plot for a Europa spacecraft with a solar array configuration. The spacecraft is again assumed to be covered by black Kapton (with $\delta_{max} = 0.87$). The solar panel surfaces (e.g., the coverglass) are, however, assumed be coated with a special conducting material, indium tin oxide or ITO ($\delta_{max} = 2.47$, Krainsky et al., 1980), to reduce differential surface potentials. The spacecraft potential is again ~+2 V. The ITO's maximum secondary electron emission yield was then varied to see how it affected the spacecraft potential. The behavior is illustrated in Fig. 46. Again, the spacecraft

potential is extremely sensitive to the secondary electron yield varying from ~2 V to -1100 V as the maximum yield, δ_{max}, goes from 2.47 to 1.00.

To summarize, from the NASCAP-2K surface charging analyses:

- Changing the design from the RPS to the solar array has a significant effect on the surface charging pattern over the spacecraft.
- The spacecraft potential in each case is very sensitive to the ITO's maximum secondary electron emission yield.

These results indicate that the material charging properties must be carefully determined and verified if accurate estimates of the spacecraft potentials are to be made. Also it is known that the charging properties of materials change significantly due to the surface contamination over time. Further laboratory testing is called for.

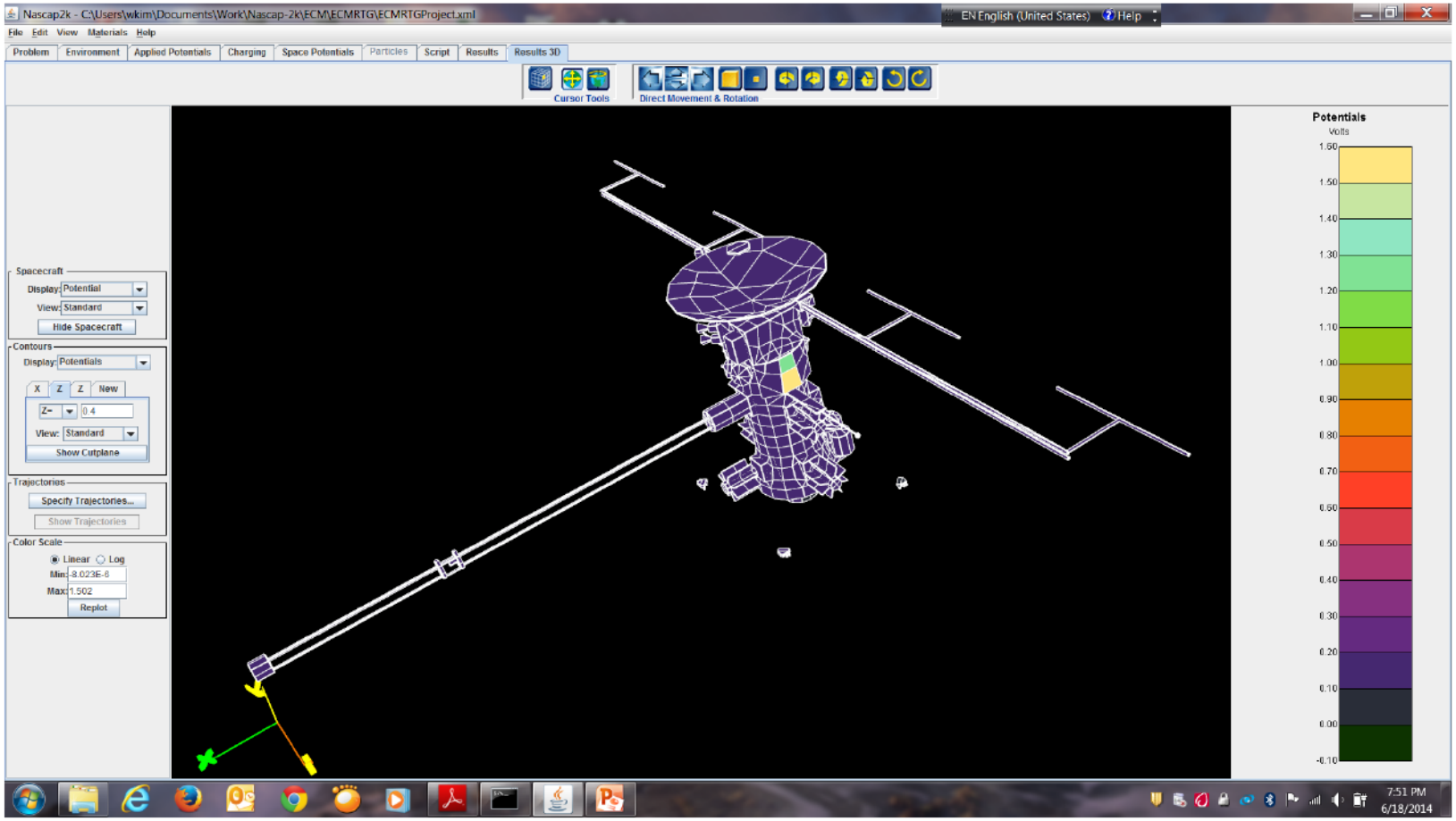

Figure 42. Three-dimensional Nascap-2k plot of an RPS-powered Europa spacecraft design concept showing the differential surface potentials. The surface material is covered in the default conductive black Kapton with δmax = 2.1.

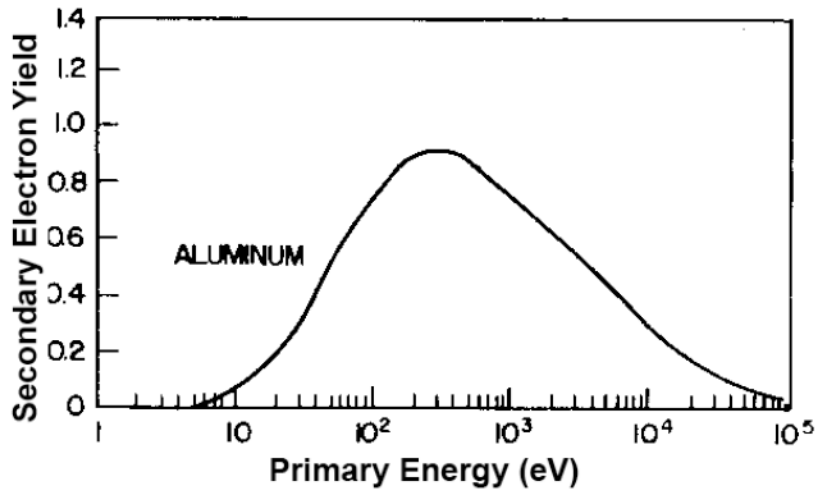

Figure 43. Sample secondary electron emission yield curve for Aluminum, δ_{max} = 1.00 showing how the secondary yield change with incident electron energy. The secondary electron yield is the number of electrons emitted from a surface for each energetic electron impacting the surface at the indicated energy.

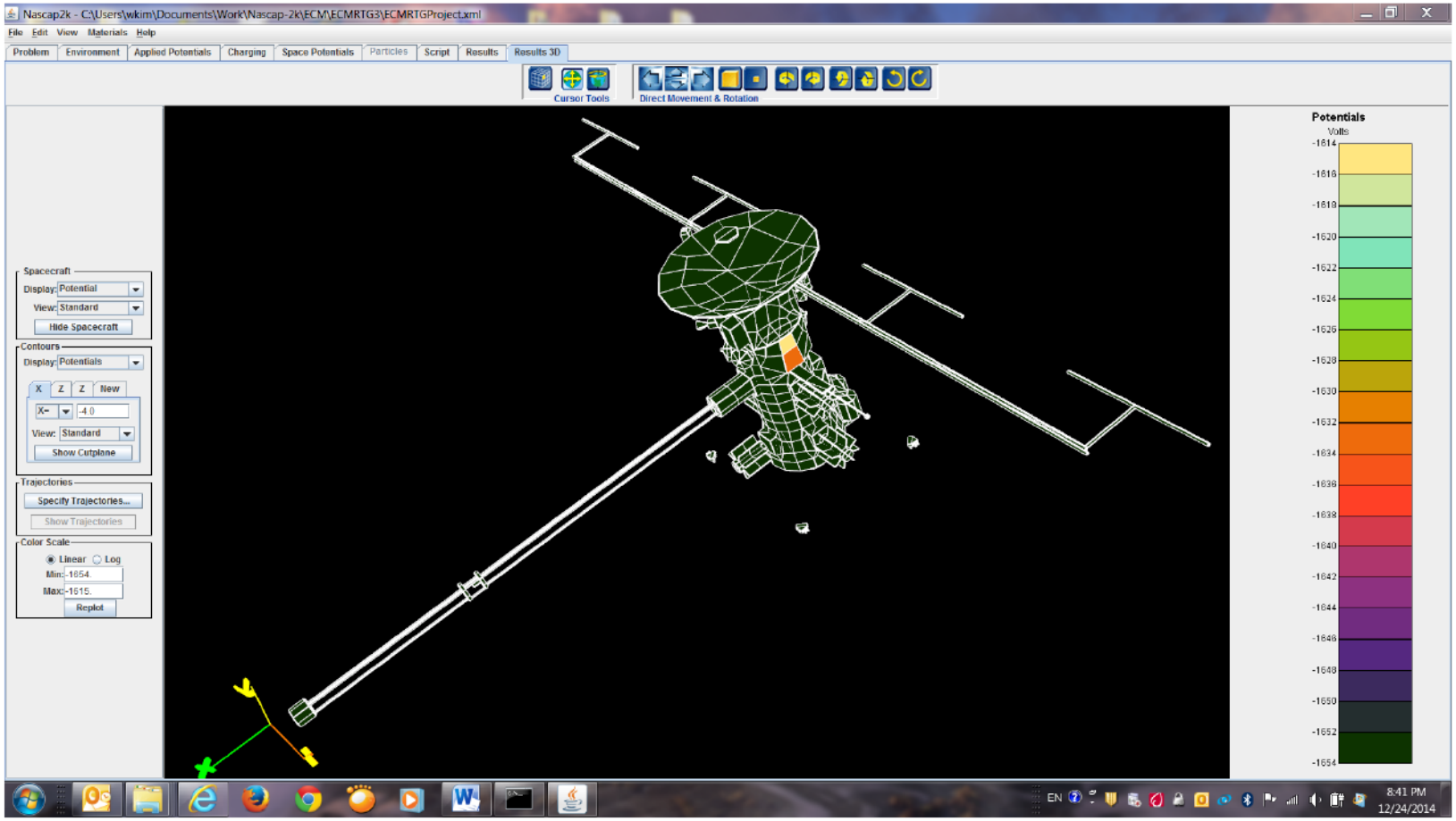

Figure 44. Three-dimensional Nascap-2k plot of a RPS-powered Europa spacecraft design concept showing the differential surface potentials. The surface material is covered in the default conductive black Kapton with δ_{max} = 0.87 as measured by J. R. Dennison and associates. Note the dramatic change in surface potential.

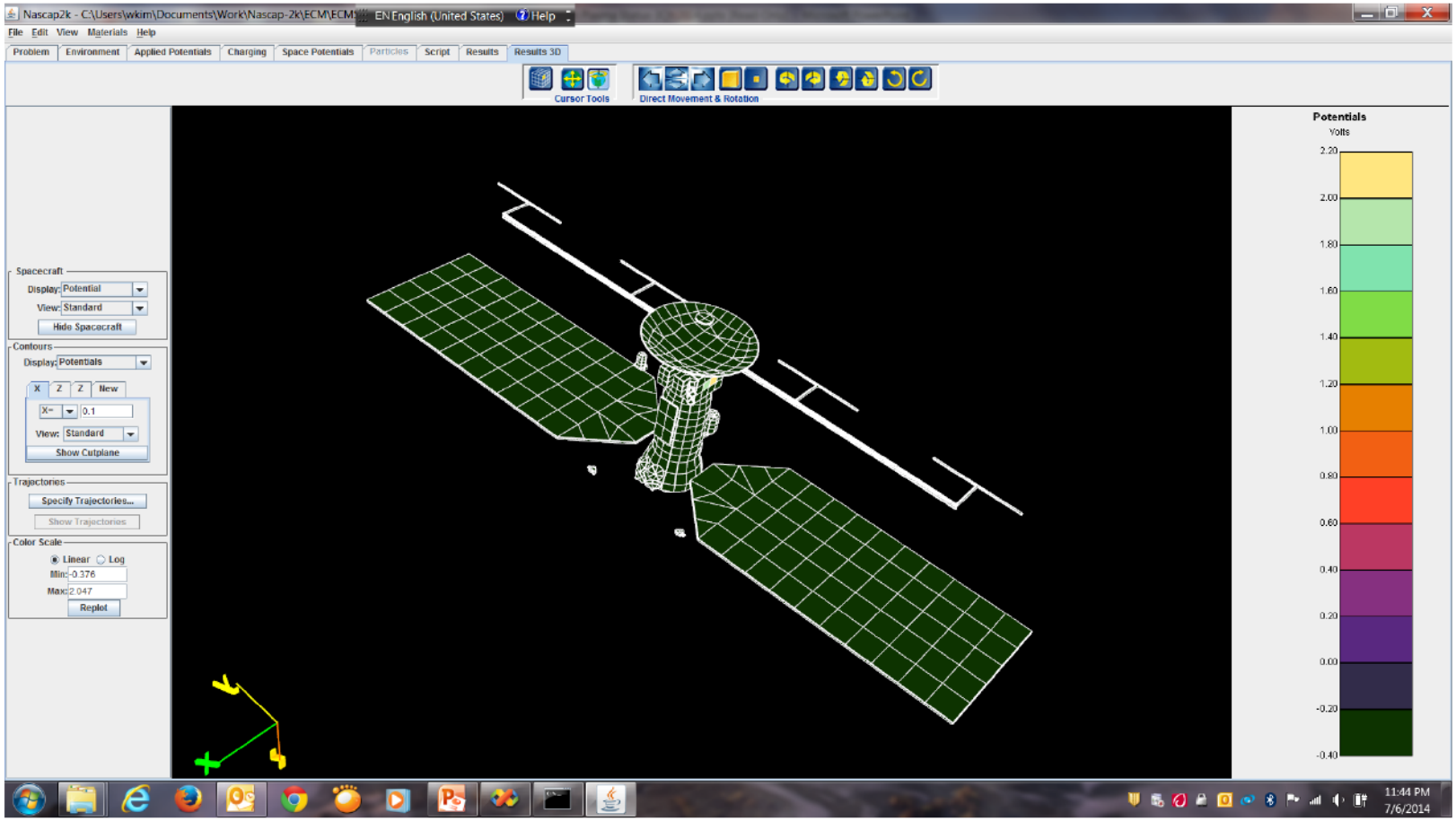

Figure 45. Similar plot of a Europa design for the solar spacecraft design concept showing the differential surface potentials. The spacecraft is assumed to be covered in black Kapton (with δ_{max} = 0.87) whereas the solar panels are assumed be coated with ITO (δ_{max} = 2.47). The potential is again ~+2 V.

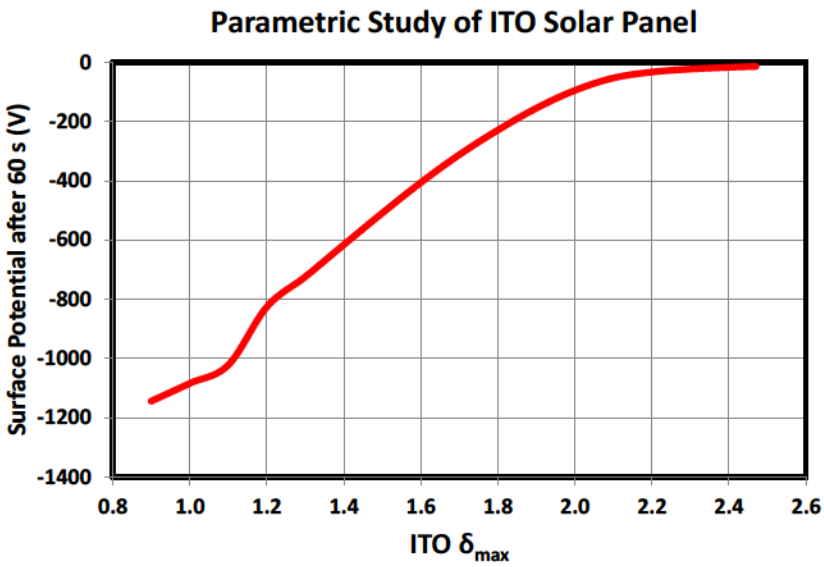

Figure 46. ITO coated solar panel potential as a function of the ITO δ_{max}.

6 CONCLUSIONS

This report has addressed uncertainties in the original plasma models at Jupiter responsible for surface charging. The updated plasma environment models were then used to evaluate two possible Europa mission designs for spacecraft charging effects using the Nascap-2k code. To be specific, prior to this study, the current Divine/Garrett jovian plasma model, DG1 (Divine and Garrett, 1983), had not been updated in 30 years. As the plasma environment is critical to evaluation of surface charging effects at Jupiter, the original DG1 model was updated so that charging levels could be properly estimated using the Nascap-2k charging code. As another task, the Nascap-2k spacecraft charging tool was modified to incorporate the multiple Kappa plasma distribution functions—an important component of the DG1/DG2 plasma models—necessary to compute the particle fluxes between ~5 keV and 100 keV. The modifications and results of those modifications to the DG1 model to produce the DG2 model and the steps taken to integrate the DG2 predictions into Nascap-2k have been described. The final task employed Nascap-2k to analyze possible Europa RPS and solar array design concepts for spacecraft charging. The designs were extremely sensitive to the secondary emission properties of the materials. The black Kapton secondary electron emission properties were found to differ significantly between a nominal value and more recent laboratory tests, the corresponding surface potentials varying from +2 V to –1650 V. On the other hand, a solar array with ITO surface coatings would drive the spacecraft potential to ~2 V. This potential, however, is also very sensitive to the secondary electron emission properties of the ITO coating with the potential varying between +2 V to –1100 V. These results imply that Europa mission designers should consider testing any surface materials/coatings for their charging properties if accurate charging measurements are desired and that contamination effects which would alter the surface properties need to be carefully considered.

7 REFERENCES

Ajello, J. M., D. E. Shemansky, W. R. Pryor, A. I. Stewart, K. E. Simmons, T. Majeed, J. H. Waite, G. R. Gladstone, and D. Grodent, "Spectroscopic Evidence for High-Altitude Aurora at Jupiter from Galileo Extreme Ultraviolet Spectrometer and Hopkins Ultraviolet Telescope Observations," *Icarus,* vol. 152, pp. 151–171, 2001.

Bagenal, F., and P. A. Delamere, "Flow of mass and energy in the magnetospheres of Jupiter and Saturn," *J. Geophys. Res.*, vol. 116, A05209, 2011, doi:10.1029/2010JA016294, 2011.

Bagenal, F., R. McNutt, Jr., J. W. Belcher, H. A. Bridge, and J. D. Sullivan, "Revised Ion Temperatures for Voyager Plasma Measurements in the Io Plasma Torus," *J. Geophys. Res.*, vol. 90, A2, pp. 1755–1757, Feb. 1, 1985.

Bagenal, F., and P. A. Delamere, LASP Galileo PLS Data Analysis website, Laboratory for Atmospheric and Space Physics, University of Colorado, Boulder, http://lasp.colorado.edu/mop/galileo/pls/index.html, 2014.

Belland, B., *Aurora Kappa Distribution Upgrade of Nascap-2K*, IOM 5132-14-053 (JPL internal document), To: H. Garrett, From: B. Belland and W. Kim, November 12, 2014, Jet Propulsion Laboratory, California Institute of Technology, Pasadena, California, 2014.

Bhattacharya, B., R. M. Thorne, and D. J. Williams, "On the energy source for the diffuse Jovian auroral emissivity," *Geophys. Res. Lttrs.,* vol. 28, pp. 2715–2754, 2001.

Clarke, J., G. Ballester, J. Trauger, and R. Evans, "Hubble Follows Rapid Changes in Jupiter's Aurora," *News Release Number: STScI-1996-3,* Space Telescope Science Institute, Baltimore, MD, Oct. 17, 1996.

Connerney, J. E., M. H. Acuna, N. F. Ness, and T. Satoh, "New models of Jupiter's magnetic field constrained by the Io flux tube footprint," *J. Geophys. Res.,* vol. 103, pp. 11929–11940, 1998.

Davis, V. A., M. J. Mandell, B. M. Gardner, I. G. Mikellides, L. F. Neergaard, D. L. Cooke, and J. Minow, "Validation of Nascap-2k Spacecraft-Environment Interactions Calculations," presented at *8th Spacecraft Charging Technology Conference*, Huntsville, Alabama, in NASA Technical Reports Server, 2004.

Delamere, P. A., F. Bagenal, and A. Steffl, Radial variations in the Io plasma torus during the Cassini era, *J. Geophys. Res.*, vol. 110, A12223, doi:10.1029/2005JA011251, 2005.

Divine, T. N., and H. B. Garrett, "Charged particle distributions in Jupiter's magnetosphere," *J. Geophys. Res.,* vol. 88, pp. 6889–6903, 1983.

Fontheim, E. G., K. Stasiewicz, M. O. Chandler, R. S. B. Ong, and E. Gombosi. "Statistical Study of Precipitating Electrons," *J. Geophys. Res*., vol. 87, no. A5, pp. 3469–3480, May 1, 1982.

Frank, L. A., K. L. Ackerson, J. A. Lee, M. R. English, and G. L. Pickett, "The plasma instrumentation for the Galileo Mission," *Space Sci. Rev.*, vol. 60, pp. 283– 307, 1992.

Frank, L. A., and W. R. Paterson, "Galileo observations of electron beams and thermal ions in Jupiter's magnetosphere and their relationship to the auroras," *J. Geophys. Res.*, vol. 107, A12, pp. 1478–1494, doi:10.1029/2001JA009150, 2002.

Garrett, H. B., and S. E. Deforest, "Analytical Simulation of the Geosynchronous Plasma Environment," *Planet. Space Sci.*, vol. 27, pp. 1101–1109, 1979.

Garrett, H. B., and A. Hoffman, "Comparison of Spacecraft Charging Environments at the Earth, Jupiter, and Saturn," *IEEE Trans. Plasma Sci.*, vol. 28, no. 6, pp. 2048–2057, Dec. 2000.

Garrett, H. B., I. Jun, J. M. Ratliff, R. W. Evans, G. A. Clough, and R. W. McEntire, *Galileo Interim Radiation Electron Model*, JPL Publication 03-006, 72 pages, Jet Propulsion Laboratory, California Institute of Technology, Pasadena, CA, 2003. http://www.openchannelfoundation.org/projects/GIRE/

Garrett, H. B., *Divine/Garrett Jovian Plasma Models*, JPL IOM 5130-06-012 (internal document), Jet Propulsion Laboratory, California Institute of Technology, Pasadena, California, May 16, 2006.

Garrett, H. B., R. W. Evans, A. C. Whittlesey, I. Katz, and I. Jun, "Modeling of the Jovian Auroral Environment and Its Effects on Spacecraft Charging," *IEEE Transactions on Plasma Science,* vol. 36, pp. 2440–2449, Oct. 2008.

Garrett, H. B., Kokorowski, M., Jun, I., and Evans, R. W., Galileo Interim Radiation Electron Model Update—2012", JPL Publication 12-9, March 2012. (See also Garrett, H. B., Kokorowski, M., Jun, I., and Evans, R. W., *Galileo Interim Radiation Electron Model Update—2011*, JPL IOM-5130-11-053, 29 November 2011, for the back-up computer code listings).

Garrett, H. B., I. Katz, I. Jun, W. Kim, A. C. Whittlesey, and R. W. Evans, "The Jovian Charging Environment and its Effects—A Review," *IEEE Trans. On Plasma Sci.,* vol. 40, no. 2, pp. 144–154, February 2012.

Garrett, H.B., L. M. Martinez-Sierra, and R. W. Evans, *Updating the Jovian Proton Radiation Environment—2015*, JPL Publication 15-9, pp. 36, October 2015. (See also H. B. Garrett, R. W. Evans, and Luz Maria Martinez-Sierra," IOM 5130-15-003, September 30, 2015, for the back-up computer code listings). See JPL website: http://hdl.handle.net/2014/45463

Grodent, D., J. T. Clarke, J. Kim, J. H. Waite, Jr., and C. S. W. H., "Jupiter's main auroral oval observed with HST-STIS," *J. Geophys. Res.,* vol. 108, no. 11, pp. 1389–1404, 2003.

Hill, T. W., and F. C. Michel, "Heavy ions from the Galilean satellites and the centrifugal distortion of the Jovian magnetosphere," *J. Geophys. Res.*, vol. 81, pp. 4561–4565, 1976.

Krimigis, S. M., T. P. Armstrong, W. I. Axford, C. O. Bostrom, C. Y. Fan, G. Gloeckler, L. J. Lanzerotti, E. P. Keath, R. D. Zwickl, J. F. Carbary, and D. C. Hamilton, "Low-energy charged particle environment at Jupiter: A first look," *Science*, vol. 204, 998–1003, 1979a.

Krimigis, S. M., T. P. Armstrong, W. I. Axford, C. O. Bostrom, C. Y. Fan, G. Gloeckler, L. J. Lanzerotti, E. P. Keath, R. D. Zwickl, J. F. Carbary, and D. C. Hamilton, "Hot plasma environment at Jupiter: Voyager 2 results." *Science*, vol. 206, pp. 977–984, 1979b.

Krimigis, S. M., J. F. Carbary, E. P. Keath, C. O. Bostrom, W. I. Axford, G. Gloeckler, L. J. Lanzerotti, and T. P. Armstrong, "Characteristics of hot plasma in the Jovian magnetosphere: Results from the Voyager spacecraft," *J. Geophys. Res.*, vol. 86, 8227-8257, 1981

Krainsky, I., W. Lundin, W. L. Gordon, and R. W. Hoffman, "Secondary Electron Emission Yeilds," *Proc. of USAF/NASA Spacecraft Charging Conference III*, Colorado Springs, CO, Nov. 1980.

Mandell, M. J., V. A. Davis, B. M. Gardner, I. G. Mikellides, D. L. Cooke, and J. Minor, "Nascap-2k—An Overview," *Transactions on Plasma Science,* vol. 34, no. 5, pp. 2084–2093, 2006.

McNutt, R. L., Jr., *The dynamics of the low energy plasma in the Jovian magnetosphere*, Ph.D. thesis, Mass. Inst. of Technol., Cambridge, MA, 1980.

McNutt, R. L., Jr., J. W. Belcher, and H. S. Bridge, “Positve ion observations in the middle magnetosphere of Jupiter,” *J. Geophys. Res.*, vol. 86, pp. 8319–8342, 1981.

Richardson, J. D., and E. C. Sittler, Jr., "A plasma density model for Saturn based on Voyager observations," *J. Geophys. Res.,* vol. 95, pp. 12,019–12,031, 1990.

Scudder, J. D., E. C. Sittler, Jr., and H. S. Bridge, “A survey of the plasma electron environment of Jupiter: A view from Voyager,, *J. Geophys. Res.,* vol. 86, no. A10, pp. 8157–8179, 1981

Seidelmann, P. K., and T. N. Divine, "Evaluation of Jupiter longitudes in System III (1965)," *Geophys. Res. Lett.,* vol. 4, pp. 65–68, 1977.

Sittler, E. C., Jr., and D. F. Strobel, “Io plasma torus electrons: Voyager 1,” *J. Geophys. Res.*, vol. 92, no. A6, pp. 5741–5762, 1987.

Smyth, W. H., C. A. Peterson, and M. L. Marconi, “A consistent understanding of the ribbon structure for the Io plasma torus at the Voyager 1, 1991 ground-based, and Galileo J0 epochs,*” J. Geophys. Res.*, 116, A07205, doi:10.1029/2010JA016094, 2011.

Yelle, R. V., and S. Miller, "Jupiter's Thermosphere and Ionosphere", Chapter 9, pp. 185–3218, in *Jupiter, The Planet, Satellites and Magnetosphere*, edited by F. Bagenal, T. Dowling, and W. McKinnon, Cambridge Press, Cambridge, UK, 2004.

APPENDIX A. CONTOUR PLOTS

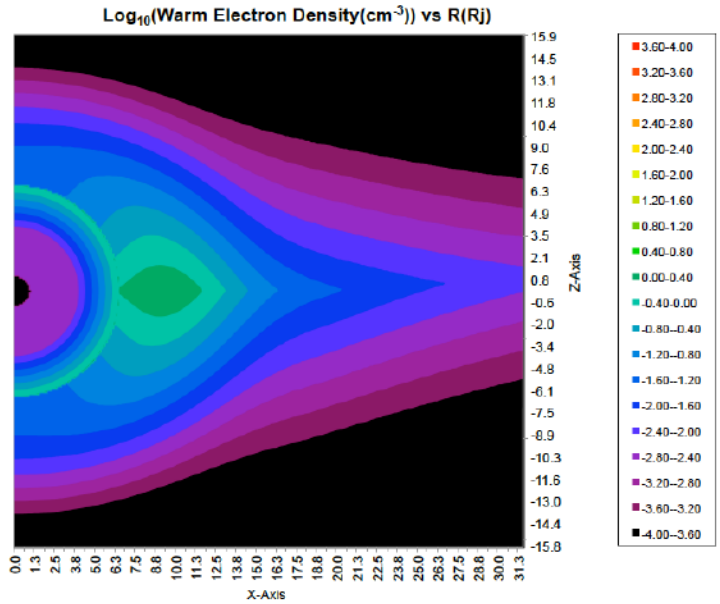

Figure A-1. Meridional contour plot of Log_{10} of warm electron density at 110° W longitude.

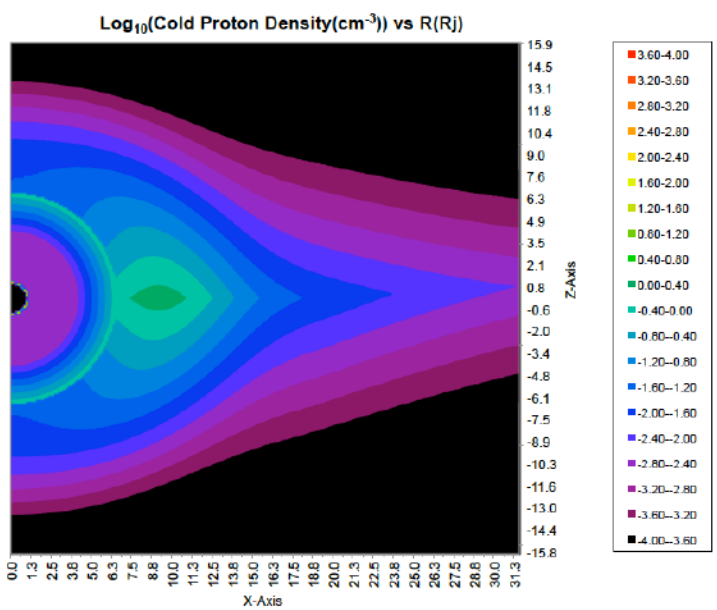

Figure A-2. Meridional contour plot of Log_{10} of cold proton density at 110° W longitude. See 3.2.4 for discussion of concerns with this parameter.

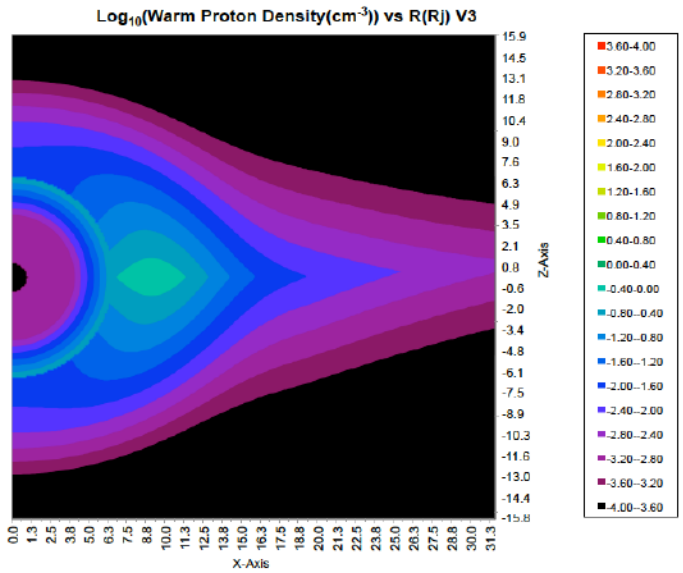

Figure A-3. Meridional contour plot of Log_{10} of warm proton density at 110° W longitude.

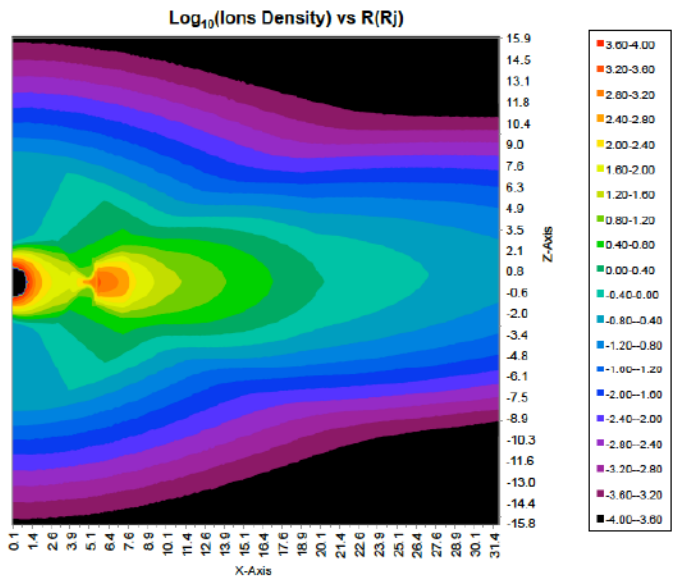

Figure A-4. Meridional contour plot of Log_{10} of the total ion density plus the cold protons at 110° W longitude. See text for discussion of concerns with this parameter.

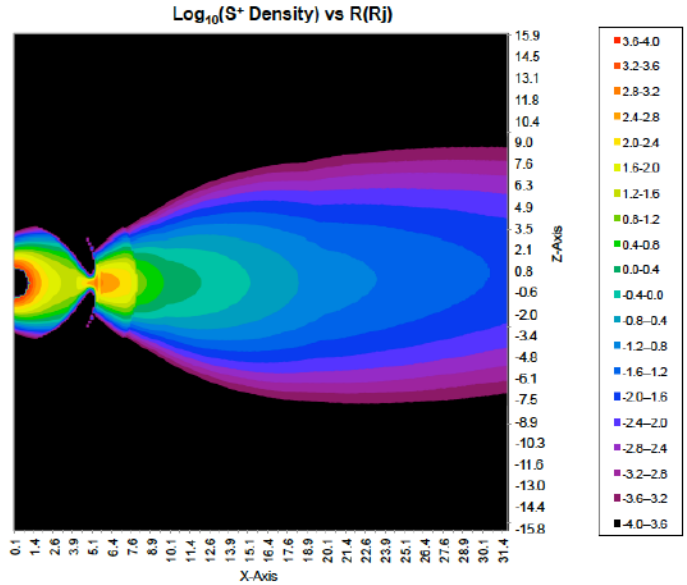

Figure A-5. Meridional contour plot of Log_{10} of cold ion S^+ at 110° W longitude.

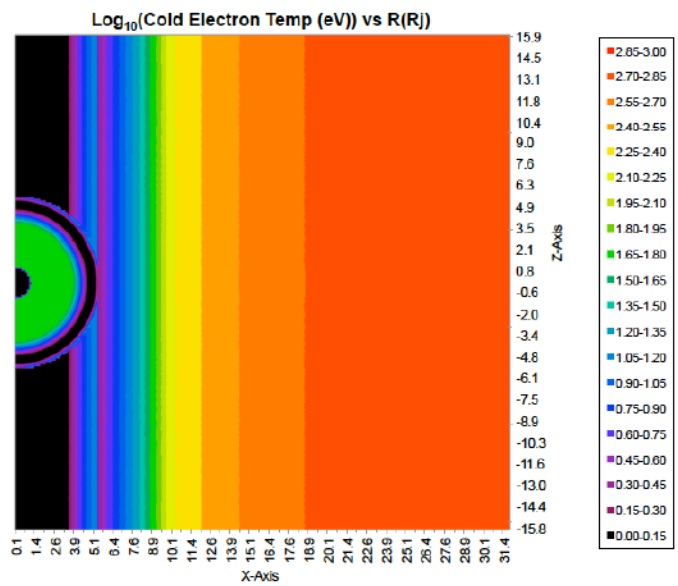

Figure A-6. Meridional contour plot of Log_{10} of the cold electron temperature at 110° W longitude.

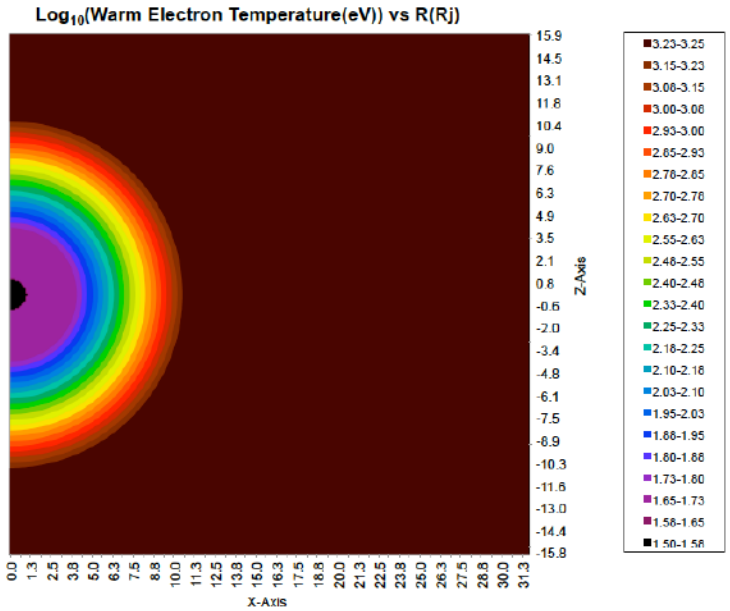

Figure A-7. Meridional contour plot of the warm electron temperature at 110° W longitude.

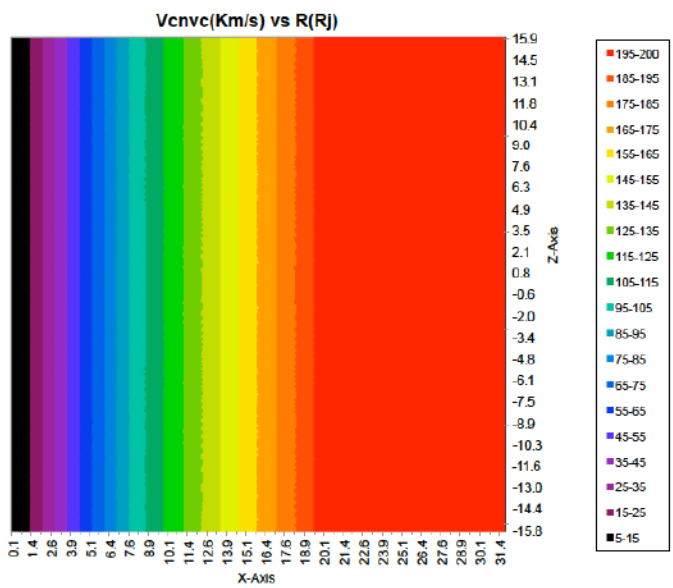

Figure A-8. Meridional contour plot of the ion convection velocity at 110° W longitude.

APPENDIX B. JOVIAN IONOSPHERE MODEL

To provide a means for comparing the DG2 plasma model with Juno along its entire trajectory and to provide a means for later updating the model using the Juno data, a simple ionospheric module has been developed. The ionosphere is defined to be the region between the "surface" of Jupiter and 8500 km. The jovian "surface" is defined as:

$$R_{surface}(\lambda) = 1\ \text{Rj}*(1-0.06487*\sin(\lambda)^2) \qquad \text{(B1)}$$

where:

$R_{surface}$	= "surface" at Jupiter, defined as the 1 Atm pressure level
λ	= jovian latitude (System III)

Unfortunately the jovian ionosphere appears to be highly variable in time and latitude. To provide a starting point for modeling the ionosphere in the future, a representative electron profile was selected based on Yelle and Miller (2004). Mathematically, the profile between 0 and 8500 km is given by:

<u>Density:</u>

For $Ht < 2484.2666$ km

$$R_{insph}(Ht) = -8.9483\text{E-}8\ Ht^4 + 1.0769\text{E-}3\ Ht^3 - 4.7322\ Ht^2 + 8866\ Ht - 5.759\text{E+}6 \qquad \text{(B1)}$$

For $Ht \geq 2484.2666$ km

$$R_{insph}(Ht) = 3.0\text{e}6\ e^{(-Ht/841.)}$$

(If $R_{insph} < 1$, $R_{insph} = 1$)

<u>Temperature:</u>

For $Ht < 0.0$ km

$$T_{insph}(Ht) = 0.02\ \text{eV}$$

For $0.0 \leq Ht \leq 8500$ km

$$T_{insph}(Ht) = ((e^{+((Ht/350)-5)} - e^{-((Ht/350.)-5)})/2 + 75)^{0.4} \cdot 0.022 \qquad \text{(B3)}$$

For $Ht > 8500$ km

$$T_{insph}(Ht) = 46\ \text{eV}$$

where:

$R_{insph}(Ht)$	= electron density as a function of height; cm^{-3}
$T_{insph}(Ht)$	= electron temperature as function of height; eV
Ht	= height above $R_{surface}$ (1 Atm level); km

Figures B-1 and B-2 illustrate the electron (and cold ion) density and temperature profiles. To balance the charge, the cold protons were equated to the cold electron densities and temperatures.

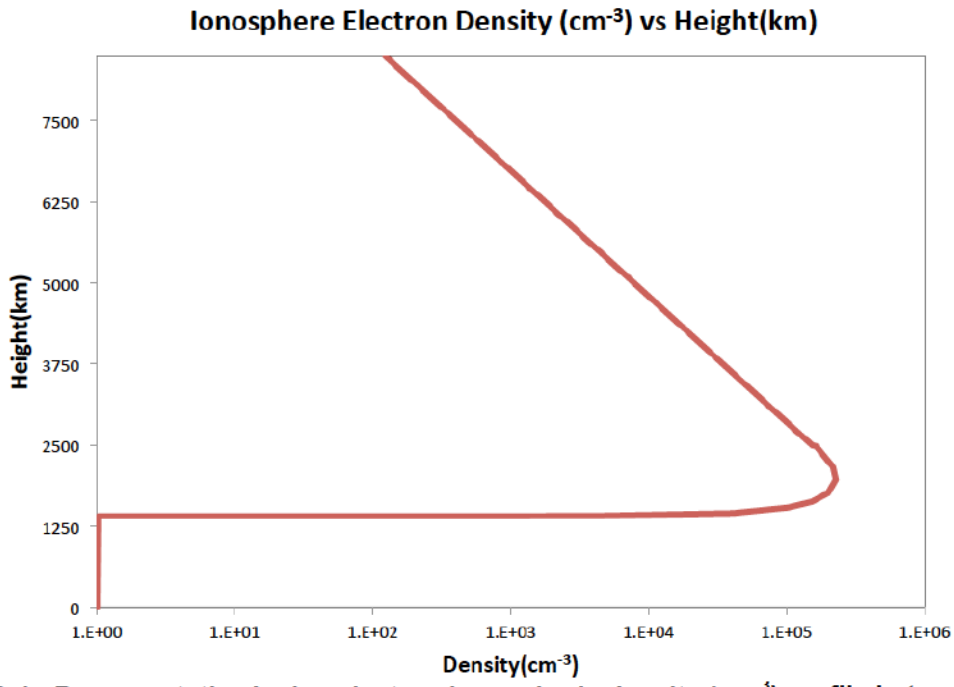

Fig. B-1. Representative jovian electron ionospheric density (cm^{-3}) profile between 0 km and 8500 km based on profiles from Yelle and Miller (2004). The cold ion profile is assumed to be the same.

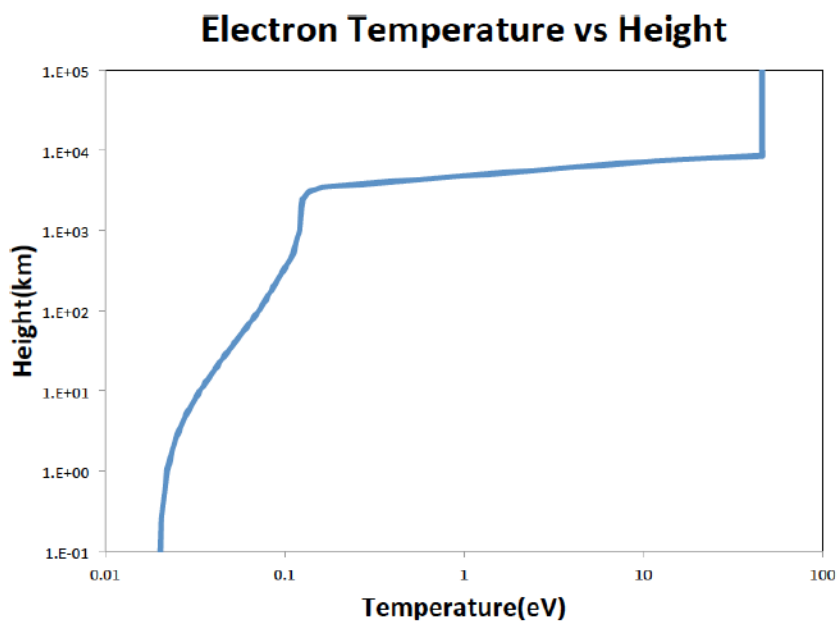

Fig. B-2 Representative jovian electron ionospheric temperature (eV) profile between 0 km and 8500 km based on profiles from Yelle and Miller (2004). The cold ion profile is assumed to be the same.

APPENDIX C. ACRONYMS AND ABBREVIATIONS

ALAT	latitude, System III
AMU	atomic mass unit
CTS	counts per second [Figure 6 has cts lower case.]
DG1	Divine and Garrett 1983 model
DG2	Revised version of the DG1 model—new plasma model presented in this report
EPD	Energetic Particle Detector
E/Q	Ratio of particle energy (E) to electron charge (Q)
ET	Solar System Barycentric Ephemeris Time
FORTRAN	Formula Translating System computer language
GEO	geosynchronous Earth orbit
GIRE	Galileo Interim Radiation Electron model (2003)
GIRE2	Galileo Interim Radiation Electron model, Version 2 (2012)
GUI	graphical user interface
HST	Hubble Space Telescope
I/O	input/output
IR	Infrared
ITO	Indium Tin Oxide surface coat material
JOI	Jupiter Orbit Insertion
JPL	Jet Propulsion Laboratory
Nascap-2k	NASA Spacecraft Charging Analyzer Program-Version 2k
PDS	Planetary Data System
PLS	Voyager Plasma Science
PRA	Voyager Planetary Radio Astronomy instrument

PWS	Voyager Plasma Wave Subsystem
RHOE	cold electron density
Rj	Jupiter radius, 71,400 km
RPS	radioisotope power system
UT	Universal Time (Greenwich Mean Time)
UV	Ultraviolet
WLONG	West longitude, System III